

The Saga of α -RuCl₃: Parameters, Models, and Phase Diagrams

Marius Möller,¹ P. A. Maksimov,² Shengtao Jiang (蒋晟韬),³ Steven R. White,⁴ Roser Valentí,¹ and A. L. Chernyshev⁴

¹*Institut für Theoretische Physik, Goethe-Universität Frankfurt,
Max-von-Laue Strasse 1, 60438 Frankfurt, Germany*

²*Bogolyubov Laboratory of Theoretical Physics, Joint Institute for Nuclear Research, Dubna, Moscow region 141980, Russia*

³*Stanford Institute for Materials and Energy Sciences,*

SLAC National Accelerator Laboratory and Stanford University, Menlo Park, California 94025, USA

⁴*Department of Physics and Astronomy, University of California, Irvine, California 92697, USA*

(Dated: February 18, 2025)

RuCl₃ was likely the first ever deliberately synthesized ruthenium compound, following the discovery of the $_{44}\text{Ru}$ element in 1844. For a long time it was known as an oxidation catalyst, with its physical properties being discrepant and confusing, until a decade ago when its allotropic form α -RuCl₃ rose to exceptional prominence. This “re-discovery” of α -RuCl₃ has not only reshaped the hunt for a material manifestation of the Kitaev spin liquid, but it has opened the floodgates of theoretical and experimental research in the many unusual phases and excitations that the anisotropic-exchange magnets as a class of compounds have to offer. Given its importance for the field of Kitaev materials, it is astonishing that the low-energy spin model that describes this compound and its possible proximity to the much-desired spin-liquid state is still a subject of significant debate ten years later. In the present study, we argue that the existing key phenomenological observations put strong natural constraints on the effective microscopic spin model of α -RuCl₃, and specifically on its spin-orbit-induced anisotropic-exchange parameters that are responsible for the non-trivial physical properties of this material. These constraints allow one to focus on the relevant region of the multi-dimensional phase diagram of the α -RuCl₃ model, suggest an intuitive description of it via a different parametrization of the exchange matrix, offer a unifying view on the earlier assessments of its parameters, and bring closer together several approaches to the derivation of anisotropic-exchange models. We explore extended phase diagrams relevant to the α -RuCl₃ parameter space using quasi-classical, Luttinger-Tisza, exact diagonalization, and density-matrix renormalization group methods, demonstrating a remarkably close quantitative accord between them on the general structure and hierarchy of the phases, with the zigzag, ferromagnetic, and incommensurate phases that are proximate to each other. One of the highlights is the detailed agreement on the nature of the incommensurate phases that realize two distinct counter-rotating helical states.

I. INTRODUCTION

As every story needs a hero [1], every condensed matter field needs a champion material, be it silicon for semiconductors [2], yttrium-iron garnet for spintronics [3], or graphene for 2D materials [4]. With its 50-year-long quest for a spin-liquid compound, the field of quantum magnetism is, arguably, still on the search for one [5, 6].

For some time, the mineral herbertsmithite, a copper-zinc hydroxychloride with its five-element composition and elaborate crystal structure, seemed to be destined for that title [7]. Made of kagomé layers of corner-sharing triangles of nearly isotropically coupled spin- $\frac{1}{2}$ Cu²⁺ ions—a motif that provides maximum frustration of magnetic orders and promotes spin-singlets—it was fitting all the theoretical stereotypes for the leading spin-liquid paradigm, suggesting a true realization of the singlet-soup state of resonating valence bonds [8]. That is, until the issues of site disorder mimicking spin-liquid features rendered this hope fruitless, although efforts continue to find its cleaner incarnation [7, 9].

But then something happened that the archetypal construct of the isotropic spin models on triangular-motif lattices did not anticipate. The fallen champion’s title was picked up by one of the most unlikely materials imaginable. Also a chloride, but a mere binary com-

pound with a geometrically unfrustrated bipartite arrangement of magnetic ions in stacked honeycomb-lattice sheets. When Karl Ernst Claus, a 19th century chemist at Kazan University, synthesized ruthenium trichloride in 1845 [10], little did he know that nearly two hundred years later physicists and material scientists alike would pin their hopes on his humble creation as being a close realization of an exotic state of matter—a Kitaev spin liquid—that could shape the fortunes of not just quantum magnetism, but the broader fields of quantum materials and topological quantum computing [11].

Historically, α -RuCl₃ has always been puzzling [12]. With its layered honeycomb-lattice composition of edge-sharing RuCl₆ octahedra [13], the actual space group symmetry, amount of the octahedral distortion, and propensity toward interlayer stacking faults have all been the subject of debate [14]. Its electronic characterization has evolved from being a small-gap magnetic semiconductor to a narrow-band Mott-Hubbard insulator that combines spin-orbit coupling and electronic correlations [15–18]. By analogy with other halides of transition metals [19], it was initially suggested to have ferromagnetic Ru-planes ordered antiferromagnetically [13, 20], but this was proven incorrect later [21, 22].

This was the state of understanding of α -RuCl₃ about ten years ago, when the search for the Kitaev spin liq-

uid in the initially more promising $5d$ iridium-oxide compounds was waning [14]. The focus of that search has moved to the structurally similar materials of the $4d$ elements with spin-orbit coupling, in which $\alpha\text{-RuCl}_3$ stood out because of its supposed nearly ideal edge-sharing octahedral structure in the honeycomb-lattice planes and uncertain electronic and magnetic properties [18].

$\alpha\text{-RuCl}_3$'s ascent to fame was not without theoretical input. The celebrated spin-liquid solution of the compass-like [23] honeycomb-lattice model by Kitaev [11], featuring topological fermionic excitations, was initially perceived as a largely theoretical construct. It was propelled to the domain of physical reality by the seminal microscopic insight of Jackeli and Khaliullin [24, 25], which laid out that Mott insulators of transition metal ions in the edge-sharing octahedral environment of ligands can lead to that very model in the limit of strong spin-orbit coupling. The anticipated nearly perfect edge-sharing RuCl_6 octahedra, weak magnetic ordering, subsequent convincing evidence of continuum-like excitations [21, 26–31], and observations of a significant and potentially anomalous thermal Hall effect [32–38] have all fueled hopes for $\alpha\text{-RuCl}_3$'s singular place in history as the key material realizing this model.

While inspiring an enormous amount of theoretical and experimental research [39–45], the initial expectations of becoming a Rosetta stone for the Kitaev spin liquid have likely not played out for $\alpha\text{-RuCl}_3$. The longer-range exchanges and other significant interactions in its low-energy spin model have arguably moved it away from the pure-Kitaev limit and its phenomenology [14]. Various spectroscopic signatures of the broad continuum, combined with the sharper excitations at lower energies, have received a more natural explanation as a combination of strongly coupled magnons and their multi-magnon states [46–48], while substantial contribution of phonons has not left much room for exotic explanations of the field-induced thermal transport in $\alpha\text{-RuCl}_3$ [49–56].

Nevertheless, the research effort devoted to this material has already laid a prominent keystone in revealing exceptional richness of phenomena offered by anisotropic-exchange magnets on the honeycomb and other lattices. Thus, it is rather remarkable that the agreement on the low-energy model describing this compound has not yet been reached, its place in the phase diagram of that model has not yet been settled, and relevant proximate phases have not yet been uniquely identified.

In the following few pages, we provide a brief digest describing the origin of the problem, suggesting a path to its resolution, and giving an overview of such an approach, with the detailed exposé of the results and their cross-examination presented in the main text.

A. Overall Summary

While the problem of finding a definitive set of parameters for an effective model is common to many materials, it has been particularly difficult for $\alpha\text{-RuCl}_3$ because of

its fluctuating ground and field-induced states and complicated interactions in its low-energy description. The main result of this work is a systematic path to a narrower parameter space for the $\alpha\text{-RuCl}_3$ effective model.

The key message is the approach itself. It consists of breaking the problem into stages. First is the task of identifying experimental observables that would not occur without the anisotropic-exchange parameters of the model, which originate from spin-orbit interaction. Such observables can be shown to work as effective phenomenological constraints for the most challenging parameters of the model. Then, any set of remaining parameters that are not fixed at this stage from such a partially restricted manifold is expected to meet the imposed constraints. The remaining, more traditional isotropic exchanges can be either fixed with additional constraints, or left for further adjustment. We demonstrate the success of such a staged approach in systematically narrowing the allowed parameter space of $\alpha\text{-RuCl}_3$.

Another important general message of our study is the deep insight provided by the use of an alternative crystallographic parameterization of the effective model of $\alpha\text{-RuCl}_3$. It offers a unifying view of most prior efforts to determine its underlying model and also gives a fresh perspective on it as a member of a coherent group of other materials and models.

The numerical approaches, such as exact diagonalization (ED) and density-matrix renormalization group (DMRG), allow us to verify that this entire approach, which involves quasiclassical approximations, actually holds up quantitatively. The other main utility of numerical explorations, specifically using DMRG, is the study of incommensurate phases. These phases are consistently found to be proximate to the relevant parameter space of $\alpha\text{-RuCl}_3$, but very little research has been done on their nature. The present study closes this gap by demonstrating detailed quantitative agreement on their structure, which corresponds to counter-rotating helical states.

B. Parameters' drama

Generally, the anisotropic-exchange Hamiltonians lack spin-rotational symmetries. For the effective low-energy spin-orbit-coupled spin degrees of freedom, it is the discrete symmetry of the honeycomb lattice of magnetic ions with edge-sharing octahedral ligand environment that allows *four* terms in the nearest-neighbor exchange matrix [14]. In a parametrization within the reference frame of the cubic axes of the idealized ligand bonds, see Fig. 1(a) and 1(b), these four are Kitaev, Heisenberg, and off-diagonal Γ and Γ' exchanges [57, 58], with three anisotropic terms stemming from the spin-orbit coupling within the electronic states of Ru^{3+} ions.

Arguably, deviations from the ideal Kitaev-only model are unavoidable in any realistic material [46], with all these four terms present in $\alpha\text{-RuCl}_3$ for any reasonable choice of electronic parameters [14]. An important role is also played by the third-neighbor, more isotropic J_3

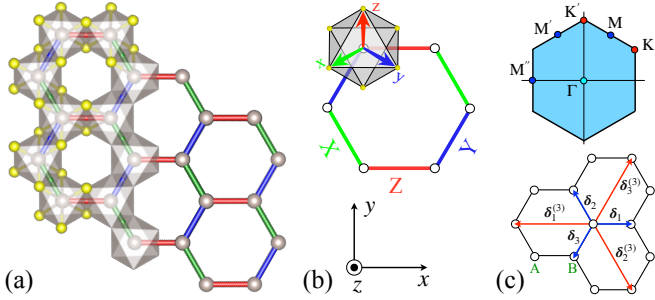


FIG. 1. (a) Ru^{3+} ions in the octahedral cages of Cl^- and the nearest-neighbor bonds. (b) $\{X, Y, Z\}$ bonds with the cubic $\{x, y, z\}$ and crystallographic $\{x, y, z\}$ axes. (c) A and B sublattices, nearest- and third-nearest-neighbor primitive vectors, δ_α and $\delta_\alpha^{(3)}$, and the Brillouin zone (BZ) of the honeycomb lattice with the high-symmetry points.

exchange [14], which, altogether, yield the minimal effective spin $S_{\text{eff}} = \frac{1}{2}$ model of the magnetic two-dimensional (2D) honeycomb-lattice planes of $\alpha\text{-RuCl}_3$

$$\hat{\mathcal{H}} = \hat{\mathcal{H}}_1 + \hat{\mathcal{H}}_3 = \sum_{\langle ij \rangle} \mathbf{S}_i^T \hat{\mathbf{J}}_{ij} \mathbf{S}_j + J_3 \sum_{\langle ij \rangle_3} \mathbf{S}_i \cdot \mathbf{S}_j, \quad (1)$$

where $\mathbf{S}_i^T = (S_i^x, S_i^y, S_i^z)$ and the nearest-neighbor part of the model in the cubic-axes parametrization is

$$\mathcal{H}_1 = \sum_{\langle ij \rangle_\gamma} \left[J \mathbf{S}_i \cdot \mathbf{S}_j + K S_i^\gamma S_j^\gamma + \Gamma (S_i^\alpha S_j^\beta + S_i^\beta S_j^\alpha) + \Gamma' (S_i^\gamma S_j^\alpha + S_i^\gamma S_j^\beta + S_i^\alpha S_j^\gamma + S_i^\beta S_j^\gamma) \right], \quad (2)$$

where the spin indices $\{\alpha, \beta, \gamma\}$ follow the $\{X, Y, Z\}$ bonds according to Fig. 1(b): $\{y, z, x\}$ for the X, $\{z, x, y\}$ for the Y, and $\{x, y, z\}$ for the Z bond, respectively.

There is a broad consensus that this generalized Kitaev-Heisenberg (KH), or *effective KJTG'-J₃* model is the *minimal* microscopic model of $\alpha\text{-RuCl}_3$ which incorporates further-neighbor exchanges into the fewer parameters. However, even the parameters of this minimal model have received very wide ranges of estimates, see Ref. [46] for the earlier overview and Sec. II below.

Because of the initial optimism regarding the near-proximity of $\alpha\text{-RuCl}_3$ to the ideal Kitaev case [26–29], early strategies have involved adding other symmetry-allowed terms to the pure Kitaev model in small quantities, with a hope for a reasonable phenomenology [59–61]. Nonetheless, significant systematic efforts have also been made to restrict parameters of the more complete versions of the generalized KH model using first-principles approaches, perturbative orbital model derivations, exact diagonalization, spin-wave calculations, and other methods, many in combination with the symmetry analysis and with the goal to match various experimental observations [62–92]. However, in spite of its importance for the field of Kitaev materials, this significant effort has not yet yielded an agreement on the parameters of the

$\alpha\text{-RuCl}_3$ model, nor are there sets of them that successfully describe the full set of experimental observations.

One objective reason for the difficulty with the convergence on the physical set of parameters for $\alpha\text{-RuCl}_3$ can be attributed to the model's multi-dimensional parameter space, which generally complicates the search for a unique set of strong microscopic constraints [14, 93]. It can also be argued that the natural instinct to reduce the dimensions of this space by neglecting some of the parameters only exacerbates the problem of convergence. This is not only due to artificial restrictions on the parameter space, possibly affecting one's ability to describe physical phenomena, but also because this reductionist approach suffers from the lack of intuition regarding the outcomes of individual terms in the standard $KJTG'$ parametrization of the exchange matrix. In a sense, the model's own complexity is a problem that has been calling for a better, more intuitive parametrization.

Another objective obstacle on the path to convergence to an ultimate parameter set are strong quantum fluctuations in both ordered and nominally polarized field-induced paramagnetic phases of $\alpha\text{-RuCl}_3$, the situation common to anisotropic-exchange magnets [94, 95]. These fluctuations limit the access to the regime of the truly polarized state with quenched quantum fluctuations, where a direct determination of the “bare” model parameters can be made using spectroscopic measurements of spin excitations, as is successfully done in the other, more fortunate quantum magnets [96–103]. This limitation leaves most of the phenomenological analyses of $\alpha\text{-RuCl}_3$ dealing with the observables that can be strongly affected by quantum effects. To extract model parameters from such observables in a meaningful part of the parameter space requires a prohibitively demanding numerical effort. Alternatively, they are extracted using semi-classical approximations, resulting in the parameters that are themselves renormalized from the bare ones, making uncertain their use for the other phenomenologies and complicating their comparison with the other suggested sets [46, 82].

C. The solution

In the present study, we propose to have reached, if not the final scene of the $\alpha\text{-RuCl}_3$ parameters' drama, but perhaps its final act.

1. Anisotropic strategy

We argue that it is precisely the spin-orbit-induced anisotropic-exchange components of the effective spin model of $\alpha\text{-RuCl}_3$ that can be strongly constrained by the existing phenomenologies. The crucial ideological steps are to identify phenomena that (i) would *not* have occurred if such terms were absent, (ii) provide *orthogonal*, i.e., not redundant, constraints that restrict different combinations of anisotropic exchanges, and (iii) have

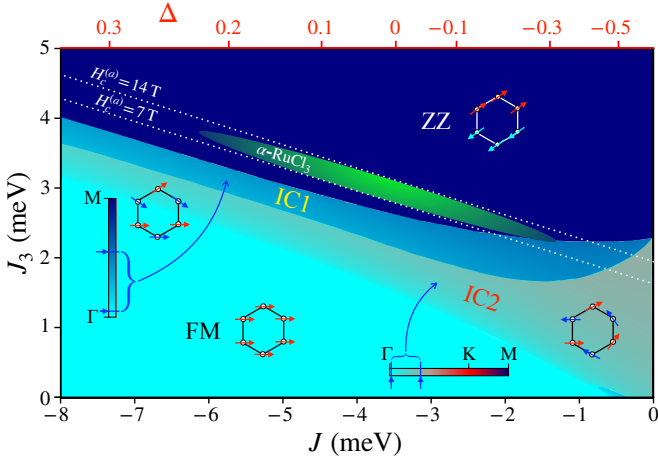


FIG. 2. The J - J_3 phase diagram of the model (1) for $J < 0$ and $J_3 > 0$ obtained by the LT approach at fixed “Point B” set of $\{K, \Gamma, \Gamma'\}$, see the text. The ZZ, FM, and IC phases, the color bars indicating ranges of their ordering vectors, and the constraints from the critical field $H_c^{(a)}$ are highlighted.

minimal effects of quantum fluctuations in them. Thus, the strategy is to focus on the bounds on the K , Γ , and Γ' terms of the generalized KH model, leaving the isotropic ones, J and J_3 , to further phenomenological constraints and explorations of the resultant lower-dimensional phase diagram in the restricted parameter subspace.

We claim to have identified three nearly orthogonal phenomenological constraints that can fulfill such a mission: (a) The out-of-plane tilt angle α of the ordered moments in the zero-field zigzag state of α -RuCl₃ [21, 22, 26, 81, 104], (b) the energy offset ΔE_g of the lowest single-spin-flip excitation in the Raman, terahertz (THz), and electron spin resonance (ESR) spectra at high fields [29, 80, 105], referred below as to the “ESR gap,” and (c) the difference of the critical fields ΔH_c for the transition to the paramagnetic phase in the two principal orthogonal in-plane directions [67, 68, 105]. Each of these quantities is thoroughly discussed in Sec. II.

By imposing physical bounds that are guided by phenomenologies on the theoretical expressions for these quantities, we can infer the bounds on the three anisotropic terms of the model (2). To illustrate the result of this approach in very broad strokes, the small critical-field difference ΔH_c strongly ties Γ' to Γ , with Γ' necessarily positive and significant [46]. The physical limits on the ESR gap provide tight bounds for Γ . Lastly, the out-of-plane tilt angle α binds Kitaev K -term in a significantly narrower range than the prior estimates, see Sec. II for further details.

In this context, two recent works suggest a promising convergence of very different approaches on the parameter space relevant to α -RuCl₃ of the same effective model.

The first is Ref. [90], which has used the extensive perturbative orbital model derivation in the spirit of the original work by Jackeli and Khaliullin [24]. By considering octahedral distortion pertinent to α -RuCl₃ and using an exhaustive set of hopping channels for all relevant

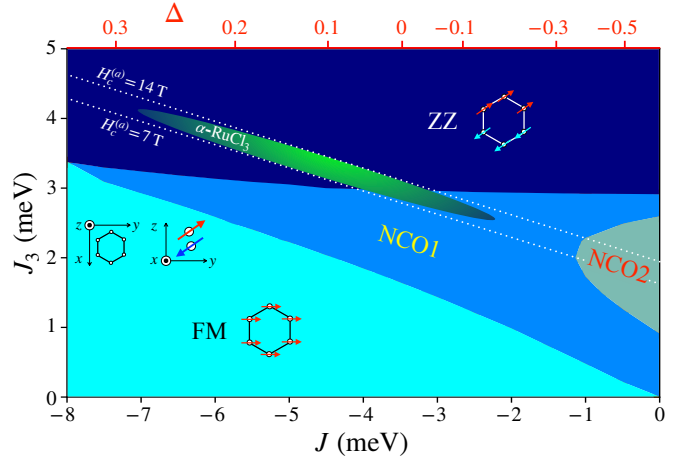


FIG. 3. Same as Fig. 2 by ED.

orbitals, their systematic microscopic derivation of the nearest-neighbor exchange parameters has yielded qualitative and quantitative trends which are very similar to our purely phenomenological results, perhaps aside from the overall rescaling, and specifically pointed to a positive and sizable Γ' term. Other close similarities between our results will be further highlighted below.

The second is Ref. [89], which has extracted interaction parameters of α -RuCl₃ from the neutron-scattering data using machine learning, but restricted itself to an artificially abbreviated model with no Γ' term, underutilizing its parameter space. Despite this restriction, their resultant model is able to satisfy, even if for the wrong reasons, two of the phenomenological constraints suggested in this work, while failing the more stringent one, as we show below. Our analysis suggests that a redo of the same effort with no artificial restrictions in the model and with an additional experimental input may open the full potential of this approach and lead to a convergence of our parameter sets.

With the proposed constraints, one is able to focus on the relevant region of the multi-dimensional phase diagram of this model. In Figure 2, we provide a representative example of such a phase diagram, in which $\{K, \Gamma, \Gamma'\}$ anisotropic terms are fixed to a set of values referred below as the “Point B” that belongs to a narrow 3D region bounded by the constraints, while the remaining “free” isotropic parameters of the model (1) are varied in the relevant region of the J - J_3 plane. The Point B selection, Luttinger-Tisza (LT) method [106–110], which is used for obtaining Fig. 2, and specific features of the spin configurations in the individual phases are all thoroughly described in Secs. II and III below. Here, we point out two ubiquitous features of this phase diagram.

First, the zigzag (ZZ) and ferromagnetic (FM) phases are prominently present in the relevant phase space of α -RuCl₃, in agreement with several prior works [65, 70, 75, 83], and are separated by a layer of two incommensurate (IC) phases with varying ordering vectors [46, 91].

Second, while the difference of the critical fields for the transition to the paramagnetic phase ΔH_c , already utilized as a constraint for the anisotropic terms, does not depend on the isotropic J and J_3 exchanges, the values of these critical fields themselves are strongly dependent on a linear combination of J and J_3 , providing another strong constraint on the α -RuCl₃ parameters [46]. While the critical fields can be strongly renormalized by quantum fluctuations, Fig. 2 demonstrates the narrow strip of the J - J_3 space that is carved by such a constraint, showing the boundaries that correspond to the bare value of one of the critical fields $H_c^{(a)} \approx 7$ T [26, 65, 67], and the value twice as high, allowing for its strong quantum renormalization. The acceptable range of $|J|$ is also broadly restricted from below by α -RuCl₃ being in the zigzag phase and from above by the overall widths of the magnetic excitation spectra [46].

We also demonstrate that the chosen strategy allows us to rein in on the otherwise prohibitively demanding numerical exploration of the α -RuCl₃ parameter space. With the phase diagram in Fig. 2 obtained by a quasi-classical Luttinger-Tisza approach [106–110], one may be skeptical of its applicability to the quantum $S=1/2$ limit of the model (1). In Figure 3, we present such a quantum phase diagram obtained by ED, see Sec. III for further details. While the nature of the intermediate phases between the ZZ and FM cannot be fully characterized in the ED approach, hence the “non-commensurate” (NCO) nomenclature, the close *quantitative* accord between the two diagrams in Fig. 2 and Fig. 3 on the general structure and hierarchy of the proximate phases is rather remarkable. These numerical explorations are also furthered by the DMRG approach, which yields unambiguous insights into the nature of the incommensurate phases and provides various selfconsistency checks on our phenomenological constraints, see Sec. IV.

2. Alternative parametrization

Generally, the exchange matrix $\hat{\mathbf{J}}_{ij}$ in the model (1) is not invariant under axes transformations if anisotropic terms are present. While the choice of the cubic axes in Fig. 1(b) is designed to make explicit the Kitaev-like structure of the model (2) which may not be obvious otherwise, this may not be the optimal choice when other significant terms are present.

The most natural physical alternative is the crystallographic reference frame associated with the planes of magnetic ions, with x and y axes corresponding to the principal in-plane directions of the honeycomb lattice and z axis pointing out of this plane, see Figs. 1(b) and 1(c). Several virtues of this reference frame, which include making explicit the symmetries of the model and bond directionality of interactions while also elucidating some of the enigmatic duality relations of the cubic-axis representation of the model (2), have been discussed in the past [46, 58, 90, 111, 112].

With the nomenclature for the $\{x, y, z\}$ frame inher-

ited from the related spin-ice models [95, 99, 113, 114], the nearest-neighbor Hamiltonian (2) is recast into the XXZ - $J_{\pm\pm}$ - $J_{z\pm}$ form

$$\begin{aligned} \mathcal{H}_1 = \sum_{\langle ij \rangle} \Big\{ & J_1 (S_i^x S_j^x + S_i^y S_j^y + \Delta S_i^z S_j^z) \\ & + 2J_{\pm\pm} \left((S_i^x S_j^x - S_i^y S_j^y) \tilde{c}_\alpha - (S_i^x S_j^y + S_i^y S_j^x) \tilde{s}_\alpha \right) \\ & + J_{z\pm} \left((S_i^x S_j^z + S_i^z S_j^x) \tilde{s}_\alpha - (S_i^y S_j^z + S_i^z S_j^y) \tilde{c}_\alpha \right) \Big\}, \end{aligned} \quad (3)$$

where we use the shorthand notations $\tilde{c}_\alpha = \cos \tilde{\varphi}_\alpha$ and $\tilde{s}_\alpha = \sin \tilde{\varphi}_\alpha$, with the phases $\tilde{\varphi}_\alpha = \{0, 2\pi/3, -2\pi/3\}$ for the $\{Z, X, Y\}$ bonds in Fig. 1 being the bond angles of the primitive vectors δ_α with the x axis.

The matrix of the transformation from the cubic $\{x, y, z\}$ to the crystallographic $\{x, y, z\}$ reference frame, $\mathbf{S}_{\text{cryst}} = \hat{\mathbf{R}}_c \mathbf{S}_{\text{cubic}}$, is given in Appendix A together with the translation of the parameters of the generalized KH model in the form (2) to that of (3) and back: $\{J, K, \Gamma, \Gamma'\} \leftrightarrow \{J_1, \Delta J_1, J_{\pm\pm}, J_{z\pm}\}$. The isotropic third-neighbor \mathcal{H}_3 in (1) is unchanged by this transformation.

One immediate advantage of the crystallographic form of the model (3) is in having fewer bond-dependent terms, with its first line being a conventional XXZ Hamiltonian. As we argue in Sec. II, the XXZ - $J_{\pm\pm}$ - $J_{z\pm}$ model (3) also provides a much more intuitive understanding of the outcomes of its individual terms, allowing one to tie them directly to specific observables. One such example is the out-of-plane tilt angle α discussed above, which can only be caused by the $J_{z\pm}$ -term, the sole term in the model that connects the in-plane and the out-of-plane spin components. Another example is the ESR gap ΔE_g that depends on an uninformative combination of Γ and Γ' in the $K\Gamma\Gamma'$ language (2), but corresponds to a simple XXZ anisotropy, $J_1(1 - \Delta)$, upon translation to the crystallographic frame (3), see Sec. II.

Moreover, significant additional progress in understanding α -RuCl₃ can be made by reforging phenomenological constraints on the anisotropic parameters of the generalized KH model (2) $\{K, \Gamma, \Gamma'\}$ into similar constraints on the $\{J_1(1 - \Delta), J_{\pm\pm}, J_{z\pm}\}$ terms of the model (3). This conversion results in a clear hierarchy of the parameters of this model and, ultimately, in a simpler and more intuitive version of it.

For the advocated parameter ranges of α -RuCl₃, the nearest-neighbor part of the spin model in the crystallographic language can be shown to have two leading terms, J_1 and $J_{z\pm}$, and two secondary ones, the XXZ parameter Δ and one of the bond-dependent anisotropic terms, $J_{\pm\pm}$. This hierarchy is also in very close accord with the results of the orbital model expansion of Ref. [90] discussed above, and is in broader agreement with the majority of the earlier assessments of the α -RuCl₃ parameters, offering a unifying view of them as all pointing in a similar direction, although often in a limited way.

It transpires that the resultant minimal model that closely describes α -RuCl₃ is dominated by the XY ($\Delta \approx 0$) ferromagnetic J_1 and sizable anisotropic $J_{z\pm}$ terms,

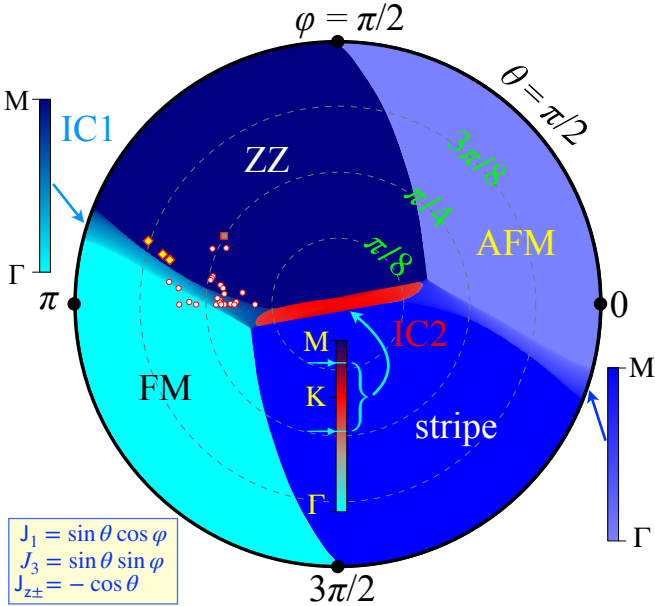


FIG. 4. Polar phase diagram of the model (3) for $\Delta = J_{\pm\pm} = 0$, with J_1 and J_3 encoding the polar and $J_{z\pm}$ the radial coordinates in units of $J_1^2 + J_{z\pm}^2 + J_3^2 = 1$, see the legend. Phases are discussed below and the small symbols near the ZZ-FM boundary are projections of prior $\alpha\text{-RuCl}_3$ parameter searches onto the $\Delta = J_{\pm\pm} = 0$ plane, see Sec. III B for details.

which are complemented by the isotropic antiferromagnetic J_3 exchange. The neglected Δ and $J_{\pm\pm}$ can be verified as playing only secondary roles in the physical outcomes compared to the leading terms.

Needless to say, this revelation suggests a considerable simplification of the $\alpha\text{-RuCl}_3$ parameter problem, as it allows a significantly more focused and detailed exploration of the relevant and physically justified three-dimensional parameter space of the resultant $J_1^{XY} - J_{z\pm} - J_3$ model.

In Figure 4, we provide an example of such an exploration in the form of its polar phase diagram, with details given in Sec. III. In this phase diagram, obtained by the same LT method as Fig. 2, J_1 and J_3 encode the polar coordinate and $J_{z\pm}$ is the radial one, as indicated in the legend. While covering the entire parameter space of the $J_1^{XY} - J_{z\pm} - J_3$ model, which contains additional antiferromagnetic (AFM) and stripe phases, the relevant segment of it is populated by the zigzag and ferromagnetic phases, separated by the incommensurate phase. This proximity is already familiar from the Cartesian phase diagrams of Figs. 2 and 3, which offer a different slice through the same higher-dimensional parameter space. In addition, the small symbols in Fig. 4 are the projections of the majority of the previously proposed $\alpha\text{-RuCl}_3$ parameter sets onto the $\Delta = J_{\pm\pm} = 0$ plane of the phase diagram, demonstrating the commonality of the trends and phenomenologies that all of them were trying to capture.

It is also important to point out that the model in the crystallographic frame (3) and its abbreviated $J_1 - J_{z\pm} - J_3$ version offer a direct connection to the broader spectrum

of the paradigmatic models in frustrated magnetism. In fact, the circumference of the phase diagram in Fig. 4 corresponds to the $J_1 - J_3$ FM-AFM model that has been studied since long ago [115] and has attracted significant attention very recently in the context of the other material candidates of the Kitaev model realization [116–119]. This model and its ubiquitous characteristic sequence of the FM, ZZ, and intermediate phases also provide a wider context to the studies of $\alpha\text{-RuCl}_3$.

D. The plan

With the brief synopsis of our findings given in the previous pages, the rest of the paper is organized as follows.

The empirical constraints and representation of them in the cubic and crystallographic reference frames, the outline of the advocated parameter space, and selected representative choices of the anisotropic exchanges are discussed in Section II together with the systematic analysis of the prior efforts at the $\alpha\text{-RuCl}_3$ parameters in the context of the proposed phenomenologies.

In Section III, we provide a detailed discussion of the phase diagrams for the relevant region of the multi-dimensional parameter space of the $\alpha\text{-RuCl}_3$ model, such as the ones in Figs. 2 and 3 in the generalized KH, and in Fig. 4 in the crystallographic axes. Here we also elaborate on the technical details of the approaches that are used for their derivation.

A comparative analysis uncovering the nature of the incommensurate phases in these phase diagrams using DMRG is presented in Section IV. Further insights and selfconsistency checks from the unbiased numerical methods on the phenomenological constraints and other assumptions of our approach are also provided.

We discuss possible future directions as an outlook in Section V and present a summary in Section VI. Technical details are delegated to Appendices.

II. CONSTRAINTS AND PARAMETERS

In this Section, we demonstrate that the available phenomenologies are powerful enough to significantly restrict the physically reasonable parameter space of the generalized KH model (1) for $\alpha\text{-RuCl}_3$. With the help of the translation of the model using the alternative parametrization described in Sec. IC 2, we also emphasize important physical insights and intuition associated with the crystallographic reference frame. The 3D boundaries of the proposed parameter space in both parametrizations are shown, the representative choices of the model parameters that are used for the phase diagrams in Secs. III, IV, and IC 1 are suggested, and a comparison of the $\alpha\text{-RuCl}_3$ parameter sets with recent works is highlighted.

A. Constraints

According to our discussion in Sec. IC 1, the observables that are effective in restricting anisotropic terms of the spin model of α -RuCl₃ are the ones that (i) should occur only if such terms are present, (ii) should preferably depend on a distinct set of such terms to avoid redundancy of the empirical constraints, and (iii) should contain minimal or controllable quantum effects.

We identify three phenomenological constraints that can fulfill such a mission and provide a thorough discussion of them. In the end of Section II, Table I offers a comprehensive compilation of the previously proposed parameter sets for the anisotropic exchanges $\{K, \Gamma, \Gamma'\}$ of α -RuCl₃ [69–90], with the only general restriction of $K < 0$, which is consistently demonstrated by the first-principles guidance and spectroscopic measurements [70, 81]. Table I also shows the ability of these parameter sets to match the proposed phenomenological constraints. Since the number of entries in this compilation is significant, we also use histogram distributions of the data in these sets to showcase the proposed physical limits on the observables and the effect of the constraints on the possible ranges of the model parameters.

1. Tilt angle

The first proposed phenomenological constraint is the substantial tilt of the ordered moments out of the crystallographic plane of magnetic ions in the low-temperature zigzag state of α -RuCl₃ [21, 22], see inset of Fig. 5. This tilt angle has been measured by the neutron and resonant elastic x-ray scattering spectroscopies, which put its value to $\alpha \approx 35^\circ$ and $\alpha \approx 32^\circ$, respectively [26, 81, 104]. The sign of this angle was also important for the determination of the sign of the Kitaev K -term in α -RuCl₃ [81].

Needless to say, the isotropic exchanges cannot be responsible for the tilt, with the classical energy minimization connecting the tilt angle to a rather non-intuitive mix of all three anisotropic-exchange terms of the generalized KH model (2) [46, 64, 111]

$$\tan 2\alpha = 4\sqrt{2} \cdot \frac{\Gamma - K - \Gamma'}{7\Gamma + 2K + 2\Gamma'}. \quad (4)$$

In the crystallographic notations of the model (3), this expression becomes significantly more telling

$$\tan 2\alpha = \frac{4J_{z\pm}}{J_1(1 - \Delta) + 4J_{\pm\pm}}, \quad (5)$$

showing plainly that the tilt can only be induced by the term that explicitly connects the in-plane and the out-of-plane spin components, $J_{z\pm}$.

One can question the use of the classical expressions for the tilt angle to match the actual observations in α -RuCl₃. According to Ref. [64], there are also possible

differences between the calculated direction of the pseudospin in (4) and the experimentally measured direction of the magnetic moment.

For the first concern, prior comparisons to exact diagonalization for several representative sets of parameters have shown only insignificant quantum corrections to the tilt angle [64]. Similarly small deviation from the classical value of the out-of-plane tilt of the magnetic moments was recently observed in a strongly-fluctuating ground state of a related anisotropic-exchange model of the 1D compound CoNb₂O₆, where it was rationalized as due to a natural compensation of the contributions of different terms [120]. The conclusive DMRG check of the numerical correspondence of the tilt angle in the quantum and classical models for the parameters proposed in this work will be given in Sec. IV.

In order to account for these effects, and instead of fixing α to a particular value, we take a relatively broad span of $30^\circ \leq \alpha \leq 37^\circ$ as the physically allowed range of the tilt angle.

2. ESR gap

While the tilt angle criterion has been previously discussed [64], the second phenomenological constraint has received less attention, despite its clear advantages and being close in spirit to the standard approach to the problem of determining parameters in fluctuating magnets [46]. As was mentioned earlier, significant quantum fluctuations in the nominally polarized paramagnetic phase of α -RuCl₃ limit the insights that one can draw from such a state, compared to the case when fluctuations are fully quenched by the field [96–103].

Although limiting, they do not completely prohibit such insights, because some spectroscopies can be utilized in the fields that are much higher than the ones available to neutron scattering. Specifically, the field-dependence of the lowest-energy spin excitation at $\mathbf{k} = 0$ has been probed up to the high fields of 35 T using Raman and THz spectroscopies [80], with the ESR results essentially coinciding with them up to its feasibility range of 17 T [29], see Fig. 5. For the fields $\gtrsim 20$ T, quantum fluctuations in α -RuCl₃ are substantially quenched, leading to $\lesssim 20\%$ suppression of the ordered moment [22, 65], the number that can be used to gauge their overall effect.

All three techniques are consistent with each other and in their interpretation of the lowest excitation in their spectra as that of the single magnon-like spin-flip in the partially polarized ferromagnetic background [80, 105], to which we will refer to as the lowest “ESR mode.” The behavior of this mode differs markedly from the Zeeman-like linear field-dependence, typical of the isotropic magnets, with the high-field asymptote of E_0 vs H having a large positive shift. The latter follows straightforwardly from the quasiclassical result [46]

$$E_0 = \sqrt{h(h + \Delta E_g)}, \quad (6)$$

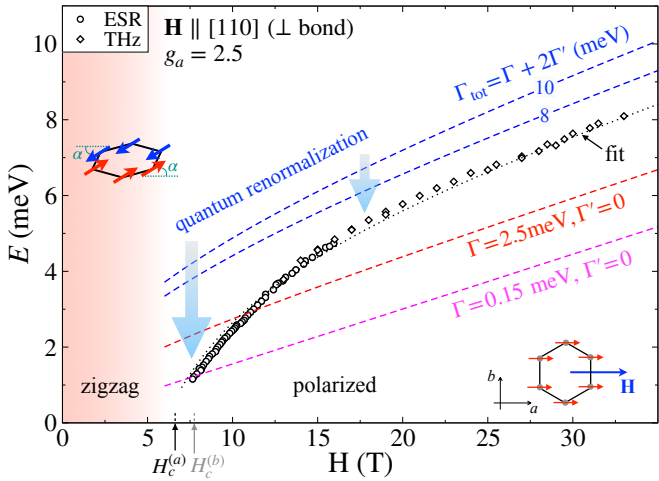


FIG. 5. ESR [29] and THz [80] data for the magnon energy, E_0 , at $\mathbf{k}=0$ vs field in the a -direction. Results from Eq. (6) for Γ_{tot} from Refs. [89] and [75] and for 8 meV and 10 meV. Arrows emphasize the downward renormalization by quantum fluctuations. Insets: sketches of the zigzag and polarized states and in-plane a and b directions.

with $h=g\mu_B H$ and the “ESR gap” ΔE_g

$$\Delta E_g = 3S(\Gamma + 2\Gamma') = -3SJ_1(1 - \Delta), \quad (7)$$

that depends on a subset of terms of the model (1), underscoring its utility as of the “orthogonal” constraint.

The ESR gap depends on a simple, but uninformative combination of Γ and Γ' in the generalized KH parametrization (2). In contrast, its explicit relation to the departure of the XXZ part of the model in the crystallographic frame (3) from the isotropic Heisenberg limit, $(1 - \Delta)$, is not only simple, but also explains the physical origin and generic character of the positive shift of the ESR mode. Given the large observed value of ΔE_g , it provides the most direct evidence of the strong deviation of the KH model of α -RuCl₃ from the Kitaev limit and a compelling argument for its natural description as an easy-plane J_1-J_3 ferro-antiferromagnet.

In Fig. 5, we reproduce the data for the energy of the lowest ESR mode from Refs. [29, 80] for the in-plane field perpendicular to the bond (a -direction), varying from the critical field $H_c^{(a)} \approx 7$ T to about 35 T, with the data for the b -direction, along the bond, being very similar. The high-field expansion of Eq. (6), $E_0 \approx h + a_0 + a_1/h$ provides the fit to the data. In this study, we use $g_a = g_b = 2.5$, in accord with the earlier estimates [62, 65, 121].

Qualitatively, quantum fluctuations should produce a downward shift of the “bare” quasiclassical mode in (6) due to a repulsion from the two-magnon states, which are also observed in Refs. [29, 80]. This effect is naturally stronger near the critical field, as is emphasized schematically in Fig. 5, where these states may overlap, according to the analysis of Ref. [80]. The downward renormalization has also been confirmed by exact diag-

onalization and selfconsistent spin-wave theory for representative parameter sets [46, 65].

This downward trend implies a logical *lower* limit on the value of the “bare” ESR gap, or $\Gamma_{\text{tot}} = \Gamma + 2\Gamma'$, as the unrenormalized theory result in (6) must be at least above the experimental curve in order to be able to reach it upon a downward renormalization.

To demonstrate the power of this criterion as a test for the existing parameter sets from Table I, we use Fig. 5 to show E_0 vs H from Eq. (6) for two representative $\Gamma_{\text{tot}} = \Gamma + 2\Gamma'$, with the lowest dashed line from Ref. [89] of the machine-learning approach and the second lowest from Refs. [75, 77], which is successful in describing the low-field phenomenology of α -RuCl₃. Both miss the high-field results by a significant margin, with the data suggesting substantially larger values of ΔE_g and the corresponding combination of Γ and Γ' . With the residual quantum fluctuations still present up to 35 T, our analysis suggests that Γ_{tot} cannot be less than ≈ 7.5 meV.

Importantly, quantum fluctuations are reduced in higher fields, which also puts a logical *upper* limit on ΔE_g and Γ_{tot} . As is made clear in Fig. 5 with the help of the quasiclassical results for E_0 vs H curves for $\Gamma_{\text{tot}} = 8$ and 10 meV, with quantum effects in magnetization being $\lesssim 20\%$, it would be very hard to justify Γ_{tot} to be larger than ≈ 10 meV, as this would imply unphysically large fluctuations in a strongly gapped high-field state.

Altogether, the high-field results for the ESR gap provide the lower and the upper bounds of the physically allowed range directly to the linear combination of the model parameters, $7.5 \text{ meV} \leq \Gamma + 2\Gamma' \leq 10 \text{ meV}$, which are used in our analysis below. The quantitative verification of the downward-renormalization effects in the field-dependence of the ESR gap is presented in Sec. IV, using ED for the quantum model with one of the representative parameter sets proposed in this work. This also serves as a validation of our strategy for constraining the anisotropic terms of the α -RuCl₃ effective model.

3. Critical fields

The third phenomenological constraint is counterintuitive. If the bond-dependent terms in the generalized KH model of α -RuCl₃ are significant, it is natural to inquire why the experimentally observed in-plane critical fields for the transition to the partially polarized paramagnetic phase in the two principal field directions are so close, $\Delta H_c^{\text{exp}} = H_c^{(b)} - H_c^{(a)} \approx 0.8$ T [67, 68, 105]; both fields are indicated in Fig. 5. Such a small difference would be natural for the nearly isotropic Heisenberg or pure KH models, but with the ESR gap suggesting substantial Γ and Γ' terms, small ΔH_c condition should be able to bind them in a way that is distinct from the other constraints.

One can use the quasiclassical expressions for the critical fields given below to calculate such ΔH_c for the parameter sets proposed in prior works, most of which put strong emphasis on the anisotropic terms in α -RuCl₃.

It is intriguing that *all* but one of them yield values of these quasiclassical estimates of ΔH_c that are not just larger, but typically an order of magnitude larger than the observed value—of the same magnitude as the $H_c^{(b)}$ and $H_c^{(a)}$ critical fields themselves, see Table I. The one exception, Ref. [89], fails the ESR gap criterion as it suggests a model which is close to the pure KH limit.

One concern for the critical fields being a phenomenological constraint is their expected strong quantum effects. However, while quantum fluctuations should considerably suppress the critical fields from their classical values [122], it would be very unnatural for their *difference* to change drastically [46]. This suggested lack of quantum effects in ΔH_c can be taken as a falsifiable prediction of our strategy, with the representative parameter sets proposed in this work given a numerical verification by DMRG in Sec. IV.

The transition from the field-induced paramagnetic to the zigzag phase corresponds to a closing of a magnon gap at the ordering vector associated with zigzag order [78, 86, 123]. This condition yields quasiclassical expressions for the transition fields in the two principal directions, $H \parallel a$ and $H \parallel b$ [46], perpendicular and parallel to the nearest-neighbor bond, respectively, see Fig. 1(b)

$$h_c^{(a)} = J + 3J_3 + \frac{1}{12}(5K - 5\Gamma - 16\Gamma') + \frac{1}{12}R_a, \quad (8)$$

$$R_a = \sqrt{(K + 5\Gamma + 4\Gamma')^2 + 24(K - \Gamma + \Gamma')^2},$$

$$h_c^{(b)} = J + 3J_3 + \frac{1}{4}(2K - \Gamma - 6\Gamma') + \frac{1}{12}R_b, \quad (9)$$

$$R_b = \sqrt{(2K + 7\Gamma + 2\Gamma')^2 + 32(K - \Gamma + \Gamma')^2},$$

where $h_c^{(\alpha)} = g_\alpha \mu_B H_c^{(\alpha)}$. Consistent with our proposed anisotropic strategy, the difference of the critical fields in (8) and (9) is a function of only anisotropic terms of the model, $\{K, \Gamma, \Gamma'\}$. Although not leading to significant new insights, rewriting the critical fields in the crystallographic language yields more compact expressions

$$h_c^{(a)} = J_1 + 3J_3 + \frac{1}{4}J_1(1 - \Delta) - \frac{1}{2}J_{\pm\pm} + \frac{1}{4}R_a, \quad (10)$$

$$R_a = \sqrt{(J_1(1 - \Delta) + 2J_{\pm\pm})^2 + 12J_{z\pm}^2},$$

$$h_c^{(b)} = J_1 + 3J_3 + \frac{1}{4}J_1(1 - \Delta) - J_{\pm\pm} + \frac{1}{4}R_b, \quad (11)$$

$$R_b = \sqrt{(J_1(1 - \Delta) + 4J_{\pm\pm})^2 + 16J_{z\pm}^2},$$

suggesting that some subtle near-cancellation of the anisotropic terms is needed to yield $\Delta H_c \approx 0$.

Aside from the quantum fluctuations suppressing $H_c^{(a)}$ and $H_c^{(b)}$ from their quasiclassical values, the interplane 3D couplings in α -RuCl₃ should also alter them, as discussed in Ref. [86]. However, since these 3D couplings are mostly isotropic [86], they are not expected to modify the functional expression for the field difference ΔH_c , thus, effectively, redefining only the combination of the

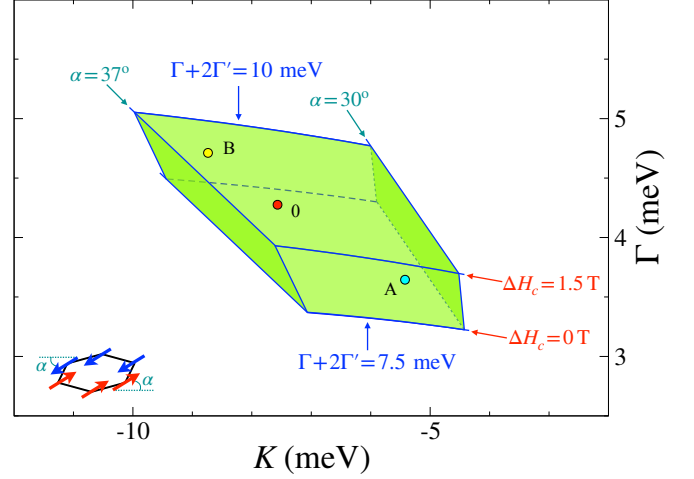


FIG. 6. The projection of the $\{K, \Gamma, \Gamma'\}$ parameter space on the K – Γ plane. The colored region is the subspace bounded by the phenomenological constraints for α -RuCl₃. Boundaries due to tilt angle α (4), critical fields difference ΔH_c (8) and (8), and $\Gamma + 2\Gamma'$ from the ESR gap (7), and representative parameter sets, Points 0, A, and B, are indicated.

isotropic exchanges of the 2D model (1), $J + 3J_3$ in Eqs. (8) and (9) or $J_1 + 3J_3$ in Eqs. (10) and (11), and can be absorbed into them. These couplings may also play an additional role in stabilizing the zigzag phase [86].

In α -RuCl₃, the in-plane critical field $H_c^{(a)}$ for the transition from the zigzag to the paramagnetic state found experimentally is ≈ 7 T and $H_c^{(b)} \approx 7.8$ T [26, 65, 67], see Fig. 5. There is an additional transition for $H \parallel a$ at ≈ 6 T, which has been identified with an interplane ordering of the zigzag planes [47, 67, 86] that is unrelated to the 2D physics of α -RuCl₃ discussed in this work. In the following analysis, the physical range of $0 \leq \Delta H_c \leq 1.5$ T is assumed to allow for modest quantum effects.

B. Parameter space

We now turn to restricting the three anisotropic terms of the generalized KH model (2) by applying phenomenological constraints proposed in Sec. II A. Our Figures 6 and 7 show the 2D projections of the 3D $\{K, \Gamma, \Gamma'\}$ parameter space on the K – Γ and Γ – Γ' planes, respectively, with the colored region corresponding to the physical subspace of α -RuCl₃ that is bounded by the constraints. In the figures, we also indicate the ranges of the physical observables responsible for the specific boundaries of this subspace, with the out-of-plane tilt angle α from Eq. (4) and the field difference ΔH_c from Eqs. (8) and (9). For the ESR gap ΔE_g in Eq. (7), we apply the constraint directly to the $\Gamma + 2\Gamma'$ combination.

The constraints can be seen as sufficiently, if not nearly “orthogonal,” in the sense of being nonredundant and resulting in a closed compact physical region in the 3D parameter space. While all three constraints are essential

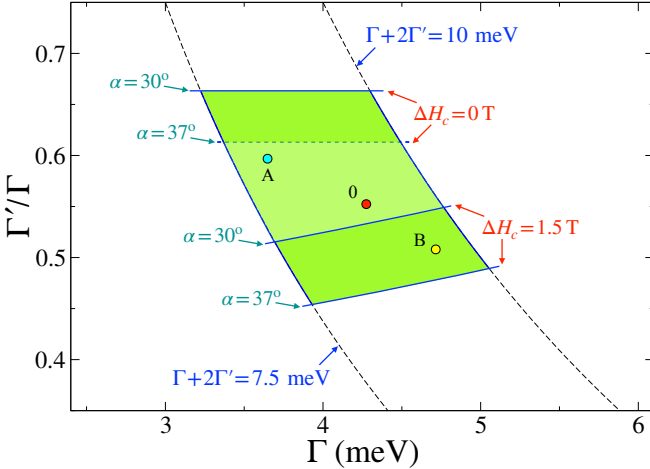


FIG. 7. Same as Fig. 6 with the projection on the Γ - Γ' plane.

for the physical bounds on all three parameters of the model, the rough account of their roles, summarized in Sec. IC1, can be recounted here. The main role of the ΔH_c constraint can be seen in strongly tying Γ' to Γ , with the resultant overall parameter range $0.45 \lesssim \Gamma'/\Gamma \lesssim 0.66$, followed by the ESR gap strongly limiting the physical values of Γ to the $3.2 \text{ meV} \lesssim \Gamma \lesssim 5.0 \text{ meV}$ range. The tilt angle can be seen as responsible for binding K to the range of $4.5 \text{ meV} \lesssim |K| \lesssim 10 \text{ meV}$. Obviously, these limits do not do the full justice to the picture as the constrained space is not orthorhombic, so fixing one of the parameters would narrow the allowed ranges for the others.

1. Representative parameters

In Figs. 6 and 7, one can see three points within the colored region. These are projections of the representative $\{K, \Gamma, \Gamma'\}$ sets from the advocated physical parameter subspace, chosen to span it along its longer axis.

These sets will be referred to as Point 0, roughly at the center of the physical subspace, and Point A and Point B, located toward the opposite ends of it, respectively. Their $\{K, \Gamma, \Gamma'\}$ coordinates and the values of the observables, α , Γ_{tot} , and ΔH_c , to which these parameter sets correspond, are given by

$\{K, \Gamma, \Gamma'\}$	α	Γ_{tot}	ΔH_c
Point 0: $\{-7.567, 4.276, 2.362\}$	35°	9.0	0.8 T
Point A: $\{-5.427, 3.647, 2.176\}$	32°	8.0	0.5 T
Point B: $\{-8.733, 4.714, 2.393\}$	36°	9.5	1.3 T

All parameters are in meV unless indicated otherwise.

The phase diagrams for Points 0 and A in the remaining J - J_3 parameter space of the model (1), such as the ones shown in Sec. IC1 for Point B, will be explored in detail in Sec. III, with their similarities and differences highlighted. The stability of the quasiclassical values of the observables to quantum effects for the Point 0 is verified by DMRG in Sec. IV B.

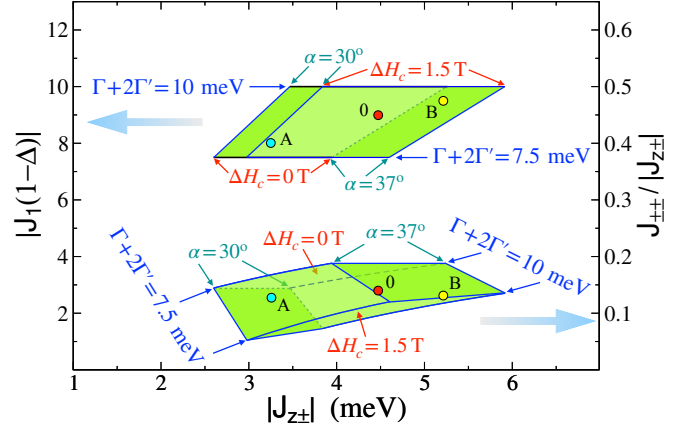


FIG. 8. Same as Figs. 6 and 7 for the crystallographic parametrization of the model (3): the $J_1(1 - \Delta)$ - $J_{\pm\pm}$ plane (left axis) and the $J_{\pm\pm}$ - $J_{z\pm}$ plane (right axis) are shown.

2. Alternative space

Our Figure 8 presents projections of the physical parameter space of α -RuCl₃ in the alternative crystallographic parametrization of the XXZ - $J_{\pm\pm}$ - $J_{z\pm}$ model (3). The corresponding anisotropic parameter space is also three-dimensional, with the $\{J_1(1 - \Delta), J_{\pm\pm}, J_{z\pm}\}$ coordinates. Fig. 8 shows projections of this 3D space on the $J_1(1 - \Delta)$ - $J_{z\pm}$ and $J_{\pm\pm}$ - $J_{z\pm}$ planes.

Given the discussion in Sec. II A, some of the phenomenological constraints proposed in this work have much more direct and instructive relation to the parameters of the model in the crystallographic reference frame. For the ESR gap, Eq. (7), the XXZ anisotropy parameter, $J_1(1 - \Delta)$, is constrained directly, hence the horizontal boundaries of the respective region in Fig. 8. Since the tilt angle, Eq. (5), is induced by the coupling of the in-plane to the out-of-plane spin components from the $J_{z\pm}$ term, its physical range is largely dictated by the constraints on the angle. In turn, while somewhat more complicated, the critical field difference ΔH_c is responsible for the bounds on $J_{\pm\pm}$.

An important insight provided by the crystallographic form of the model is the clear hierarchy in the magnitude of the physical parameters in this alternative space, which is seen in the representative Points 0, A, and B,

$\{J_1(1 - \Delta), J_{\pm\pm}, J_{z\pm}\}$	α	Γ_{tot}	ΔH_c
Point 0: $\{-9.0, 0.623, -4.469\}$	35°	9.0	0.8 T
Point A: $\{-8.0, 0.414, -3.252\}$	32°	8.0	0.5 T
Point B: $\{-9.5, 0.682, -5.211\}$	36°	9.5	1.3 T

Specifically, the largest is the (negative) $J_1(1 - \Delta)$, followed by $J_{\pm\pm}$, see Fig. 8. On the other hand, the physical range of $J_{z\pm}$ is nearly an order of magnitude smaller than that of the leading terms. While its small positive values will be important for the details of the incommensurate phases in the phase diagrams discussed in Sec. III, one expects a secondary role of this term to that of $J_{z\pm}$ [113].

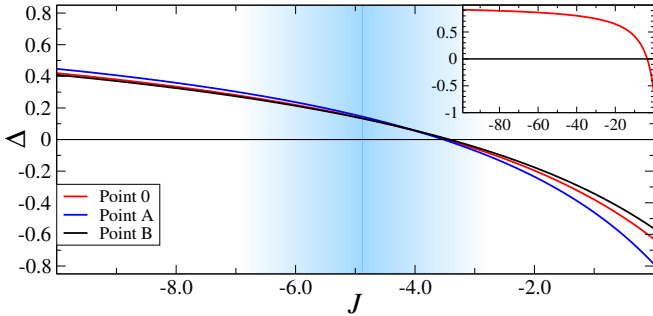


FIG. 9. The XXZ Δ of the model (3) vs J of the KH model (2) for Points 0, A, and B. Inset: Point 0 in a larger range.

A less obvious, but arguably more dramatic element of this hierarchy is the strongly easy-plane character of the model (3) in the physical space of α -RuCl₃. Since $J_1(1-\Delta)$ is the largest parameter, it already implies that the XXZ term cannot be close to the Heisenberg limit ($\Delta=1$) for any physically reasonable values of J_1 .

In order to determine a plausible range of Δ , one can rely on the broad expectations for the isotropic term J in the KH representation to be negative and not to exceed $|K|$ [46, 70, 83]. Using relations between the crystallographic and KH frames in Appendix A and taking $|K| \approx \Gamma_{\text{tot}}$ for the α -RuCl₃ range of parameters from Sec. II B, one can find that Δ should vary from about -0.5 at $J=0$ to 1 for $J \rightarrow -\infty$, crossing zero at $J \approx -\Gamma_{\text{tot}}/3$. These trends are verified for the Points 0, A, and B in Fig. 9. One can see that for the values of J relevant to α -RuCl₃ (shaded region), the XXZ anisotropy parameter Δ varies between -0.1 and 0.3.

Having $J_{\pm\pm}$ and Δ near zero suggests a simpler and more intuitive description of α -RuCl₃ by the easy-plane $J_1^{XY}-J_3$ FM-AFM model with strong bond-dependent $J_{z\pm}$ term, the perspective further explored below.

3. Comparison with Ref. [90]

Here we discuss in more detail recent results of Ref. [90], which has obtained nearest-neighbor exchanges for the α -RuCl₃ model from a completely different viewpoint from the phenomenological approach of our work. Their systematic perturbative derivation of the KH exchanges using microscopic treatment of the orbital model in the spirit of the original work by Jackeli and Khaliullin [24] has included the most relevant orbitals and their hoppings together with the octahedral distortion of the ligand environment. Their results are reproduced in our Fig. 10(a). The horizontal axis is the dimensionless parametrization of the octahedral distortion and the shaded region marks the range relevant to α -RuCl₃.

One can see a close accord of the hierarchy of the $\{K, \Gamma, \Gamma'\}$ terms in the shaded region of Fig. 10(a) with our suggested ranges in Sec. II B 1: the leading K -term, Γ close next, and, specifically, positive and sizable Γ' term,

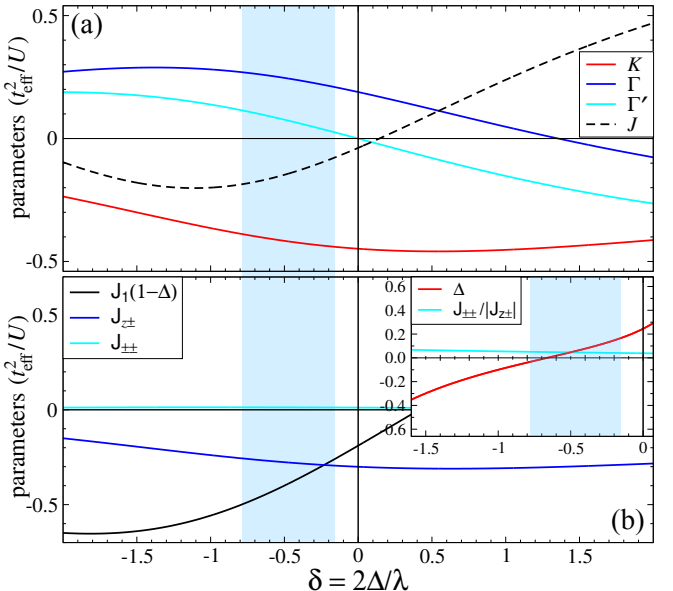


FIG. 10. (a) J, K, Γ , and Γ' from Ref. [90], δ is the octahedral distortion, shaded region is relevant to α -RuCl₃. (b) and inset: same data in the crystallographic parametrization (3).

originally proposed in Ref. [46]. Here and in Fig. 10(b), t_{eff}^2/U is the overall energy scale of the model parameters in this perturbative approach, see Ref. [90].

However, the most remarkable results are shown in Fig. 10(b). It is the same data from Ref. [90], but in the crystallographic parametrization of the $XXZ-J_{\pm\pm}-J_{z\pm}$ model (3). One can see all the aspects of the physical parameter space of α -RuCl₃ that are discussed in Sec. II B 2 above: leading $J_1(1-\Delta)$ that is followed by $J_{z\pm}$, a sub-leading $J_{\pm\pm}$ for all distortion values, with its ratio of $J_{\pm\pm}/|J_{z\pm}| \approx 0.1$ matching nicely the physical space in Fig. 8, and, most importantly, the value of Δ varying from -0.1 to 0.2 in the relevant region of Fig. 10(b).

Needless to say, such a close agreement on the qualitative and quantitative trends of the two very different approaches to the same problem is rather remarkable. It also provides a sign of the promising convergence on the physical parameter space of α -RuCl₃ for the effective $K\Gamma\Gamma'-J_3$ model.

4. Compilation of prior results

Our Table I presents a comprehensive compilation of the previously proposed $\{K, \Gamma, \Gamma'\}$ parameter sets of the generalized KH model (1) for α -RuCl₃, which are based on density-functional theory (DFT) [69–73] and various phenomenological, analytical, and numerical analyses [74–90]. Entries with the positive K values, which contradict broad phenomenologies [26, 81], are omitted. The reference is in the first and the abbreviated details of the approach are in the second column; all parameters are in meV unless indicated otherwise. For the few cases

Reference	Method	$K (< 0)$	$\Gamma (> 0)$	Γ'	$\alpha (\circ)$	$\Gamma + 2\Gamma'$	ΔH_c (T)
Kim et al. [69]	DFT+ t/U , P3	-6.55	5.25	-0.95	36.6	3.35	9.64
	DFT+SOC+ t/U	-8.21	4.16	-0.93	40.9	2.3	7.03
	same+fixed lattice	-3.55	7.08	-0.54	28.4	6.01	14.4
Winter et al. [70]	DFT+ED, C2	-6.67	6.6	-0.87	34.4	4.87	12.2
Hou et al. [71]	DFT+ t/U , $U = 2.5\text{eV}$	-14.4	6.43		41.1	6.43	7.96
	same, $U = 3.0\text{eV}$	-12.2	4.83		42.2	4.83	5.74
	same, $U = 3.5\text{eV}$	-10.7	3.8		43.2	3.8	4.36
Wang et al. [72]	DFT+ t/U , P3	-10.9	6.1		38.9	6.1	8.15
	same, C2	-5.5	7.6		30.2	7.6	13.3
Eichstaedt et al. [73]	DFT+Wannier+ t/U	-14.3	9.8	-2.23	38.3	5.33	18.1
Ran et al. [74]	LSWT, INS fit	-6.8	9.5		30.1	9.5	16.6
Winter et al. [75]	<i>Ab initio</i> +INS fit	-5.0	2.5		40.0	2.5	3.22
Suzuki et al. [76]	ED, C_p fit	-24.4	5.25	-0.95	47.3	3.35	6.76
Cookmeyer et al. [77]	thermal Hall fit	-5.0	2.5		40.0	2.5	3.22
Wu et al. [78]	LSWT, THz fit	-2.8	2.4		34.6	2.4	3.68
Ozel et al. [79]	same	-3.5	2.35		37.0	2.35	3.34
Sahasrabudhe et al. [80]	ED, Raman fit	-10.0	3.75		42.7	3.75	4.38
Sears et al. [81]	Magnetization fit	-10.0	10.6	-0.9	33.4	8.8	19.0
		-10.0	8.8		34.3	8.8	13.6
Laurell et al. [82]	ED, C_p fit	-15.1	10.1	-0.12	37.2	9.86	14.6
Suzuki et al. [83]	RIXS	-5.0	2.5	+0.1	39.8	2.7	3.03
Kaib et al. [84]	GGA+U	-10.1	9.35	-0.73	34.5	7.89	16.0
Andrade et al. [85]	χ	-6.6	6.6		33.1	6.6	10.6
Janssen et al. [86]	LSWT+3D	-10.0	5.0		40.0	5.0	6.43
Li et al. [87]	C_m , χ	-25.0	7.5	-0.5	44.8	6.5	9.03
Ran et al. [88]	polarized INS	-7.2	5.6		35.6	5.6	8.33
Samarakoon et al. [89]	Machine learning, INS	-5.3	0.15		36.4	0.15	0.11
Liu et al. [90]	downfolding	-5.0	2.8	+0.7	37.3	4.2	2.37
This work	realistic range	[-10.0,-4.4]	[3.2,5.0]	[1.8,2.85]	[30.0,37.0]	[7.5,10.0]	[0.0,1.5]
	point 0	-7.57	4.28	2.36	35.0	9.0	0.8
	point A	-5.43	3.65	2.18	32.0	8.0	0.5
	point B	-8.73	4.71	2.39	36.0	9.5	1.3

TABLE I. The proposed sets of $\{K, \Gamma, \Gamma'\}$ parameters for $\alpha\text{-RuCl}_3$ and values of the angle α , $\Gamma + 2\Gamma'$, and ΔH_c that follow from them according to Eqs. (4), (7), and (8) and (9), respectively. For all the results, only the nearest-neighbor anisotropic exchanges from the proposed parameter sets were used. The acronyms are linear spin-wave theory (LSWT), spin-orbit coupling (SOC), inelastic neutron scattering (INS), resonant inelastic x-ray scattering (RIXS); “P3” and “C2” refer to the lattice symmetry. Representative sets of Points 0, A, and B, and proposed ranges are from Sec. II B 1, see the text.

of the lower symmetry of the model, the bond-averaged values of the exchange parameters were used.

The last three columns of the Table I list the values of the key physical observables, tilt angle α , the $\Gamma + 2\Gamma'$ combination for the ESR gap ΔE_g , and critical field difference ΔH_c , which follow from the proposed $\{K, \Gamma, \Gamma'\}$ sets according to Eqs. (4), (7), and (8) and (9), respectively. These values are highlighted in bold in cases where they fall within, or come close to the suggested realistic ranges. The latter are listed at the bottom of the table together with the physical bounds for $\{K, \Gamma, \Gamma'\}$ from Figs. 6 and 7 and representative sets of Point 0, A, and

B discussed above, see Sec. II A and Sec. II B.

We note here again that the $KJ\Gamma\Gamma' - J_3$ model considered in this work is an effective one, with the nearest-neighbor exchange matrix encapsulating *all* anisotropic terms, while some of the microscopic studies listed in Table I also allow such terms in the more extended exchanges [70–75]. This may account for the lack of the significant nearest-neighbor Γ' term in such models and lead to a better agreement with the proposed phenomenological constraints if the additional exchanges are included.

To provide a graphical presentation of the variation of the entries in the data compilation of Table I (28 entries, excluding our own), we use the histograms in Figures 11,

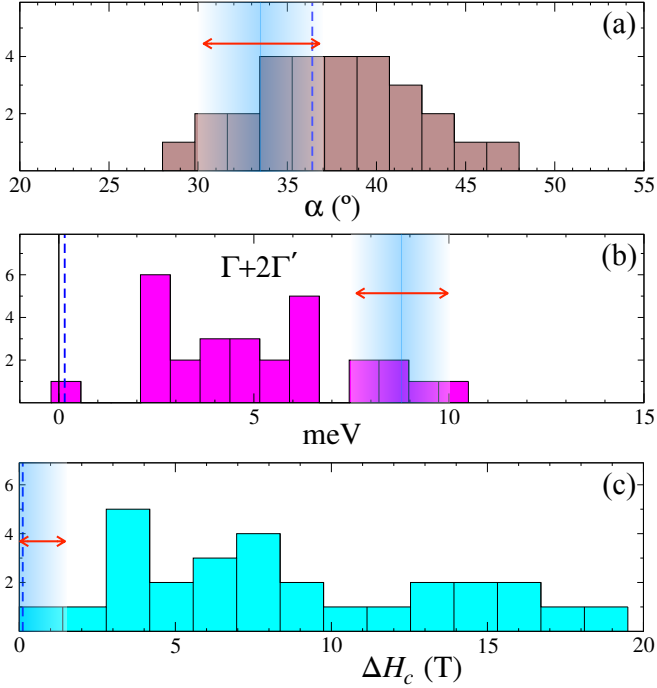


FIG. 11. Histograms of the observables from Table I, excluding present work. Shaded regions are physical limits (see text) and vertical dashed are for the data from Ref. [89].

12, and 13 to show the wide distribution of the prior attempts at the model parameters, highlight the physical limits on the observables proposed in our work, and emphasize the resultant effect of the constraints on the possible ranges of the model parameters. The physical limits discussed above are shown by shaded regions and vertical dashed lines correspond to a representative set of this compilation from the second to last entry, Ref. [89], elaborated on below in more detail.

As one can see in both Table I and Fig. 11(a), about half of the entries correspond to the tilt angle range close to the physical one. However, for the ESR gap in Fig. 11(b) and in the second to last column of Table I, only about 20% of them hit within the physical bounds. For the last column and Fig. 11(c), only one parameter set matches the range of the empirical critical field difference, and, arguably, for a wrong reason.

This set is from Ref. [89] that extracted effective model parameters of α -RuCl₃ from the INS data using machine learning. It has neglected Γ' and their resultant parameter set has near-zero Γ . Because of that, this set fails the ESR gap criterion, which requires a large $\Gamma + 2\Gamma'$ combination, while satisfying the remaining two of the phenomenological constraints put forward in our work. Its ability to match ΔH_c range is because the pure $K-J$ model always yields $\Delta H_c \equiv 0$, see Eqs. (8) and (9).

One can argue that a redo of the same analysis with no artificial restrictions in the model and with additional experimental input, which can improve the lack of orthogonality in their phenomenological constraints, may

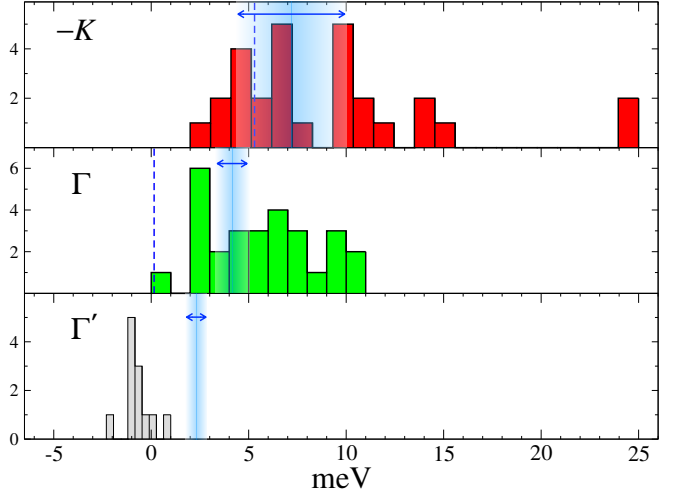


FIG. 12. Same as in Fig. 11 for $\{K, \Gamma, \Gamma'\}$ from Table I.

open the full potential of this approach and lead to a convergence of our parameter sets.

The rest of the entries in Table I that match the physical ranges of both tilt angle *and* ESR gap, fail at the remaining criterion, all yielding ΔH_c in excess of 13 T.

Lastly, the orbital model expansion study of Ref. [90], highlighted in Sec. II B 3 as showing great similarity to our results, suggested a representative set (the last entry in Table I) that has likely suffered from the choices of the smaller overall t^2/U scale for their parameters and a somewhat conservative value of the octahedral distortion δ , leading to a positive, but insufficiently large Γ' . A reasonable adjustment in both should produce a set not far from the ones proposed in this work.

Following our discussions in Sec. II B, the proposed constraints on the physical observables lead to important bounds on the model parameters. In Fig. 12, we highlight these bounds with the backdrop of the distributions of K , Γ , and Γ' from Table I. Needless to say, the phenomenological constraints lead to a significantly narrower physical parameter space, also visualized in Figs. 6 and 7. Our Fig. 12 reinforces the statements that are already made above. For an adequate description of the α -RuCl₃ phenomenology within the effective model, a positive Γ' -term is unavoidable, a significant Γ -term is necessary, and fairly tight limits on all three anisotropic exchanges can be established.

In Fig. 13, the same parameter sets from Table I are recast into the alternative crystallographic parametrization, with the actual values of the $\{J_1(1 - \Delta), J_{\pm\pm}, J_{z\pm}\}$ parameters of the model (3) given in Table II in Appendix A. Although not listed in Table I, the values of the J -term of the KH model (2) were used to obtain the histogram of the XXZ anisotropy Δ , see inset.

Aside from demonstrating the effect of phenomenological constraints that lead to a significantly narrower physical parameter space in these alternative axes, the crystallographic language underscores important com-

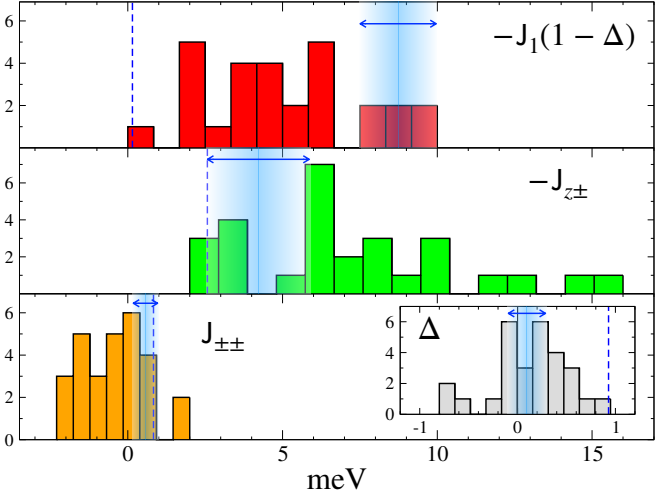


FIG. 13. Same as in Fig. 12 for the $\{J_1(1 - \Delta), J_{\pm\pm}, J_{z\pm}\}$ parameters of the model (1) in the crystallographic parametrization (3), see also Table II in Appendix A.

mon trends in most of the prior attempts at the $\alpha\text{-RuCl}_3$ parameters. Whether they match the proposed physical parameter space or not, the majority of them respects the hierarchy of terms proposed in this work: the two leading ones, $J_1(1 - \Delta)$ and $J_{z\pm}$, and a subleading $J_{\pm\pm}$.

Especially notable is another trend. As is laid plain in Fig. 13, *all* prior works with no exception suggest an easy-plane character of the ferromagnetic nearest-neighbor exchange in their $\alpha\text{-RuCl}_3$ modeling, showing $|\Delta| < 1$. In retrospect, the strongly easy-plane character of the model (3) is one of the most direct arguments that the parameter space of $\alpha\text{-RuCl}_3$ is far away from the Kitaev limit.

In a sense, the crystallographic representation of the model offers a lens that allows one to see the commonality of all earlier assessments of $\alpha\text{-RuCl}_3$ phenomenologies, suggesting a broader agreement between them as all pointing in a similar direction.

C. Summary on physical parameters

In this Section, we have demonstrated that the available phenomenologies should allow one to overcome the uncertainty in the model parameters for $\alpha\text{-RuCl}_3$ using observables that are induced by the anisotropic terms, see Sec. II A. The outline of the advocated parameter space and selected representative choices of the anisotropic exchanges, which will be used in the next Section, have been proposed, see Sec. II B 1. A systematic analysis of the prior attempts at the $\alpha\text{-RuCl}_3$ parameters in the context of the proposed phenomenologies has been provided, see Secs. II B 3 and II B 4.

Important physical insights and intuition associated with the alternative crystallographic reference frame parametrization have been highlighted in Secs. II B 2 and II B 4. They will be expanded upon below within the dis-

cussion of the phase diagrams relevant to $\alpha\text{-RuCl}_3$ parameter space, also offering a connection to the broader class of paradigmatic models in frustrated magnetism, thus providing a wider context to the studies of $\alpha\text{-RuCl}_3$.

III. PHASE DIAGRAMS

The purpose of the next two Sections is twofold. The first is to explore the remaining parameter space of the model (1) for the representative anisotropic parameter sets suggested above in order to pinpoint the ultimate parameter region for $\alpha\text{-RuCl}_3$ and to identify proximate phases that can be relevant to its properties. The second is to provide a better understanding of such phases and to characterize them with the help of numerical methods. We also use the opportunity to highlight the close agreement of various approaches to the derivation of these phase diagrams and to demonstrate that our anisotropic strategy outlined in Sec. IC 1 allows one to reign in on the otherwise prohibitively costly numerical exploration of the $\alpha\text{-RuCl}_3$ model parameter space.

A. $J\text{-}J_3$ phase diagrams of the KH model (1)

With the logic for fixing anisotropic exchanges articulated in Sec. IC 1 and executed in Sec. II above, the remaining two parameters of the effective model (1) of $\alpha\text{-RuCl}_3$ in the generalized KH representation are the isotropic J and J_3 exchanges. As highlighted in Sec. IC 1 for the representative set of $\{K, \Gamma, \Gamma'\}$ for Point B from Sec. II B 1 and Table I, the relevant region of the parameter space resides in the $J < 0$ and $J_3 > 0$ quadrant of the 2D $J\text{-}J_3$ phase diagram of the model, conforming to the general expectations [46, 70, 75, 82].

1. Phase diagrams by LT and ED methods

Here, we provide a detailed analysis of such phase diagrams and elaborate on the technical details of the approaches that are used for their derivation. Setting $\{K, \Gamma, \Gamma'\}$ to Point 0, we show the phase diagram in the $J\text{-}J_3$ plane in Figure 14, and for Point A in Figure 15. Both of these phase diagrams have regions consistent with the phenomenology of $\alpha\text{-RuCl}_3$.

In Fig. 14(a) and Fig. 15(a), the $J\text{-}J_3$ phase diagrams are obtained by the quasiclassical Luttinger-Tisza (LT) approach, which allows us to find spin arrangements of the classical spins that minimize their energy. The modern version of the original LT approach [106–109] involves diagonalization of the exchange matrix of the classical model in the momentum space, and the lowest eigenenergy, corresponding ordering vector, and associated types of spin arrangement are identified by a scan through reciprocal space and a Fourier transform back into the real space. It has been widely

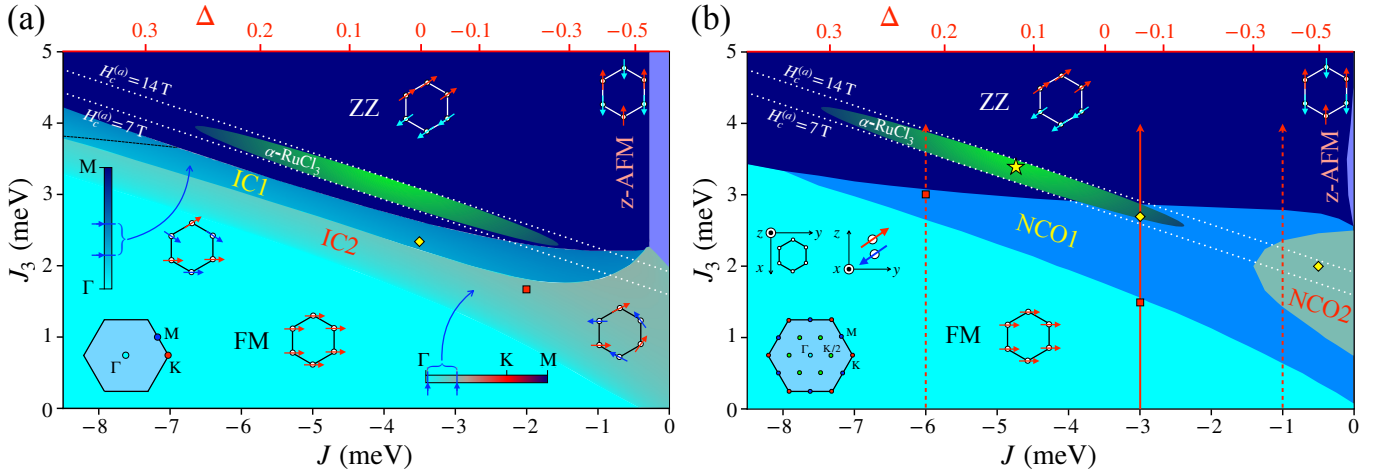


FIG. 14. The J – J_3 phase diagram of the model (1) for the Point 0 parameter set, see Sec. II B 1 and Table I, in the $J < 0$ and $J_3 > 0$ quadrant: (a) by the LT and (b) by ED. The ZZ, FM, AFM, IC, and NCO phases are designated and sketched using the xy plane for the lattice and the yz plane for the spin orientation. The upper horizontal axis is the XXZ parameter Δ in the crystallographic axes (3). Slanted dashed lines mark the boundaries of the parameter region for $\alpha\text{-RuCl}_3$ from the constraints on $H_c^{(a)}$ from Eq. (8), the star symbol in (b) is a representative point from that region, see Sec. III A 2. Vertical solid and dashed arrows in (b) show the extent of the DMRG scans discussed in Sec. IV A. Squares and diamonds are representative points in the IC phases for (a) LT and (b) DMRG non-scans, see Sec. IV A. Insets: (a) color-coded bars for the ordering vector in the IC phases and the first BZ with the high-symmetry points, (b) allowed momenta of the ED cluster in the first BZ.

used in the studies of the anisotropic-exchange models [61, 110, 112, 113, 124, 125], in which classical ground-state spin configurations are often not obvious. The implementation of the LT method is computationally cheap and straightforward (see Appendix B), with the area shown in Fig. 14(a) and Fig. 15(a) containing a grid of several hundreds points in both the J and J_3 directions.

In Figs. 14(b) and 15(b) we show similar phase diagrams obtained from ED. The reduction of the parameter space is essential in making this feasible. To reduce the effort of mapping out the phase diagrams, sets of 1D sweeps along various lines through the plane are performed [43, 65, 118, 125, 126]. At individual points along a line, an ED using a 24-site cluster with all space-group symmetries of the lattice is performed. The second derivative of the ground-state energy with the sweep parameter, $\partial^2 E_0 / \partial J_{(3)}^2$, is used to find phase boundaries, and the static spin structure factor, $\mathcal{S}(\mathbf{q})$, is analyzed to identify ordered states, see App. C for details.

The FM, AFM, and ZZ phases were identified by the dominant peak of $\mathcal{S}(\mathbf{q})$ at the corresponding ordering vector, with the insets in Figs. 14(b) and 15(b) showing the allowed momenta of the 24-site cluster in the first Brillouin zone. In the cases with no definite dominance of a specific \mathbf{q} -point in $\mathcal{S}(\mathbf{q})$, the states received the “non-commensurate” (NCO) designation. Peaks in the energy derivatives $\partial^2 E_0 / \partial J_{(3)}^2$ are associated with the phase boundaries and their relative sharpness can be suggestive of the order of the phase transition [125, 126].

The vertical dashed and solid lines in Figs. 14(b) and 15(b) show the direction and extent of the 1D DMRG “scans,” which will be discussed in Sec. IV together with the analysis of the IC phases at the representative points, marked by the squares and diamonds.

The resultant side-by-side comparison of the LT and ED phase diagrams in Fig. 14 and Fig. 15 is revealing. Very different methods, having very different limitations, one is classical and the other constrained by the finite-size effects, both point to a very similar structure of the phase diagram with a rather remarkably close *quantitative* correspondence of their boundaries and arrangements.

In broad strokes, large sectors of the phase diagrams are occupied by the ZZ and FM phases, both discussed as prominently present in the relevant phase space of $\alpha\text{-RuCl}_3$ by prior analyses [65, 70, 75, 83].

The z-AFM phase at low values of $|J|$ has Néel order with spins pointing along the z axis, not unlike the Ising- z phase discussed recently for the J_1 – J_3 FM-AFM model [43, 116, 117], where it is stabilized by strong quantum fluctuations due to frustrating in-plane interactions. However, here its origin is simpler, as the out-of-plane order is also promoted by $\Delta < 0$, as can be seen from the upper horizontal axis in Figs. 14 and 15. This means that the out-of-plane nearest-neighbor exchange in the crystallographic parametrization (3) is antiferromagnetic, cooperating with the J_3 term. As we discuss below, this region is likely irrelevant to $\alpha\text{-RuCl}_3$ for different reasons.

According to the LT phase diagrams in Figs. 14(a) and 15(a), the FM and ZZ phases are separated by the sequence of two incommensurate phases, IC2 and IC1. While the IC phases are regularly found in the extended KH model [46, 57, 58, 91], they are rarely analyzed. In our case, the ordering in the IC2 and IC1 phases correspond to two variants of the deformed counter-rotating spin-helices, discussed in detail in Sec. IV, with the \mathbf{Q} -vectors and corresponding periodicities varying according to the color maps shown in the insets.

For the IC2 phase, the \mathbf{Q} -vector is along the ΓK di-

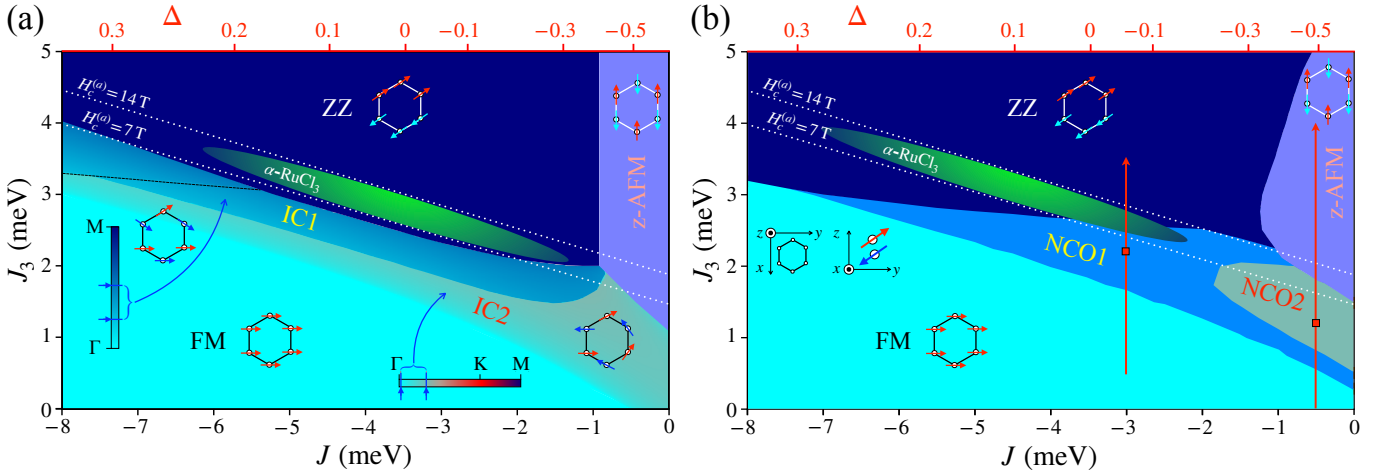


FIG. 15. The J – J_3 phase diagrams, same as in Fig. 14, for the Point A set, see Sec. II B 1 and Table I.

rection and it evolves from a value that is imperceptibly close to the Γ point, suggesting a smooth evolution from the FM state, followed by a jump to the ΓM direction when crossing to the IC1 phase, but with nearly the same value of $|\mathbf{Q}|$. In fact, according to LT, the two phases at that transition correspond to very shallow energy minima and are close to the other IC states with the intermediate \mathbf{Q} directions. The transition from the IC1 to ZZ is by a finite jump in \mathbf{Q} to the ordering vector of the ZZ phase at the M-point and is significantly first order. Although the finite-size effects in ED do not allow it to contribute decisively to the discussion of the nature of the IC phases, the widths of the peaks in the second derivative of ED energy at the FM-NCO1 and NCO1-ZZ boundaries are not inconsistent with the former being second and the latter being first order. Further verifications of these traits are provided by DMRG in Sec. IV.

As has been noted in the past, the LT method may fail to satisfy its own selfconsistency constraints for some of the phases, specifically the spin length, see Appendix B, formally finding groundstates that are deemed unphysical. Such “failures” have been interpreted as the sign of the more complicated multi- \mathbf{Q} phases [113, 124], candidate spin-liquid regions [110], and other states [127]. In our case, LT constraints are satisfied for all phases with the commensurate ordering vectors, the FM, ZZ, and AFM in Figs. 14, 15, and 2, and for the stripe phase in Figs. 4 and 16. But the IC phases obtained by the LT approach do violate the spin-length constraint and formally fall under the “unphysical” category.

However, the ability of the LT method to consistently produce states that are lower in energy than the competing classical ones at the cost of not preserving spin length can be seen as a blessing in disguise instead of being unphysical. This is because it may allow it to mimic quantum effects of the fluctuating states that are not conserving the length of the ordered moments either; a similar sentiment has also been expressed in Ref. [128].

This conjecture will receive rather spectacular support from the analysis of the character of the IC counter-

rotating helical phases, with their periods, mutual orientations of the \mathbf{Q} -vectors with the planes of spin rotations, and even phase shifts of the spirals, all being in close *quantitative* accord between the LT predictions and that of the DMRG results discussed below in Sec. IV, yielding additional remarkable agreements and insights.

2. Where is α -RuCl₃?

Last, but not least, is the study of additional constraints on the α -RuCl₃ parameters in the J – J_3 plane.

At the quasiclassical level, the out-of-plane tilt angles (4) that closely match magnetic order in α -RuCl₃ should be the same throughout the ZZ regions of Figs. 14(a) and 15(a), fixed by the choices of anisotropic parameters of Point 0 and Point A, respectively. Other phases that are present in the phase diagrams can only constrain the values of $|J|$ and J_3 from below.

However, as we argue here, one can devise a much stronger constraint on a combination of the two remaining isotropic parameters using phenomenologies that have already been introduced. Although the difference of the critical fields for the transition to the paramagnetic phase ΔH_c has been utilized as a constraint for anisotropic exchanges, the values of the critical fields themselves have not been exploited yet. As one can see in Eqs. (8) and (9), both $H_c^{(a)}$ and $H_c^{(b)}$ fields depend on the same linear combination of $J + 3J_3$, making it a natural variable [46] for another strong empirical constraint that binds J and J_3 terms via the experimental value of one of the critical fields.

Each of the panels in Figs. 14 and 15 shows a straight dashed line with a constant slope of $J_3 = -J/3$. They correspond to the solutions of Eq. (8) with the experimental value of $H_c^{(a)} = 7$ T [26, 65, 67]. Another line with the same slope is for the value of $H_c^{(a)}$ that is twice as high. The second line is introduced because the critical fields are expected to be suppressed by quantum fluctuations, with the theoretical calculations of that effect for the KH models suggesting it potentially reaching a factor

of two [65, 122]. One can see that the lines in Figs. 14 and 15 carve a narrow strip of the J – J_3 space, altogether suggesting very effective additional bounds on the physical parameters of α -RuCl₃.

One may wonder why this strip is so narrow despite the doubling of the “bare,” unrenormalized critical field from 7 T to 14 T. This is because a relatively small change of J_3 by 0.4 meV in the $J+3J_3$ combination readily modifies H_c in Eq. (8) by about 7 T.

In the phase diagrams in Figs. 14 and 15, the acceptable range of $|J|$ is also restricted from below by the competing phases. It is also rather unlikely for $|J|$ to exceed the value of $|K|$, restricting it from above [46, 70].

Altogether, the “complete” sets of the prospective α -RuCl₃ parameters for the model (1) should be chosen from the narrow ranges that are marked by the elongated ellipses in the J – J_3 planes in Fig. 14, Fig. 15, and Figs. 2 and 3, for the Point 0, A, and B anisotropic parameter sets, respectively.

One of such choices is marked by the star symbol in Fig. 14(b). It corresponds to the following complete set of the model (1) parameters, all in meV,

$$\{ K, \Gamma, \Gamma', J, J_3 \}, \quad (12)$$

$$\text{Point } \star : \{ -7.567, 4.276, 2.362, -4.75, 3.4 \}$$

which is, of course, a combination of the anisotropic parameter set of Point 0, see Sec. II B 1, and the choice of the $\{J, J_3\}$ pair from the middle of the allowed region.

By fixing the isotropic exchanges, the parameter set for α -RuCl₃ is complete. It is not a unique choice, as both J and J_3 can be adjusted according to the allowed range, and so can be anisotropic parameters, in a co-ordinated fashion, see Sec. II B. Nevertheless, these adjustments may not be significant and are not expected to lead to drastically different physical outcomes, as the comparison between phase diagrams for the Point 0, A, and B sets in Figs. 14, 15, 2, and 3 indicates.

Moreover, the complete Point \star parameter set (12) can be used to test predictions and assumptions of the present study, as well as the other phenomenologies. Specifically, using Eqs. (8) and (9), this parameter set yields the “bare” critical fields $H_c^{(a)} = 11.7$ T and $H_c^{(b)} = 12.5$ T, maintaining their difference at the physical 0.8 T. One of the key hypotheses of our anisotropic strategy is that this difference does not change drastically, while the fields themselves get suppressed considerably by quantum effects, see Sec. II A. We will provide a full vindication of both expectations using DMRG in Sec. IV B.

Another test is the verification by DMRG of the same out-of-plane tilt angle of spins throughout the ZZ phase for a given choice of $\{K, \Gamma, \Gamma'\}$ in Figs. 14 and 15, which is also expected to stay within the physically allowed range for α -RuCl₃ in the quantum limit. These selfconsistency checks of our anisotropic strategy for the quantum model will also be presented in Sec. IV B.

Since we return to the discussion of the model (1) in the crystallographic parametrization (3) in the next Section, it is useful to reflect on one more common thread

that is exposed in the phase diagrams in Figs. 14 and 15. Using the upper horizontal axis for the XXZ anisotropy parameter Δ , one can see that the relevant region for the α -RuCl₃ parameters resides solidly in the range of $-0.1 < \Delta < 0.3$, in agreement with the discussions in Secs. II B 2, II B 3, and II B 4.

It is also useful to rewrite the representative Point \star parameter set (12) in these axes (in meV except for Δ)

$$\{ J_1, J_{\pm\pm}, J_{z\pm}, \Delta, J_3 \}, \quad (13)$$

$$\text{Point } \star : \{ -10.272, 0.623, -4.469, 0.124, 3.4 \}$$

to emphasize this feature. Here, the $J_{\pm\pm}$ term is secondary as before, with J_1 and $J_{z\pm}$ dominating.

Lastly, we remark on the implications of the easy-plane, $\Delta \approx 0$ XXZ character of the α -RuCl₃ parameter space. As one can easily obtain from the relations between different parametrizations in App. A, the pure K – J model, together with its Kitaev-only points, must reside in the plane of $\Delta = 1$, which places α -RuCl₃ far away from that plane from the outset. This simple understanding, together with a straightforward phenomenology that allows one to detect significant XXZ anisotropy in the material suspects, see Sec. II A 2, may serve as important guidance for the studies of the other Kitaev candidates.

B. J_1^{XY} – $J_{z\pm}$ – J_3 phase diagram

As repeatedly argued above, the crystallographic-axes parametrization (3) not only helps with a better description of α -RuCl₃, it can also offer a transparent and intuitive perspective to the studies of anisotropic-exchange systems in general. It allows one to take a broader conceptual view on the studies of the generalized KH and other anisotropic-exchange models, placing them in a more tangible context within studies in frustrated magnetism.

For α -RuCl₃, we have made it clear that its model description favors the dominant XY -like ($\Delta \approx 0$) ferromagnetic J_1 combined with a sizable anisotropic bond-dependent $J_{z\pm}$, complemented by the isotropic antiferromagnetic J_3 , see Secs. IC 2, II B 2, II B 3, II B 4, and III A 2. The residual XXZ anisotropy Δ and $J_{\pm\pm}$ can be treated as secondary in their physical outcomes and studied as quantitative additions to the main model.

Here, we analyze the phase diagram of this simplified and physically justified J_1^{XY} – $J_{z\pm}$ – J_3 model. Because of the three-dimensional parameter space, and given the redundancy of the sign of the $J_{z\pm}$ term [113], one can explore the entirety of its parameter space with the help of the polar parametrization, shown in the inset of Fig. 16(a), with the $\{J_1, J_3\}$ pair parameterizing polar variable and $J_{z\pm}$ the radial one in units of $J_1^2 + J_{z\pm}^2 + J_3^2 = 1$.

1. LT polar phase diagram and other details

Our Figure 16(a) presents the phase diagram obtained by the LT method as in Figs. 14(a) and 15(a) above. In addition to the ZZ, FM, and IC phases, this phase diagram features AFM and stripe phases. The former occurs

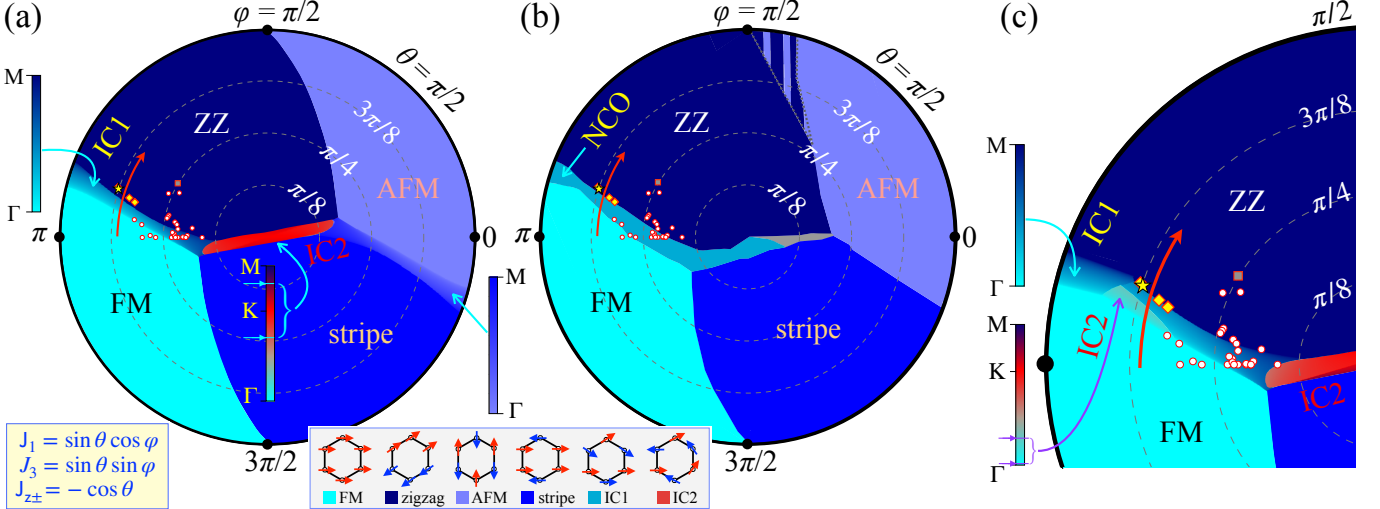


FIG. 16. Polar phase diagrams of the model (3) for $\Delta=0$. In (a) and (b) $J_{\pm\pm}=0$, in (c) $J_{\pm\pm}=0.05$, in units of $J_1^2+J_{z\pm}^2+J_3^2=1$. (a) and (c) are obtained by LT and (b) by ED methods, respectively. J_1 and J_3 encode polar and $J_{z\pm}$ radial coordinates, see inset in (a). Other details include sketches of the phases, color-bars for the \mathbf{Q} -vectors in the IC phases, projections of the data sets from the prior works, representative Point \star , and DMRG scan path from Fig. 14(b), see the text.

for the antiferromagnetic sign of J_1 and the latter mirrors the ZZ phase. The incommensurate phase sandwiched between them, in turn, mirrors the IC1 phase separating FM and ZZ, already familiar from the Cartesian phase diagrams in Sec. III A.

The incommensurate phase in the center of the circle has a \mathbf{Q} -vector that is continuously evolving along the TK line, normal to the bond of the honeycomb lattice, and then along the KM BZ boundary, as is shown in the color-coded bar. It is labeled as IC2 as it belongs to the same phase as the IC2 phase in Figs. 14(a) and 15(a), with both of them corresponding to the same type of the counter-rotated, deformed, and slightly tilted helix (spiral), as will be further discussed in Sec. IV.

While the \mathbf{Q} -vector in the IC2 phase evolves within the limits marked on the color bar, similar to the finite spans for both IC1 and IC2 in Figs. 14(a) and 15(a), the IC1 phase and its AFM-stripe mirror in Fig. 16(a) span the entire range between the Γ and M points. This is due to the $J_{z\pm}=0$ circumference of this phase diagram, which corresponds to the pure J_1-J_3 model. In this limit, the classical IC1 is a coplanar, co-rotating spiral continuously interpolating FM and ZZ [115, 116]. Away from the boundary, the IC1 phase turns into a deformed counter-rotated helix with a finite range of the \mathbf{Q} -vector that is parallel to the bond of the honeycomb lattice, see Sec. IV.

The inset in Figs. 16(a) and 16(b) provides sketches of the phases and emphasizes the differences between the propagation vectors in the IC1 and IC2 phases.

There are small circles in Fig. 16, which represent projections of all individual α -RuCl₃ parameter sets listed in Table I onto the $\Delta=J_{\pm\pm}=0$ plane of the phase diagram. While some of the parameters that are necessary to obtain the coordinates for such projections are made available in Table II in App. A, we do not list J and J_3 values of these individual sets in this work.

The small square with a darker shading corresponds to the machine-learning effort of Ref. [89], discussed in Secs. II A 2 and II B 4. The group of three diamonds are the sets listed in Table III in App. D that were proposed in Ref. [46], which has used some of the same types of phenomenological constraints on the α -RuCl₃ parameters as the ones used in the present work. These sets were deliberately not included in Table I for the sake of not skewing independent distribution of parameters from the prior literature. The projection of the representative Point \star set from Fig. 14(b) and Sec. III A 2 is shown by the star symbol. Although it appears close to one of the sets from Table III in App. D, the parameters in the sets are rather different.

An important benefit of this comparison and the clear advantage of the bird's-eye view of the polar phase diagrams demonstrated in Fig. 16 is in making apparent the commonality of the trends among the prior, although not always successful, hunts for the adequate description of α -RuCl₃ and its phenomenologies.

In addition to Point \star from the Cartesian phase diagram in Fig. 14(b), one additional correspondence is brought into the polar field of view of Fig. 16 by the red line with the arrow that traverses FM, IC1, and ZZ phases at a fixed radius. It is a projection of the DMRG scan path at $J=3$ in Fig. 14(b), which closely corresponds to the XXZ anisotropy value of $\Delta=0$, see the upper axis. As all anisotropic terms in Fig. 14(b) are at Point 0, by fixing J (and Δ) the scan changes only J_3 . For the polar representation in Fig. 16, changing J_3 corresponds to varying the ratio of J_3/J_1 and traveling along the radial path. Altogether, this reference scan helps to relate the view provided by the Cartesian phase diagrams in Sec. III A and the polar phase diagrams in Sec. III B as offering different slices through the same higher-dimensional parameter space.

2. ED polar phase diagram

Our Fig. 16(b) offers another demonstration of the power of the numerical tour-de-force exploration of the 2D parameter space using ED in the 24-site cluster.

With the technical description of the approach provided in Sec. III A 1 and App. C, the phase diagram in Fig. 16(b) is based on the combination of the 1D radial and polar sweeps, 1000 points each. For the radial sweeps, the variable θ was varied from 0 to $\pi/2$ for fixed polar angles φ . For the polar sweeps, φ angle was swept from 0 to 2π at fixed θ . In addition, two spiral sweeps were performed, in which both θ and φ variables changed, making four full rotations in φ while varying θ from 0 to $\pi/2$ and from 0 to $\pi/5$, see App. C. Additional polar sweeps were performed for the FM-ZZ boundary with the higher discretization. To determine phase boundaries, the second derivatives of the ground-state energy along the sweeps were taken with respect to φ and θ .

As in the case of the phase diagrams in Sec. III A 1, the agreement between the LT and ED phase diagrams in Figs. 16(a) and 16(b) is spectacularly quantitative, especially in the $J_1 < 0$, $J_3 > 0$ sector relevant to α -RuCl₃, where the NCO analog of the IC1 phase appears in between the FM and ZZ phases, with their boundaries in close correspondence. We stress here again that the two side-by-side diagrams are not only obtained in two different limits, classical and quantum, and by the two methods with different limitations, but in the case of Fig. 16 they also span the entire parameter space of the model. Yet, the phases they contain and their compositions are in a remarkably close *quantitative* agreement.

The LT phase diagram in Fig. 16(a), being classical in nature, shows a complete symmetry between FM and AFM and ZZ and stripe phases, respectively. In the quantum $S = 1/2$ case in Fig. 16(b), this symmetry is lost, and there is no discernible intermediate phase between the AFM and stripe phases. As we discuss below, the symmetry of the LT phase diagram in Fig. 16(a) is only a property of the $J_1 - J_{z\pm} - J_3$ model, with the finite $J_{z\pm}$ also inducing asymmetries in the phase diagram, similarly to the quantum effects.

In the ED case, the ZZ-AFM boundary, which concerns the region of small J_1 , is somewhat problematic. This problem is due to the finite-size effects specific to the 24-site cluster, which splits into three independent clusters containing only 8 sites connected by the same J_3 network at $J_1 = 0$. Because of that, that sector of the phase diagram was clarified by DMRG.

3. Finite $J_{z\pm}$ phase diagram and other trends

Although not elaborated on in detail in the present study, the evolution of the phase diagram in Fig. 16 with Δ away from the $\Delta = 0$ limit is the following. For negative Δ , the IC1 and its mirror regions expand somewhat, while the rest of the boundaries shift only mildly. At about $\Delta = -0.4$, the z-AFM and z-FM regions open at

the outer edges of the ZZ and stripe sectors and continue to expand for $\Delta < -0.4$. This is in agreement with Figs. 14 and 15 where this range of Δ is associated with the smaller $|J|$. For positive Δ , the shift of most of the boundaries is less perceptible all the way to the Heisenberg limit $\Delta = 1$, with the only significant effect being a nearly complete disappearance of the intermediate IC1 phase away from the outer boundary for finite $J_{z\pm}$.

The evolution with $J_{z\pm}$ is more drastic and also more relevant to the discussed physical space of α -RuCl₃, featuring an asymmetry of the phase diagram mentioned above and the nucleation of another region of the IC2 phase from the FM-IC1 boundary at $J_{z\pm} > 0$. Upon the further increase of $J_{z\pm}$ to about 0.15, the two IC2 regions merge, while IC1 diminishes.

The effect of $J_{z\pm}$ is shown in Fig. 16(c) for $J_{z\pm} = 0.05$ in units of $J_1^2 + J_{z\pm}^2 + J_3^2 = 1$, which closely corresponds to its relative value for the representative Points 0, A, and B from the physical region for α -RuCl₃. With the full phase diagram for that choice of $J_{z\pm}$ shown in App. D, where one can observe the asymmetry of the previously symmetric phases, the cutout from it with the FM-ZZ region shown in Fig. 16(c) allows one to observe the emerging IC2 region within the IC1 phase. This is an important feature for the α -RuCl₃-related region of the phase diagram. The relatively small, but essential addition of $J_{z\pm}$ brings the polar phase diagrams in Fig. 16 to a close agreement with the Cartesian ones in Figs. 14 and 15, which show not one, but two intermediate IC phases.

Altogether, the consideration of the phase diagram of the KH model in the crystallographic frame (3) in Sec. III B highlights the benefits of the alternative perspective on the parameter space of the anisotropic-exchange models. The value of this perspective is also in the organic connection of the considered parameter space to the other models that are of wide interest in frustrated magnetism.

For instance, the circumference of the phase diagrams in Fig. 16 corresponds to the $J_1 - J_3$ FM-AFM model. The classical phase diagram of this model, known since the end of the 1970s [115], has been recently revisited for the quantum case because of the other Kitaev-candidate magnets [116–119]. It was found that the IC spiral state between FM and ZZ is completely replaced by the entirely unexpected phases, such as double-zigzag and z-AFM Néel phase [116], stabilized by quantum fluctuations. Not only does this consideration suggest a wider context to the studies of α -RuCl₃, but it also underscores the importance and the urgency of understanding of its proximate incommensurate phases, provided next.

IV. NATURE OF INCOMMENSURATE PHASES

As was made abundantly clear in the preceding pages, the only phases that occur in the vicinity of the ZZ region of the advocated α -RuCl₃ parameter space are the FM and incommensurate IC1 and IC2 phases. Although the FM state has been noted as relevant in the

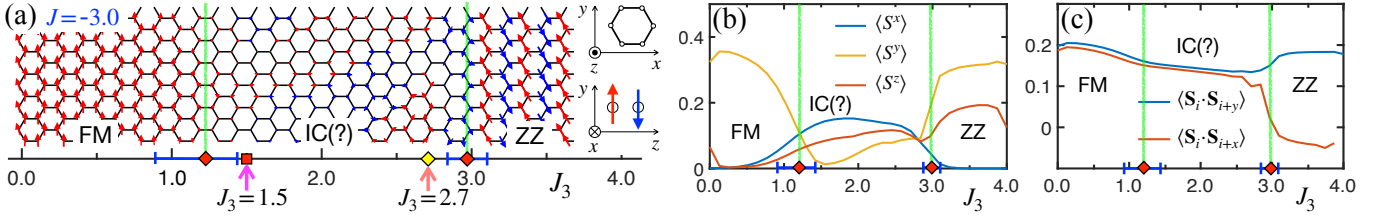


FIG. 17. (a) The 32×12 XC long-cylinder scan with J_3 from 0 to 4.0 meV for the Point 0 set and $J = -3.0$ meV. The blue and red arrows are the ordered moments' projections onto the yz plane with $\langle S_i^y \rangle < 0$ and $\langle S_i^y \rangle > 0$, respectively. IC(?) marks the phase that is not identified by the scan. The square and diamond with the arrows at $J_3 = 1.5$ meV and $J_3 = 2.7$ meV correspond to the same symbols in the phase diagram in Fig. 14(b) along the red line. The two non-scans at these values of J_3 are studied below, see Figs. 18 and 19. (b) and (c) $\langle S_i^\alpha \rangle$ components and nearest-neighbor correlators $\langle \mathbf{S}_i \cdot \mathbf{S}_{i+x(y)} \rangle$, respectively, averaged over the circumference of the cylinder, vs J_3 . Transitions between phases and error bars are indicated, see text.

past [65, 75, 83], the IC phases have not been closely scrutinized. Given the close proximity to where α -RuCl₃ may reside, exploring their nature is imperative.

This exploration is done using DMRG calculations presented below. Technically, we have employed a combination of two approaches, referred to as the DMRG “scans” and “non-scans,” using the ITensor library [129]. Both approaches utilized the $L_x \times L_y$ -site honeycomb-lattice open cylinders of width $L_y = 12$ (6 honeycomb cells). For the “scans,” we have used longer cylinders of $L_x = 32$ and had the J_3 parameter varied along their length for the representative 1D cuts that are shown in the phase diagrams in Figs. 14(b) and 15(b) by red arrows. The “non-scans” were done for the select parameter choices, with all parameters fixed, marked by diamonds and squares on the same 1D cuts in these figures. For the non-scans, we used more symmetric 12×12 cylinders with the aspect ratio that has been demonstrated to closely approximate the 2D thermodynamic limit [130]. The non-scans were performed on the so-called X-cylinders (XC) [131], in which one of the nearest-neighbor bond is horizontal, and on the Y-cylinders (YC), with these bonds being vertical, to study different orientations of orders. All scans were performed on the XC clusters.

This combination of approaches has been successfully employed in the past for the studies of the multi-dimensional phase diagrams of a variety of models and lattices [116, 131–136]. Scans give direct snapshots of the phases along their 1D cuts [131, 132], help to identify phase boundaries [133–135], distinguish first- and second-order transitions [136], and uncover hidden phases [116]. The non-scans allow one to study the given parameter set in finer detail.

We performed a sufficient number of DMRG sweeps to reach a maximum bond dimension of $m \sim 1600$ and to ensure good convergence with a truncation error of $\mathcal{O}(10^{-5})$. Generally, there is no spin-rotational symmetry to utilize in an anisotropic-exchange model (1), with the DMRG ground states typically breaking any remaining lattice or emergent spin symmetries. We find the local magnetic order in these states changes little with increasing bond dimension, a signature of mimicking the thermodynamic limit in 2D [137], enabling us to measure the local ordered moment $\langle \mathbf{S}_i \rangle$ directly.

With the nature of the incommensurate phases uncovered in Sec. IV A, the selfconsistency of our anisotropic strategy is also verified using DMRG in Sec. IV B.

A. IC1 and IC2: Deformed counter-rotating helices

Our main representative results are shown in Figs. 17, 18, and 19. In Fig. 17(a), we show the long-cylinder scan for the Point 0 set of $\{K, \Gamma, \Gamma'\}$ with J_3 varying from 0 to 4.0 meV for fixed $J = -3.0$ meV, the path corresponding to the solid red line in the Cartesian phase diagram in Fig. 14(b). The arrows represent the local ordered moments $\langle \mathbf{S}_i \rangle$ projected onto the yz plane. The honeycomb lattice is in the xy plane. Spins with positive and negative $\langle S_i^y \rangle$ are shown in red and blue, respectively.

This 1D cut through the phase diagram as a function of J_3 provides a direct visualization of the FM phase, an intermediate phase marked as IC(?) although it is not identified within the scan, and the ZZ phase. Fig. 17(b) shows the evolution of the three components of the on-site ordered moment, $\langle S_i^\alpha \rangle$, averaged over the vertical direction (circumference of the cylinder), vs J_3 . Fig. 17(c) shows the same for the nearest-neighbor correlators $\langle \mathbf{S}_i \cdot \mathbf{S}_{i+x} \rangle$ and $\langle \mathbf{S}_i \cdot \mathbf{S}_{i+y} \rangle$ averaged the same way.

The transition points and their error bars are determined from the inflection points in the ordered moment curves and the widths of the transition regions, respectively. One can see that the transition region is narrower and sharper on the IC-ZZ side, consistent with both ED and LT approaches indicating the first-order character of that transition. This transition point at $J_3 \approx 3$ meV is also in a very close agreement with the ED results of Fig. 14(b) discussed in Sec. III A 1. The FM-IC transition is “softer” by all indicators shown in Fig. 17, again in agreement with both ED and LT that suggested a nearly second-order type of it. The DMRG scan also shows the FM-IC transition at $J_3 \approx 1.2$ meV, a somewhat lower value than the one found by ED in Fig. 14(b).

From the ordered moment curves in Fig. 17(b), one may also find an indication of a transition within the IC region at about $J_3 \approx 2.0$ meV, suggesting two different IC phases in the scan, with this suggestion certainly requiring a less speedy look. Such a look is provided below in Figs. 18 and 19 by the two non-scans within the IC

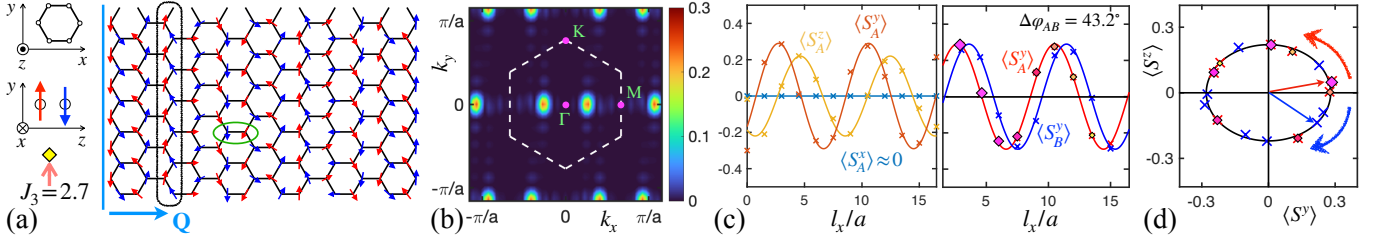


FIG. 18. (a) The 12×12 XC-cylinder non-scan for the Point 0, $J = -3.0$ meV, and $J_3 = 2.7$ meV. Ordered moments are colored according to the A (red) and B (blue) sublattices. The unit cell (small ellipse), propagation vector \mathbf{Q} of the counter-rotating spirals, and the vertical zigzag column (rounded rectangle) normal to \mathbf{Q} are indicated. (b) $|\langle S_{B,\mathbf{q}}^y \rangle|^2$ shows the periodic single- \mathbf{Q} character of the state in (a). First panel in (c): $\langle S_A^{x(y,z)} \rangle$ spin components in the A sublattice along the cylinder. Spins rotate in the yz plane, normal to $\mathbf{Q} \parallel x$. Second panel in (c): $\langle S_A^y \rangle$ and $\langle S_B^y \rangle$ vs x . There is a phase offset $\Delta\varphi_{AB}$ between the A and B spirals. Symbols are the data, solid lines are the spiral ansatz for the deformed counter-rotating spin helices in Eq. (14). Colored diamonds of decreasing size mark the data for sublattice A vs x to correlate with (d). (d) Cross-sections of the A and B helices, viewed along the x -axis. Straight arrows are ordered moments from the rounded black rectangle in (a) averaged over the vertical columns. The curved arrows are the directions of the spins' rotation along \mathbf{Q} . Following the diamonds as they decrease in size from that initial column, one can see the counterclockwise rotation about the spiral for the A sublattice.

phases at $J_3 = 2.7$ meV and $J_3 = 1.5$ meV, respectively. They are marked by the square and the diamond (with arrows) in Fig. 17(a), corresponding to the symbols used for these points in the phase diagram in Fig. 14(b).

1. IC1

Starting from $J_3 = 2.7$ meV, which is closer to the ZZ phase, Fig. 18(a) shows the 12×12 XC cylinder with all parameters fixed as discussed. To facilitate the visual perception of its real-space spin configuration, the local ordered moments are colored in red and blue according to their sublattices of the honeycomb lattice, A and B, respectively, with the unit cell marked by the green oval. Spins are shown in the yz plane and the honeycomb lattice is in the xy plane, as before.

Focusing on the spins in the vertical zigzag columns in Fig. 18(a), such as the one marked by the rounded rectangle, and following their evolution along the cylinder length, it is apparent that spins in the two sublattices form counter-rotating spirals, with red spins rotating clockwise and blue spins counterclockwise.

Fig. 18(b) complements these real-space observations. It shows a proxy of the static structure factor, $|\langle S_{B,\mathbf{q}}^y \rangle|^2 = |\sum_{i \in B} S_i^y e^{i\mathbf{q}\mathbf{r}_i}|^2$, the square of the norm of the Fourier transform of one of the spin components from one sublattice, highlighting its periodicity. The peaks correspond to the propagation vector $\pm\mathbf{Q}$ of the spiral, with the dashed hexagon showing the Brillouin zone of the honeycomb lattice. Since the \mathbf{Q} vector is directed along the Γ -M line, parallel to the horizontal nearest-neighbor bonds, the spin state realized in the DMRG cluster in Fig. 18(a) identifies closely with the IC1 state of the LT approach in Fig. 14(a), discussed in Sec. III A 1.

Figs. 18(c) and 18(d) quantify this IC1 state of the two-sublattice counter-rotating spirals in more detail. To be precise, these spirals will be referred to as the deformed spin helices. The first panel of Fig. 18(c) explicates that the helices rotate entirely in the yz plane, that is, in a screw-like fashion, normal to the propagation vector

$\mathbf{Q} \parallel x$ of the helix. For clarity, only the results for the A-sublattice (red spins) are shown, with the ones for the B-sublattice being very similar.

The second panel of Fig. 18(c) demonstrates the phase offset between the A and B helices. Fig. 18(d) provides the parametric plot of the $\langle S_i^z \rangle$ vs $\langle S_i^y \rangle$ in both sublattices, which is also the cross-sectional view of the helices along the x -axis. The spins on the edges are excluded, straight arrows show the ordered moments from the rounded black rectangle in Fig. 18(a), and curved arrows show the direction of the rotation of the helices along the propagation vector \mathbf{Q} .

In Figs. 18(c) and 18(d), the symbols are the DMRG data for the ordered moments averaged over the vertical zigzag columns and plotted vs the x -coordinate of the cylinder in units of the interatomic distance a . The solid curves are given by the spiral ansatz with $\mathbf{Q} \parallel \hat{x}$

$$\langle \mathbf{S} \rangle_{i,\gamma} = \hat{\mathbf{y}} \langle S^y \rangle \cos \theta_{i,\gamma} \pm \hat{\mathbf{z}} \langle S^z \rangle \sin \theta_{i,\gamma}, \quad (14)$$

where $\hat{\mathbf{y}}$ and $\hat{\mathbf{z}}$ are the unit vectors for the y and z axes, \pm is for $\gamma = A(B)$, and the phases are $\theta_{i,\gamma} = \mathbf{Q}\mathbf{r}_i + \varphi_\gamma$.

The in-plane and the out-of-plane ordered moments in Figs. 18(c) and 18(d) are $\langle S^y \rangle = 0.28$ and $\langle S^z \rangle = 0.22$, and the phase offset between the A and B helices is $\Delta\varphi_{AB} = 43.2^\circ$. One can read the pitch of the helix from Fig. 18(c) as $\ell \approx 7.85a$, which corresponds to the incommensurate $|\mathbf{Q}| \approx 0.19$ r.l.u. [reciprocal lattice vector is $\mathbf{G} = (4\pi/3a, 0)$].

Before moving on to the next non-scan, we note, for the record, that the DMRG non-scan in the XC cylinder in Fig. 18(a) realizes an incommensurate spiral state.

2. IC2

For $J_3 = 1.5$ meV, the point in the proximity of the FM-IC phase boundary, see Fig. 17(a), a different state is realized, for which we found the “rotated” YC orientation of the cylinders to be optimal. In Fig. 19(a), the 6×24 YC cylinder is shown, with the same color-coding for the

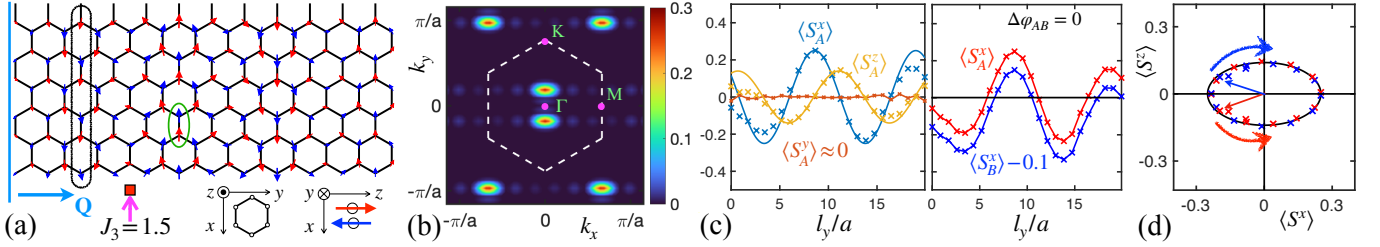


FIG. 19. Same as Fig. 18 for the 6×24 YC-cylinder at $J_3 = 1.5$ meV and $S^y \Rightarrow S^x$. In the second panel of (c), the B-sublattice data are shifted to emphasize zero phase offset.

spins according to their sublattices as in Fig. 18(a), but spin are now shown in the zx plane, while the lattice axes are maintained as xy for consistency.

With the evidence presented in Figs. 19(a), 19(b), 19(c) and 19(d), following the same exposition as in Fig. 18, it is easy to see that the state presented here identifies with the IC2 state of the LT approach in Fig. 14(a), also discussed in Sec. III A 1. It is also composed of the two deformed counter-rotating helices in the two sublattices, with the spin plane normal to the propagation vector of the helices, but now with the \mathbf{Q} vector directed perpendicular to the nearest-neighbor bonds of the honeycomb lattice, $\mathbf{Q} \parallel \hat{\mathbf{y}}$, which is parallel to Γ K line

$$\langle \mathbf{S} \rangle_{i,\gamma} = \hat{\mathbf{x}} \langle S^x \rangle \cos \theta_{i,\gamma} \pm \hat{\mathbf{z}} \langle S^z \rangle \sin \theta_{i,\gamma}, \quad (15)$$

Apart from the different direction of the ordering vector in the IC2 phase compared to that of the IC1, the qualitative difference is also in the lack of the phase offset between the A and B helices, meaning that in the spiral ansatz in Eq. (15), $\Delta\varphi_{AB}$ is zero, as is demonstrated in the second panel of Fig. 19(c).

Quantitatively, the in-plane and the out-of-plane ordered moments in the spiral ansatz (15) for the solid lines in Fig. 19(d) are $\langle S^x \rangle = 0.25$ and $\langle S^z \rangle = 0.14$, exhibiting a stronger deformation of the helices than in the IC1 state of Fig. 18(d). The pitch of the helix in Fig. 19(c) is also longer, $\ell \approx 10.39a$, corresponding to $|\mathbf{Q}| \approx 0.144$ r.l.u., translating to the the nearly commensurate periodicity of six hexagons along the YC cylinder, as one can observe in Fig. 19(a).

3. Comparison with LT and classical spiral ansatz

The IC phases were found as potentially proximate to the α -RuCl₃ parameter space using the LT approach and verified with ED and DMRG.

In order to show the almost unnatural closeness of the agreement of the LT and DMRG results, we performed additional checks of the IC states within the LT approach for the representative choices of parameters for the Point 0 selection of the anisotropic terms and two choices of the $\{J, J_3\}$ pair: $J = -3.5$ meV and $J_3 = 2.4$ meV for the IC1 phase and $J = -2.0$ meV and $J_3 = 1.8$ meV for the IC2 phase, shown by the diamond and the square, respectively, in the Cartesian LT phase diagram in Fig. 14(a).

The IC1 representative choice in the LT calculations yielded the phase offset between the A and B helices as $\Delta\varphi_{AB} = 41^\circ$ and the pitch of the helix as $\ell \approx 7.805a$, both nearly coincidental with the corresponding numbers in the DMRG results in Sec. IV A 1 above. For the IC2 choice, the LT gives zero phase offset $\Delta\varphi_{AB}$, in a complete accord with the same DMRG answer in Sec. IV A 2. The pitch of the helix is somewhat shorter than the DMRG counterpart, $\ell \approx 8.03a$, but not by much.

The purely classical spiral solution suggests no dependence of the spiral's pitch on the isotropic exchanges for the fixed anisotropic ones, see App. E. This is in a broad agreement with all non-scans for the IC states that we have studied by DMRG, all showing similar values of their $|\mathbf{Q}|$. The LT results are less constraining, but the windows for \mathbf{Q} for both IC1 and IC2 are narrow.

Here is the summary of the rather amazing agreement of the LT and DMRG results on the IC phases.

- Two distinct states are realized in both approaches, IC1 and IC2, with the ordering vectors \mathbf{Q} directed along ΓM and ΓK of the honeycomb-lattice BZ, respectively, parallel and perpendicular to the nearest-neighbor bonds, with IC1 bordering the ZZ phase and IC2 the FM phase.
- Despite the different orientation of the ordering vectors, there is no sign of a significantly sharp transition between these two ICs in either of the methods, suggesting a weak first-order transition in the thermodynamic limit. They are nearly degenerate in LT and classical calculations and DMRG scans shows only minor signs of a transition. For some of the parameters, DMRG non-scans in XC vs YC cylinders showed different \mathbf{Q} orientations and dependence on the initial state also hinted at a close degeneracy of the different IC states.
- All approaches show a remarkable consistency regarding the first-order like transition at the ZZ-IC1 boundary and the second-order or weakly first-order transition for the FM-IC2 boundary.
- Both LT and DMRG identify IC states as the screw-like spirals, or helices, with the plane of spin rotation orthogonal to the propagation vector \mathbf{Q} (nearly orthogonal for IC2 in the LT case).
- Both LT and DMRG identify IC states as the counter-rotating helices of spins in the two sublattices of the honeycomb structure.

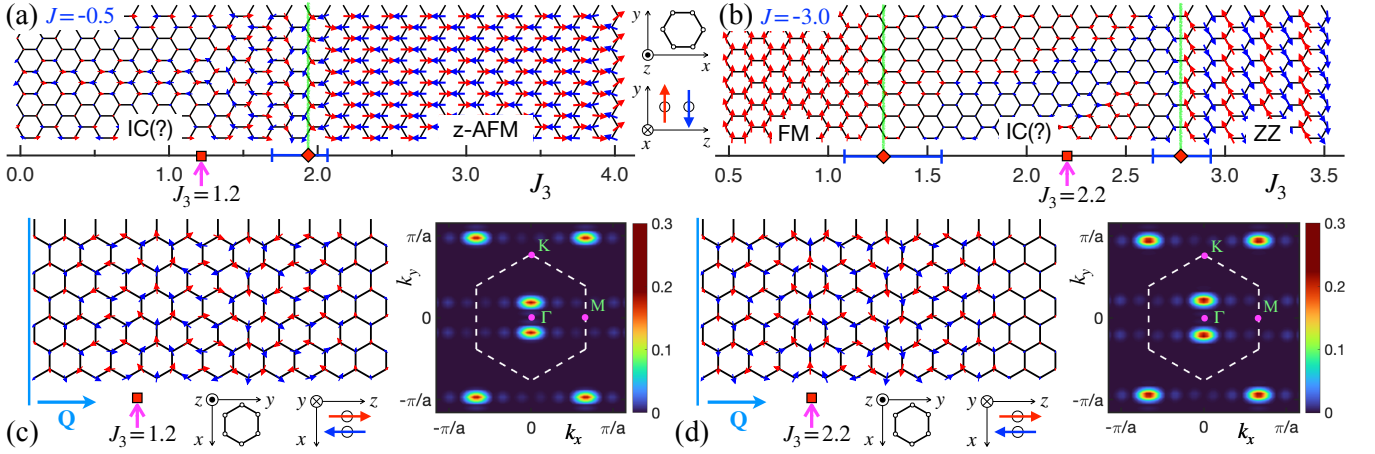


FIG. 20. (a) and (b) The 32×12 XC long-cylinder scans for Point A and $J = -0.5$ meV and $J = -3.0$ meV, respectively, same as in Fig. 17(a), J_3 's for the non-scans in (c) and (d) are indicated. (c) and (d) The 6×24 YC-cylinder non-scans and $|\langle S_{B,\mathbf{q}}^x \rangle|^2$ for $J_3 = 1.2$ meV and $J_3 = 2.2$ meV, respectively, same as in Figs. 19(a) and 19(b).

- The phase offset between the IC2 helices is zero in both LT and DMRG, and it is finite for IC1, with values that are close between the two techniques.
- The pitch of the helices is independent of J and J_3 , i.e., fully defined by the $\{K, \Gamma, \Gamma'\}$ choice in the classical calculations of App. E, which is in a broad agreement with all non-scans probed by DMRG.

This rather astonishing accord between the classical LT and purely quantum DMRG techniques reinforces the sentiment expressed earlier in Sec. III A 1 on the ability of the LT method to mimic quantum effects of the fluctuating states that are not conserving the length of the ordered moments [128], as it allows one to “squish” the helices in the IC phases, thus lowering the energy and letting LT to guess the states correctly.

We would be remiss if we did not mention the earlier discovery and detailed analysis of the counter-rotating spirals in the lithium-iridate compounds, described by a similar model on related honeycomb-based structures and rationalized as a sign of their significant bond-dependent Kitaev-like exchanges, see Refs. [138–142].

4. Point A, more phases, more helices

Here we provide some additional DMRG analysis of the phase diagram for the Point A anisotropic parameter set in order to reinforce the earlier findings, expose additional phases, and verify the ubiquity of the IC states.

Our Figures 20(a) and 20(b) provide the 1D scans through the phase diagram for the Point A in Fig. 15(b) along the two vertical red lines, at $J = -0.5$ meV and $J = -3.0$ meV, respectively, vs J_3 . Notations, color-coding, and analysis are the same as for Fig. 17(a) above.

One can see that in both cases, the agreement for the upper transition boundary with the ED results in Fig. 15(b) is very close, while the lower boundary with the FM phase is shifted down significantly compared to ED, the trend already noted in Sec. IV A above. This is also in agreement with the “softer” character of that

transition. In Fig. 20(a) the FM phase is simply absent, and the upper boundary is with the z-AFM Néel phase that has spins pointing along the z axis, promoted by the antiferromagnetic out-of-plane nearest-neighbor exchange in the crystallographic parametrization of the model (3) and the J_3 term, as discussed in Sec. III A 1.

In Figs. 20(c) and 20(d), the IC states, corresponding to the choices of $\{J, J_3\} = \{-0.5, 1.2\}$ meV and $\{J, J_3\} = \{-3.0, 2.2\}$ meV, respectively, and marked by the arrows in Figs. 20(a) and 20(b), are exposed in the same fashion as in Figs. 18(a), 18(b) and 19(a), 19(b) above.

In Figs. 20(c) and 20(d), we use the 24×6 YC cylinders, with the spins shown in the zx plane and the square of the norm of the Fourier transform of $|\langle S_{B,\mathbf{q}}^x \rangle|^2$ shown in the second panels. By following the same analysis as in Figs. 18(c) and 19(c), both states are identified as the representatives of the IC2 phase. As for the IC2 state in Fig. 19, they are described by the two-sublattice, deformed counter-rotating helices with the spin plane normal to the propagation vector of the helices and with the \mathbf{Q} vector directed along the ΓK line.

One notable feature of all DMRG non-scans of the IC states analyzed in our study is the close lengths of their \mathbf{Q} vectors, suggesting the pitches of their helices to be roughly independent of the isotropic exchanges J and J_3 , in agreement with the classical consideration of App. E.

5. IC summary

The puzzling incommensurate phases in the phase diagram of $\alpha\text{-RuCl}_3$ are enigmas no more.

The IC1 and IC2 phases were identified in Sec. III as proximate to the parameter space relevant to $\alpha\text{-RuCl}_3$, see Figs. 14, 15, and 16. They were discussed as vitally important to the understanding of their possible effects onto the $\alpha\text{-RuCl}_3$ properties. They are now fully exposed and understood as constituting two types of the counter-rotated helices with different directions of their propagation vectors as is thoroughly demonstrated above.

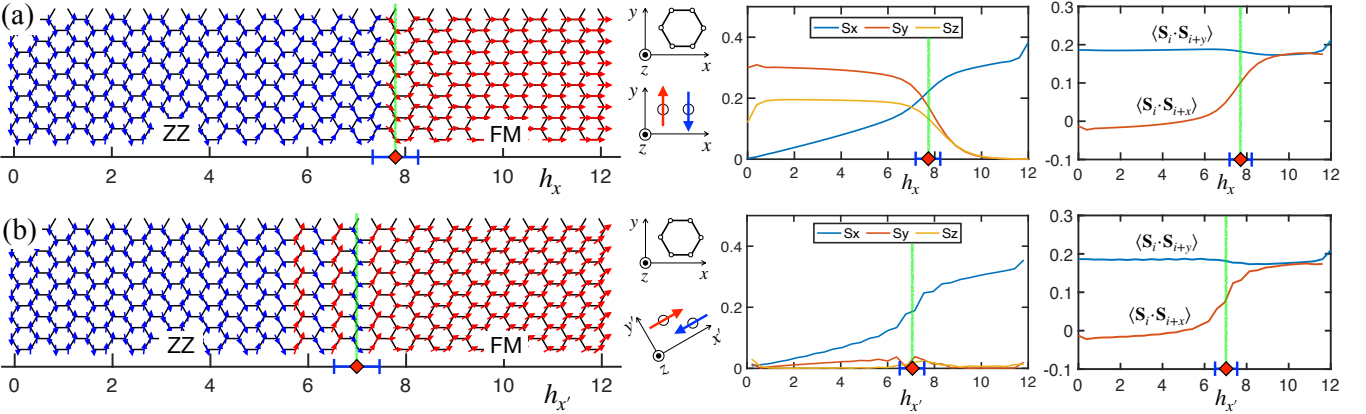


FIG. 21. The 32×12 XC long-cylinder scans for the Point \star parameter set (12) vs field (a) parallel to the bond, $b(x)$ -direction, and (b) perpendicular to the bond, $a(x')$ -direction. The arrows are the ordered moments' projections onto the xy plane. Arrows within 45° to the field are colored in red and otherwise in blue. The second and third panels show $\langle S_i^\alpha \rangle$ and $\langle \mathbf{S}_i \cdot \mathbf{S}_{i+x(y)} \rangle$, respectively, averaged over the vertical columns, same as in Fig. 17. In (b) axes for spins are rotated to align x' axis with the field, see text. Transitions to the polarized phase are indicated.

The IC1 phase, bordering the immediate region of the ZZ phase pertinent to α -RuCl₃, is separated from it by a first-order transition, suggesting limited direct effects of the IC phases on the phenomenology of this material.

If anything, this consideration also dispels the unfounded, but persistent misconception that the standard DMRG approach is incapable of identifying spiral phases, especially incommensurate ones, and would always select a different ground-state instead. Figures 17, 18, 19, and 20 and the detailed analysis provided above shatter that belief.

B. DMRG and ED verifications

We now look all the way back at the initial assumptions of the present study. Our strategy of restricting anisotropic terms of the model for α -RuCl₃ by using select physical observables that occur only because of such terms hinges on our ability to calculate these observables, which, in turn, assumes they have small or controlled quantum effects, see Secs. IC1 and II A.

For one of them, the ESR gap in Sec. II A 2, this logic is justified as it is deeply rooted in the more general approach of the field-induced quenching of quantum fluctuations. However, for the other two observables that we have chosen as the physical constraints, an *a posteriori* proof of the validity of such assumptions is needed.

For the out-of-plane tilt angle α , see Sec. II A 1, we had some prior circumstantial evidence that the effects of quantum fluctuations in α are small [64]. For the observed small difference of the in-plane critical fields ΔH_c , Sec. II A 3, the argument was that although the critical fields themselves should renormalize strongly, they should do it in sync. This requires such a difference to be small already at the “bare” quasiclassical level, before accounting for quantum effects. We posed this as a falsifiable prediction of our strategy, see Sec. II A 3.

1. Selfconsistency checks

Here we present a complete validation of both assumptions, and more.

As one can observe already in the DMRG scans in Figs. 17 and 20(b), the tilt angle of the spins in the ZZ phase shown in the yz -plane is significant and is consistent with the “bare” 30° -to- 37° physical range proposed in Sec. II A 1. It is also independent or only weakly dependent on the isotropic exchanges J and J_3 , in accord with the classical energy minimization result in Eq. (4).

A more precise evaluations from the numerical values of the spin projections for Point 0 and Point A sets of parameters give the renormalized angles 33.7° and 29.4° against their bare values of 35° and 32° , respectively, see Sec. II B 1. Thus, the renormalization effect on α is small, leaving it safely within the physical range and fully justifying the use of its bare expression in Eq. (4) for restricting model parameters.

The most challenging assumption is the use of ΔH_c as a phenomenological constraint. To verify this, we chose the representative set of the Point \star , see Sec. III A 2 and Eq. (12), which is Point 0 of the anisotropic set of $\{K, \Gamma, \Gamma'\}$ with the isotropic pair $\{J, J_3\}$ fixed in the plausible region for α -RuCl₃, as is described in Sec. III A 2. One can use Eqs. (8) and (9) for the Point \star set to obtain the bare values of $H_{c,0}^{(b)} = 12.51$ T and $H_{c,0}^{(a)} = 11.71$ T, with their bare difference $\Delta H_{c,0} = 0.8$ T corresponding to how the selection of the Point 0 set was made, see Sec. II B 1. Recall that the experimental values are $\Delta H_c^{\text{exp}} \approx 0.8$ T, $H_{c,\text{exp}}^{(b)} \approx 7.8$ T, and $H_{c,\text{exp}}^{(a)} \approx 7.0$ T.

We performed DMRG scans vs field in the two principal in-plane directions, a and b , perpendicular and parallel to the bond, respectively, for the Point \star parameter set. The results are presented in Fig. 21, with the presentation mirroring that of Fig. 17, with the key difference being the spin-projection plane now being xy in order to emphasize the polarizing effect of the field.

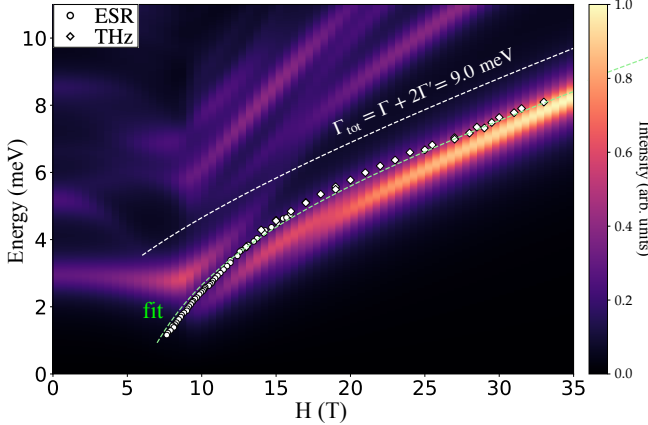


FIG. 22. The intensity map of $\mathcal{S}^{bb}(0, \omega)$ versus field in the a -direction obtained using a 24-site cluster ED for the Point \star set, experimental ESR [29] and THz [80] data for the lowest-energy spin excitation energy from Fig. 5, and LSWT results from Eq. (6) for $\Gamma_{\text{tot}} = 9.0$ meV for the Point \star set.

In Fig. 21(b), to compare the results for the two field directions fairly, we kept the same XC cylinder for $H^{(a)}$, but used a tilted direction of the field to have it perpendicular to the bond, with the spin axes tilted accordingly. Because of the tilt, the averaging of the spin components $\langle S_i^\alpha \rangle$ and correlators $\langle \mathbf{S}_i \cdot \mathbf{S}_{i+x} \rangle$ and $\langle \mathbf{S}_i \cdot \mathbf{S}_{i+y} \rangle$ was done over the two nearest vertical zigzag columns to minimize the oscillatory trends in these quantities.

The data in the second and third panels in Figs. 21(a) and 21(b) together with the scans themselves show clear transitions from the ZZ to polarized FM states, with their positions determined from the inflection points of the data, as before. The DMRG results do indeed confirm that the downward renormalization of the critical fields is quite significant in both directions, reaching some 60%–70% of their bare values, in agreement with the expectations laid out above.

Quite remarkably, the critical fields are renormalized down from their classical values by about the same factor, maintaining close proximity to each other and providing strong support to the suggested constraint. Their resultant values are also astonishingly close to the experimental ones, $H_c^{(b)} \approx 7.8(5)$ T and $H_c^{(a)} \approx 7.0(5)$ T, effectively maintaining the original value of the critical field difference of $\Delta H_c \approx 0.8(5)$ T.

While such a close agreement with the experimental data for the chosen representative set of parameters may be somewhat fortuitous, the demonstrated confirmation of the original logic of our approach is simply spectacular, providing a very strong support to the validity of our strategy, approach, and their results.

For completeness, we also provide a verification of the ESR gap criterion for the Point \star set using an ED calculation of the excitation spectrum on a 24-site cluster.

In Figure 22, the intensity map of the $\mathbf{q}=0$ dynamical spin-spin correlation function, $\mathcal{S}^{bb}(0, \omega)$, obtained by ED is shown versus the field in the a -direction. Also shown are the experimental data presented in Fig. 5 and the

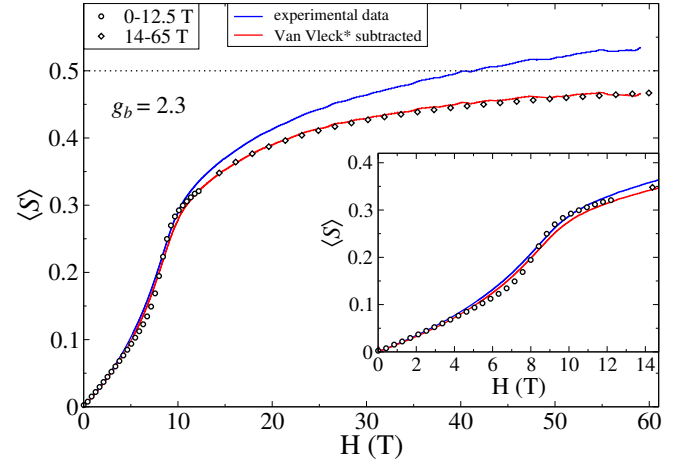


FIG. 23. Upper curve is the ordered moment extracted from the $M(H)$ results for $\alpha\text{-RuCl}_3$ in the in-plane field, Ref. [22], symbols are DMRG results, and the lower curve is the experimental data with the Van Vleck contribution subtracted, see text. Inset: same for the smaller range of fields.

“bare” LSWT magnon energy E_0 from Eq. (6) for $\Gamma_{\text{tot}} = \Gamma + 2\Gamma' = 9.0$ meV, which corresponds to the Point 0 (and Point \star) set. The g -factor in ED is the same as in Fig. 5.

The ED calculations were carried out using the Lanczos algorithm [143], employing the continued fraction method [144] to obtain the dynamical correlation functions. A Krylov dimension of 150 and a Lorentzian broadening of 0.5 meV were used; see also App. C 3.

The downward-renormalization effects of quantum fluctuations on the ESR gap, emphasized in Sec. II A 2 and Fig. 5 as necessary arguments for the large value of $\Gamma + 2\Gamma'$, are clear from the difference between its quasi-classical and ED values. Although not providing an ideal fit to the experimental data, the lowest-energy excitation in the ED spectrum provides a quantitative agreement that is much closer than that of the other parameter sets for which similar calculations have been performed [65, 80].

All three successful comparisons serve as a direct *a posteriori* validation of our strategy for constraining the anisotropic terms of the effective model.

2. Magnetization curve

As a corollary of this study, our Figure 23 shows a comparison of the DMRG and experimental results for the ordered moment along the field vs the in-plane field. DMRG is for the Point \star parameter set (12) and the low-temperature magnetization results are from Ref. [22], which provided $M(H)$ data for $\alpha\text{-RuCl}_3$ for the fields up to 60 T.

The DMRG results, shown by the symbols, are from the two 32×12 XC long-cylinder scans for the field along the b -direction. The first one is from 0 T to 12.5 T (circles), also shown in the second panel of Fig. 21(a), and the second scan is from 14 T to 65 T (diamonds). The upper curve is the original experimental data from Ref. [22].

As one can see, even at the highest field the ordered moment in DMRG is not fully saturated and retains some residual field dependence. Thus, to subtract the Van Vleck contribution from the experimental curve more consistently, we extract the linear slope in the high-field range of $\gtrsim 40$ T from *both* the experimental and DMRG data. Then the linear contribution with the *difference* of these slopes is subtracted from the upper curve to obtain the lower one for all H . In this study, we also used a slightly smaller $g_b = 2.3$ to match the value quoted in Ref. [22].

Needless to say, the agreement demonstrated in Fig. 23 is rather close. The DMRG results also naturally reproduce the low value of the saturated moment in the nominally polarized phase just above $H_c^{(b)}$, the slow approach of M to the saturation, and its unusual behavior showing an inflection point in the lower fields, see inset. This is not to claim that the Point \star parameter choice in Eq. (12) is unique in describing $\alpha\text{-RuCl}_3$, but it certainly makes the case that the region from where this representative set was extracted has a lot to do with this materials' phenomenology.

V. OUTLOOK

With the progress in finding a definitive set of parameters for an effective model of $\alpha\text{-RuCl}_3$ described above, is this truly the end of the $\alpha\text{-RuCl}_3$ parameters' drama? Yes and no.

It is an unequivocal “yes” in the sense of much better clarity on the overall strategy for finding such parameters, on where the parameters of the effective model lie, and what phases are proximate to that region.

It is a more cautious “no,” or “maybe,” for the following reasons.

First, there is a technical issue of evaluating a wide range of physical observables for $\alpha\text{-RuCl}_3$ using parameters from the physical regions proposed in this work. Preferably, such calculations should be performed using unbiased numerical methods, with the goal of possibly identifying a more precise set of these parameters. A more complex reason is that the description of some experiments may require further “dressing” of the $\alpha\text{-RuCl}_3$ effective model with additional exchanges.

There are subleading, but potentially important, 3D couplings between the honeycomb planes of $\alpha\text{-RuCl}_3$, with estimates in the range of 0.5 meV compared to 5–10 meV for the parameters of the 2D plane model considered in this work [47]. However, they cannot be simply added on top of the 2D parameters discussed here, as the parameters for that modified 3D model need to be re-evaluated to meet the same phenomenological constraints. This may or may not be a trivial rescaling of some subset of existing 2D terms, as discussed above, depending on how isotropic these 3D couplings are [86].

There is also a possibility of lower symmetry within the $\alpha\text{-RuCl}_3$ honeycomb planes, reducing it to C_2 and making exchanges on two nearest-neighbor bonds dif-

fer from those on the third [14]. Certainly, this would modify and complicate the implementation of our proposed constraints. Whether such a change can or cannot be accounted for without modifying the effective five-parameter model discussed in this work has not been investigated. The answer may also depend on which specific experiments are to be described.

A major direction that is not pursued in this work and left for future studies is the quantitative description of inelastic neutron scattering (INS) results for $\alpha\text{-RuCl}_3$ using parameters from the physical ranges proposed here. INS measurements have clearly indicated non-negligible 3D couplings in $\alpha\text{-RuCl}_3$ [47], so the model needs to be modified accordingly before pursuing such a study.

Another specific issue with such studies is the use of the linear spin-wave theory (LSWT) for anisotropic-exchange models in general and for the suggested ranges of the effective $\alpha\text{-RuCl}_3$ model in particular, both in the zigzag state and in the nominally polarized paramagnetic one. The problem is strong quantum effects in the spectrum. For instance, one can verify for any parameter sets proposed in this work, or from their broad vicinity, that the predicted zero-field LSWT single-magnon spectrum will have an unreasonably large width and a vanishingly small gap for the lowest excitation at the accidental M-points, not affiliated with the ordering vector.

For the problem of large width, one can technically mitigate this effect by considering strong mixing with two-magnon continua. This should also eliminate much of the coherent spectrum at higher energies [46, 48, 75], bringing the results for that part of the spectrum into broad accord with experimental observations. For the vanishing gap, the observed lowest-energy experimental mode is at the same \mathbf{q} -vector, but the gap is not zero. The technical solution to the problem requires a rather involved calculation that includes fluctuation-induced corrections selfconsistently [145], making any naïve comparison of the LSWT spectra with the experimental ones in the fluctuating regime somewhat meaningless.

Another approach is to model the INS spectrum using numerical methods. In App. C 3, we present results for one such calculation of the dynamic spin correlation function that can be used as a proxy for the INS dynamical structure factor. The calculations are for zero field and for the parameter set suggested in this work. While a more detailed analysis is needed to compare these results with the available INS data, certain improvements relative to similar comparisons can be pointed out, such as a better quantitative matching of the lowest-energy excitations, in accord with experimental expectations.

One may also envision a re-investigation of the theoretical calculations of field-induced thermal transport phenomena in $\alpha\text{-RuCl}_3$ using the parameter sets proposed in this work [55, 77]. However, given the emergent consensus on the substantial contribution of phonons to such effects, this research direction is more tenuous.

Thus, the saga of $\alpha\text{-RuCl}_3$ continues.

VI. CONCLUSIONS

In this paper, we have offered a historical overview of the searches for the best effective model of α -RuCl₃, which are complicated by the material's strongly fluctuating ground and field-induced states and the complex structure of its low-energy description. We have outlined an “anisotropic strategy” for constraining the most important spin-orbit-induced anisotropic-exchange model parameters using existing phenomenology and demonstrated its success for α -RuCl₃ using a combination of quasiclassical analysis and unbiased numerical approaches. The same strategy can be applied to other anisotropic-exchange materials with complex models.

The resulting constrained parameter space allowed us to focus on a much narrower region of the multi-dimensional phase diagram of the α -RuCl₃ model. The selected representative choices of anisotropic exchanges enabled a detailed study of the remaining dimensions of its parameter space.

Not only has this approach systematically led us to the definitive parameter region of α -RuCl₃ in the phase diagram, but it has also facilitated an otherwise prohibitively costly numerical exploration of its parameter space. This exploration, with both semi-classical and quantum methods, has demonstrated remarkable agreement on the structure, properties, and hierarchy of the phases, demystifying relevant proximate phases of α -RuCl₃. Specifically, the enigmatic nature of the incommensurate phases has been resolved in the present study, identifying them as counter-rotating helical states.

Moreover, a verification of our proposed general anisotropic strategy and our specific choices of phenomenological constraints has been performed using DMRG and ED, confirming the selfconsistency of our assumptions and results, showing a notable accord between experiments and theory, and further justifying the validity of our strategy and proposed parameters.

In addition to a systematic analysis of prior attempts at determining α -RuCl₃ parameters and bringing closer together several approaches to the derivation of anisotropic-exchange models, our work has suggested an intuitive description of its model via a different crystallographic parametrization of the exchange matrix, offering a unifying view of the earlier assessments of its parameters and yielding important physical insights. This parametrization has also provided a connection to a broader class of relevant paradigmatic models in frustrated magnetism, thus expanding the context of studies of α -RuCl₃.

ACKNOWLEDGMENTS

We would like to thank Matthias Vojta and Cristian Batista for fruitful discussions and Radu Coldea and Steven Nagler for sharing their experimental results. We are indebted to David Kaib for numerous insights and educational efforts. We are grateful to Giniyat Khaliullin for sharing the data and inspirational conversations.

A. L. C. thanks A. A. Chernyshev for precious editorial inputs and appreciation of cultural references.

The work by S. J. and S. R. W. was supported by the National Science Foundation under DMR-2412638. S. J. is also supported by the Department of Energy (DOE), Office of Sciences, Basic Energy Sciences, Materials Sciences and Engineering Division, under Contract No. DEAC02-76SF00515. M. M. and R. V. gratefully acknowledge support by the Deutsche Forschungsgemeinschaft (DFG, German Research Foundation) for funding through TRR 288-422213477 (project A05) and CRC 1487-443703006 (project A01). The work of A. L. C. was supported by the U.S. Department of Energy, Office of Science, Basic Energy Sciences under Award No. DE-SC0021221.

We would like to thank Aspen Center for Physics (A. L. C.) and the Kavli Institute for Theoretical Physics (KITP, A. L. C. and R. V.) where different stages of this work were advanced. The Aspen Center for Physics is supported by National Science Foundation Grant No. PHY-2210452 and KITP is supported by the National Science Foundation under Grant No. NSF PHY-2309135.

Appendix A: Details

The transformation matrix $\hat{\mathbf{R}}_c$ from the cubic to crystallographic reference frame in Fig. 1(b) is

$$\hat{\mathbf{R}}_c = \begin{pmatrix} -\frac{1}{\sqrt{2}} & \frac{1}{\sqrt{2}} & 0 \\ -\frac{1}{\sqrt{6}} & -\frac{1}{\sqrt{6}} & \sqrt{\frac{2}{3}} \\ \frac{1}{\sqrt{3}} & \frac{1}{\sqrt{3}} & \frac{1}{\sqrt{3}} \end{pmatrix}, \quad (A1)$$

The form of the Hamiltonian (1) in the crystallographic $\{x, y, z\}$ axes of the honeycomb plane is given by Eq. (3). Its parameters are related to that of the generalized KH model in the cubic axes (1) via

$$\begin{aligned} J_1 &= J + \frac{1}{3}(K - \Gamma - 2\Gamma'), \\ (1 - \Delta)J_1 &= -(\Gamma + 2\Gamma'), \\ J_{\pm\pm} &= -\frac{1}{6}(K + 2\Gamma - 2\Gamma'), \\ J_{z\pm} &= \frac{\sqrt{2}}{3}(K - \Gamma + \Gamma'). \end{aligned} \quad (A2)$$

The inverse relation is

$$\begin{aligned} J &= \frac{1}{3}(2J_1 + \Delta J_1 + 2J_{\pm\pm} - \sqrt{2}J_{z\pm}), \\ K &= -2J_{\pm\pm} + \sqrt{2}J_{z\pm}, \\ \Gamma &= \frac{1}{3}(-J_1 + \Delta J_1 - 4J_{\pm\pm} - \sqrt{2}J_{z\pm}), \\ \Gamma' &= \frac{1}{6}(-2J_1 + 2\Delta J_1 + 4J_{\pm\pm} + \sqrt{2}J_{z\pm}). \end{aligned} \quad (A3)$$

Using Eq. (A2), one can convert the comprehensive compilation of the $\{K, \Gamma, \Gamma'\}$ parameter sets of the generalized KH model (2) in Table I, which were previously proposed for α -RuCl₃, to the $\{J_1(1 - \Delta), J_{\pm\pm}, J_{z\pm}\}$ parameters of the model in the crystallographic parametrization

Reference	Method	K	Γ	Γ'	$J_{\pm\pm}$	$J_{z\pm}$	$J_1(1 - \Delta)$
Kim et al. [69]	DFT+ t/U , $P3$	-6.55	5.25	-0.95	-0.98	-6.01	-3.35
	DFT+SOC+ t/U	-8.21	4.16	-0.93	-0.33	-6.26	-2.3
	same+fixed lattice	-3.55	7.08	-0.54	-1.95	-5.27	-6.01
Winter et al. [70]	DFT+ED, $C2$	-6.67	6.6	-0.87	-1.38	-6.66	-4.87
Hou et al. [71]	DFT+ t/U , $U = 2.5\text{eV}$	-14.43	6.43		0.26	-9.84	-6.43
	same, $U = 3.0\text{eV}$	-12.23	4.83		0.43	-8.05	-4.83
	same, $U = 3.5\text{eV}$	-10.67	3.8		0.51	-6.82	-3.80
Wang et al. [72]	DFT+ t/U , $P3$	-10.9	6.1		-0.22	-8.01	-6.1
	same, $C2$	-5.5	7.6		-1.62	-6.18	-7.6
Eichstaedt et al. [73]	DFT+Wannier+ t/U	-14.3	9.8	-2.23	-1.63	-12.41	-5.33
Ran et al. [74]	LSWT, INS fit	-6.8	9.5		-2.03	-7.68	-9.5
Winter et al. [75]	<i>Ab initio</i> +INS fit	-5.0	2.5		0.0	-3.54	-2.5
Suzuki et al. [76]	ED, C_p fit	-24.41	5.25	-0.95	2.0	-14.43	-3.35
Cookmeyer et al. [77]	thermal Hall fit	-5.0	2.5		0.0	-3.54	-2.5
Wu et al. [78]	LSWT, THz fit	-2.8	2.4		-0.33	-2.45	-2.4
Ozel et al. [79]	same	-3.5	2.35		-0.2	-2.76	-2.35
Sahasrabudhe et al. [80]	ED, Raman fit	-10.0	3.75		0.42	-6.48	-3.75
Sears et al. [81]	Magnetization fit	-10.0	10.6	-0.9	-2.17	-10.14	-8.8
		-10.0	8.8		-1.27	-8.86	-8.80
Laurell et al. [82]	ED, C_p fit	-15.1	10.1	-0.12	-0.89	-11.94	-9.86
Suzuki et al. [83]	RIXS	-5.0	2.5	+0.1	0.03	-3.49	-2.7
Kaib et al. [84]	GGA+U	-10.12	9.35	-0.73	-1.67	-9.52	-7.89
Andrade et al. [85]	χ	-6.6	6.6		-1.1	-6.22	-6.6
Janssen et al. [86]	LSWT+3D	-10.0	5.0		0.0	-7.07	-5.0
Li et al. [87]	C_m , χ	-25.0	7.5	-0.5	1.5	-15.56	-6.5
Ran et al. [88]	polarized INS	-7.2	5.6		-0.67	-6.03	-5.6
Samarakoon et al. [89]	Machine learning, INS	-5.3	0.15		0.83	-2.57	-0.15
Liu et al. [90]	downfolding	-5.0	2.8	+0.7	0.13	-3.35	-4.2
This work	realistic range	[-10.0,-4.4]	[3.2,5.0]	[1.8,2.85]	[0.16,1.0]	[-5.9,-2.6]	[-10.0,-7.5]
	point 0	-7.57	4.28	2.36	0.62	-4.47	-9.0
	point A	-5.43	3.65	2.18	0.414	-3.25	-8.0
	point B	-8.73	4.71	2.39	0.68	-5.21	-9.5

TABLE II. Same as Table I with the $\{J_1(1 - \Delta), J_{\pm\pm}, J_{z\pm}\}$ parameters of the model in the crystallographic parametrization (3) converted from the generalized KH model (2) using Eq. (A2), see Secs IC 2 and II B.

(3). The result of such a conversion is presented in our Table II, see also Secs IC 2 and II B.

Appendix B: LT Details

The phase diagrams in Fig. 2, Fig. 4, Fig. 14(a), Fig. 15(a), Figs. 16(a) and (c), and Fig. 27 are obtained using the Luttinger-Tisza (LT) method [106–109]. Here we briefly outline its basics.

The goal of the LT method is to find the spin arrangement of the classical spins \mathbf{S}_i , interacting via binary interactions, that minimizes their energy under the following “strong” condition on the spin length

$$(\mathbf{S}_i)^2 = S_i^2, \quad (\text{B1})$$

where S_i is the spin length on the site i . Since, in practice, that would require a macroscopic number of Lagrange multipliers, Luttinger and Tisza introduced the so-called “weak” condition

$$\sum_i (\mathbf{S}_i)^2 = \sum_i S_i^2, \quad (\text{B2})$$

replacing the strong local condition on the spin magnitude by the global constraint on the average spin length.

The weak condition is a necessary, but not sufficient condition for the spin arrangement to satisfy the strong condition. If a solution obtained by enforcing the weak condition also fulfills the strong condition, the original problem is solved. Modifications of the LT method using alternative weak conditions have also been proposed, see Refs. [107, 146, 147].

The numerical method typically carried out today under the name of Luttinger-Tisza is simplified and involves diagonalization of the Fourier transform of the exchange matrix [61, 110, 112, 113, 124, 125, 148, 149] and finds the lower limit of the energy by applying the weak condition. In the LT approach, the lowest eigenenergy of the exchange matrix in the momentum space and the corresponding ordering vector are identified by a scan through the reciprocal space. The associated spin arrangement is found by the Fourier transform back into the real space. The implementation of the LT method is computationally straightforward.

1. LT formalism

The most general lattice Hamiltonian with binary interactions of the classical spins is given by

$$\mathcal{H} = \sum_{\langle ij \rangle} \mathbf{S}_i^T \hat{\mathbf{J}}_{ij} \mathbf{S}_j, \quad (\text{B3})$$

where the lattice indices i and j run over *all* sites of the lattice, $\langle ij \rangle$ denotes the corresponding bonds, and the 3×3 exchange matrix depends only on $\mathbf{r}_i - \mathbf{r}_j$ because of the translational invariance. To capitalize on the latter, it is convenient to rewrite the coordinates of the spins as $\mathbf{r}_i = \mathbf{R}_\ell + \boldsymbol{\rho}_\alpha$, where \mathbf{R}_ℓ is the unit cell coordinate and $\boldsymbol{\rho}_\alpha$ is the coordinate of the spin α sublattice within the unit cell. Then, the model (B3) can be rewritten as

$$\mathcal{H} = \frac{1}{2} \sum_{\ell, \ell'} \sum_{\alpha, \beta} \mathbf{S}_{\ell, \alpha}^T \hat{\mathbf{J}}_{\ell \ell'}^{\alpha \beta} \mathbf{S}_{\ell', \beta}, \quad (\text{B4})$$

separating summation over $i = \{\ell, \alpha\}$ into the ones over the unit cells and sublattices.

The Fourier transform of the 3D vectors $\mathbf{S}_{\ell, \alpha}$

$$\mathbf{S}_{\ell, \alpha} = \frac{1}{\sqrt{N}} \sum_{\mathbf{q}} \mathbf{S}_{\alpha \mathbf{q}} e^{i \mathbf{q}(\mathbf{R}_\ell + \boldsymbol{\rho}_\alpha)}, \quad (\text{B5})$$

where N is the number of unit cells, with \mathbf{R}_ℓ and $\boldsymbol{\rho}_\alpha$ defined above, allows one to rewrite the model in (B4) in the reciprocal space, using $\mathbf{S}_{\alpha - \mathbf{q}} = \mathbf{S}_{\alpha \mathbf{q}}^*$, as

$$\mathcal{H} = \sum_{\mathbf{q}} \sum_{\alpha \beta} \mathbf{S}_{\alpha \mathbf{q}}^T \hat{\mathbf{J}}_{\alpha \beta}(\mathbf{q}) \mathbf{S}_{\beta \mathbf{q}}, \quad (\text{B6})$$

with the exchange matrix $\hat{\mathbf{J}}_{\alpha \beta}(\mathbf{q})$ in the momentum space

$$\hat{\mathbf{J}}_{\alpha \beta}(\mathbf{q}) = \frac{1}{2} \sum_{\Delta \mathbf{R}_{\ell \ell'}} \hat{\mathbf{J}}_{\ell \ell'}^{\alpha \beta} e^{i \mathbf{q}(\Delta \mathbf{R}_{\ell \ell'} + \boldsymbol{\rho}_\beta - \boldsymbol{\rho}_\alpha)}, \quad (\text{B7})$$

where $\Delta \mathbf{R}_{\ell \ell'} = \mathbf{R}_{\ell'} - \mathbf{R}_\ell$.

The form in (B6) allows for a more compact writing using the “combined” vector of the spins in all sublattices

$\tilde{\mathbf{S}}^\dagger(\mathbf{q}) = (\mathbf{S}_{1 \mathbf{q}}^\dagger, \mathbf{S}_{2 \mathbf{q}}^\dagger, \dots, \mathbf{S}_{\alpha \mathbf{q}}^\dagger, \dots, \mathbf{S}_{N_s \mathbf{q}}^\dagger)$, where N_s is the number of sublattices, resulting in

$$\mathcal{H} = \sum_{\mathbf{q}} \tilde{\mathbf{S}}^\dagger(\mathbf{q}) \tilde{\mathbf{J}}(\mathbf{q}) \tilde{\mathbf{S}}(\mathbf{q}), \quad (\text{B8})$$

with the $3N_s \times 3N_s$ matrix $\tilde{\mathbf{J}}(\mathbf{q})$ built from the 3×3 blocks of $\hat{\mathbf{J}}_{\alpha \beta}(\mathbf{q})$ matrices.

Since the exchange matrix $\tilde{\mathbf{J}}(\mathbf{q})$ is hermitian, there exist unitary matrices $U(\mathbf{q})$ that diagonalize it

$$U(\mathbf{q}) \tilde{\mathbf{J}}(\mathbf{q}) U^\dagger(\mathbf{q}) = \hat{\lambda}(\mathbf{q}), \quad (\text{B9})$$

where $\hat{\lambda}(\mathbf{q})$ is a diagonal $3N_s \times 3N_s$ matrix for all \mathbf{q} .

Straightforwardly, the Hamiltonian (B8) is diagonal in the basis of the “rotated” spin vectors, $\tilde{\mathbf{S}}(\mathbf{q}) = U \tilde{\mathbf{S}}(\mathbf{q})$,

$$\mathcal{H} = \sum_{\mathbf{q}} \tilde{\mathbf{S}}^\dagger(\mathbf{q}) \hat{\lambda}(\mathbf{q}) \tilde{\mathbf{S}}(\mathbf{q}) = \sum_{\mathbf{q}, \alpha} \lambda_{\alpha \mathbf{q}} |\tilde{\mathbf{S}}_{\alpha \mathbf{q}}|^2, \quad (\text{B10})$$

with $\lambda_{\alpha \mathbf{q}}$ being the eigenvalue of the exchange matrix $\tilde{\mathbf{J}}(\mathbf{q})$ in the α -sublattice sector for a given \mathbf{q} .

If there is a momentum \mathbf{Q} at which these eigenvalues achieve the minimal $\lambda_{\mathbf{Q}}$, such that $\lambda_{\alpha \mathbf{q}} \geq \lambda_{\mathbf{Q}}$ for all \mathbf{q} and α , it means that the spin configuration minimizing the classical energy has been identified, because

$$\mathcal{H} \geq \lambda_{\mathbf{Q}} \sum_{\mathbf{q}, \alpha} |\mathbf{S}_{\alpha \mathbf{q}}|^2 = \lambda_{\mathbf{Q}} N N_s S^2, \quad (\text{B11})$$

where the assumption on spin length being the same for all sublattices, $S_i = S$, has been made for simplicity.

The connection to the LT method is in the last equation, as it corresponds to applying the weak condition in Eq. (B2),

$$\sum_{\mathbf{q}, \alpha} |\mathbf{S}_{\alpha \mathbf{q}}|^2 = \sum_{\ell, \alpha} (\mathbf{S}_{\ell, \alpha})^2 = \sum_i (\mathbf{S}_i)^2 = N N_s S^2. \quad (\text{B12})$$

One must note that the same result can be obtained by minimizing the classical energy in Eq. (B8) using the Lagrange multiplier for the weak constraint in (B2), the procedure that yields the eigenvalue problem directly for $\lambda_{\mathbf{Q}}$ [61], much in the spirit of the original LT approach.

The spin eigenstates corresponding to the minimal eigenvalues $\lambda_{\mathbf{Q}}$ found within the LT approach usually are the so-called single- \mathbf{Q} structures, for which $\mathbf{S}(\pm \mathbf{Q})$ must be kept to determine the type of the spin arrangement, although the generalizations to the multi- \mathbf{Q} states are also possible, see, e.g., Ref. [124]. In many cases, the commensurate ordering vectors \mathbf{Q} already give a clear idea of the type of spin ordering.

If the LT eigenstate also satisfies the strong constraint (B1), then LT method gives the correct classical ground state. In our case, the strong constraint is satisfied for the FM, ZZ, AFM, and stripy phases. Otherwise, it formally breaks down, see, however, the discussions in Secs. IV A 3 and III A 1.

Below, we list explicit expressions for the elements of the exchange matrices that were used to create the LT phase diagrams in Fig. 2, Fig. 4, Fig. 14(a), Fig. 15(a), Figs. 16(a) and (c), and Fig. 27.

2. Application to the $J_1 - \Delta - J_{\pm\pm} - J_{z\pm} - J_3$ and $K - J - \Gamma - \Gamma' - J_3$ honeycomb lattice models

The honeycomb lattice considered in this work is bipartite with the same spin length on each site. The couplings that are of interest for the model (1) concern the first- and the third-nearest neighbors, providing connections only between the A and B sublattices, see Fig. 1.

With that, using the primitive vectors from Fig. 1(c), $\delta_1 = a(1, 0)$ and $\delta_{2(3)} = a(-1/2, \pm\sqrt{3}/2)$, with a being the lattice spacing, and $\delta_\alpha^{(3)} = -2\delta_\alpha$, one can straightforwardly derive the elements of the Fourier transformed 3×3 exchange matrix $\hat{\mathbf{J}}_{AB}(\mathbf{q})$.

For the model (3) in the $J_1 - \Delta - J_{\pm\pm} - J_{z\pm} - J_3$ representation they are

$$\begin{aligned} J_{AB}^{xx} &= J_1\gamma_{\mathbf{q}} + 2J_{\pm\pm}\gamma'_{\mathbf{q}} + J_3\gamma_{\mathbf{q}}^{(3)}, \\ J_{AB}^{yy} &= J_1\gamma_{\mathbf{q}} - 2J_{\pm\pm}\gamma'_{\mathbf{q}} + J_3\gamma_{\mathbf{q}}^{(3)}, \\ J_{AB}^{zz} &= \Delta J_1\gamma_{\mathbf{q}} + J_3\gamma_{\mathbf{q}}^{(3)}, \\ J_{AB}^{xy} &= J_{AB}^{yx} = -2J_{\pm\pm}\gamma''_{\mathbf{q}}, \\ J_{AB}^{xz} &= J_{AB}^{zx} = J_{z\pm}\gamma''_{\mathbf{q}}, \\ J_{AB}^{yz} &= J_{AB}^{zy} = -J_{z\pm}\gamma'_{\mathbf{q}}, \end{aligned} \quad (B13)$$

where the hopping amplitudes are

$$\begin{aligned} \gamma_{\mathbf{q}} &= \sum_{\alpha} e^{i\mathbf{q}\delta_{\alpha}}, \quad \gamma_{\mathbf{q}}^{(3)} = \sum_{\alpha} e^{i\mathbf{q}\delta_{\alpha}^{(3)}}, \\ \gamma'_{\mathbf{q}} &= \sum_{\alpha} \cos \tilde{\varphi}_{\alpha} e^{i\mathbf{q}\delta_{\alpha}}, \quad \gamma''_{\mathbf{q}} = \sum_{\alpha} \sin \tilde{\varphi}_{\alpha} e^{i\mathbf{q}\delta_{\alpha}}, \end{aligned} \quad (B14)$$

and the bond-dependent phases $\tilde{\varphi}_{\alpha} = \{0, 2\pi/3, -2\pi/3\}$ for the $\alpha = \{1, 2, 3\}$ bonds in Fig. 1 are the bond angles of the primitive vectors δ_{α} with the x axis, as before. Obviously, since the real-space exchanges are real, the $\hat{\mathbf{J}}_{AB}(\mathbf{q})$ matrix is symmetric.

The matrix elements of $\hat{\mathbf{J}}_{AB}(\mathbf{q})$ in the $K - J - \Gamma - \Gamma' - J_3$ parameterization (2) are

$$\begin{aligned} J_{AB}^{xx} &= J\gamma_{\mathbf{q}} + K e^{i\mathbf{q}\delta_2} + J_3\gamma_{\mathbf{q}}^{(3)}, \\ J_{AB}^{yy} &= J\gamma_{\mathbf{q}} + K e^{i\mathbf{q}\delta_3} + J_3\gamma_{\mathbf{q}}^{(3)}, \\ J_{AB}^{zz} &= J\gamma_{\mathbf{q}} + K e^{i\mathbf{q}\delta_1} + J_3\gamma_{\mathbf{q}}^{(3)}, \\ J_{AB}^{xy} &= J_{AB}^{yx} = \Gamma e^{i\mathbf{q}\delta_1} + \Gamma' (e^{i\mathbf{q}\delta_2} + e^{i\mathbf{q}\delta_3}), \\ J_{AB}^{xz} &= J_{AB}^{zx} = \Gamma e^{i\mathbf{q}\delta_3} + \Gamma' (e^{i\mathbf{q}\delta_1} + e^{i\mathbf{q}\delta_2}), \\ J_{AB}^{yz} &= J_{AB}^{zy} = \Gamma e^{i\mathbf{q}\delta_2} + \Gamma' (e^{i\mathbf{q}\delta_1} + e^{i\mathbf{q}\delta_3}). \end{aligned} \quad (B15)$$

Using $\hat{\mathbf{J}}_{BA} = \hat{\mathbf{J}}_{AB}^\dagger$, numerical diagonalization together with the scan of the reciprocal space provide the ground state and the ordering vector \mathbf{Q} for the given choice of the model parameters. Further analysis of the spin arrangement can be done using the inverse Fourier transform of the spin eigenvectors.

Appendix C: ED Details

The exact diagonalization (ED) calculations for the phase diagrams in Figs. 3, 14(b), 15(b), and 16(b) were

performed on the high-symmetry 24-site honeycomb-lattice cluster with periodic boundary conditions, shown in Fig. 24(a). It respects all space-group symmetries of the lattice. The allowed momenta of the reciprocal space in the first three Brillouin zones are shown in Fig. 24(b) together with the high symmetry points.

The ED phase diagrams are obtained by one-dimensional sweeps along various paths through the parameter space, with the quantum model solved to find its ground state at each point of the sweep along the varying parameter X [43, 65, 118, 125, 126]. The phase boundaries are identified with the positions of the maxima in the (negative) second derivative of the ground state energy with respect to the sweeping parameter, $-\partial^2 E_0 / \partial X^2$. The momentum \mathbf{q} from the set of the allowed momenta of the cluster with the maximal static spin-structure factor

$$\mathcal{S}(\mathbf{q}) = \frac{1}{N^2} \sum_{\alpha} \sum_{\mathbf{r}, \mathbf{r}'} \langle S_{\mathbf{r}}^{\alpha} S_{\mathbf{r}'}^{\alpha} \rangle e^{i\mathbf{q}(\mathbf{r} - \mathbf{r}')},$$

provides a candidate for the ordering vector of the state in the thermodynamic limit. If no obvious dominant candidate can be found, hinting at either an incommensurate or more complicated form of ordering, the corresponding segment of the sweep is labeled as NCO for the non-commensurate order.

1. Cartesian ED phase diagrams

To obtain the phase diagrams for the Point 0, A, and B sets in Figs. 14(b), 15(b), and 3, respectively, ED sweeps where carried out in the horizontal (fixed J_3 , varying J) and vertical (fixed J , varying J_3) directions, with a discretization step of 0.01 meV within the depicted range of the phase diagrams. In Fig. 24(c), positions of the maxima of the $-\partial^2 E_0 / \partial J_{(3)}^2$ are shown as dots with the color labeling the sweep direction. The phase boundaries are then drawn by linearly interpolating these dots. Depending on the clarity of the course of the phase boundary, the distance between the sweeps was chosen to be 0.25 or 0.5 meV, with each sweep containing 500 points.

To demonstrate the process of obtaining the phase boundaries in more detail, we discuss a representative example of such an ED sweep of the phase diagram for the Point 0 parameter set in Fig. 14(b), shown in Figs. 24(d) and 24(e). It is a vertical sweep with J_3 as a varied parameter for the fixed $J = -1.25$ meV, which is shown in Fig. 24(c) by the vertical arrow. In Fig. 24(d), the ED ground state energy per site and its negative second derivative are shown. Fig. 24(e) shows the values of the static structure factor $\mathcal{S}(\mathbf{q})$ at the color-coded high-symmetry points along the sweep, with the identified phases indicated.

In the energy derivative, one can see four peaks, with the two sharp inner ones, marked as #1 and #2, and two outer ones for the smaller and larger values of J_3 , marked as #0 and #3, respectively, being considerably

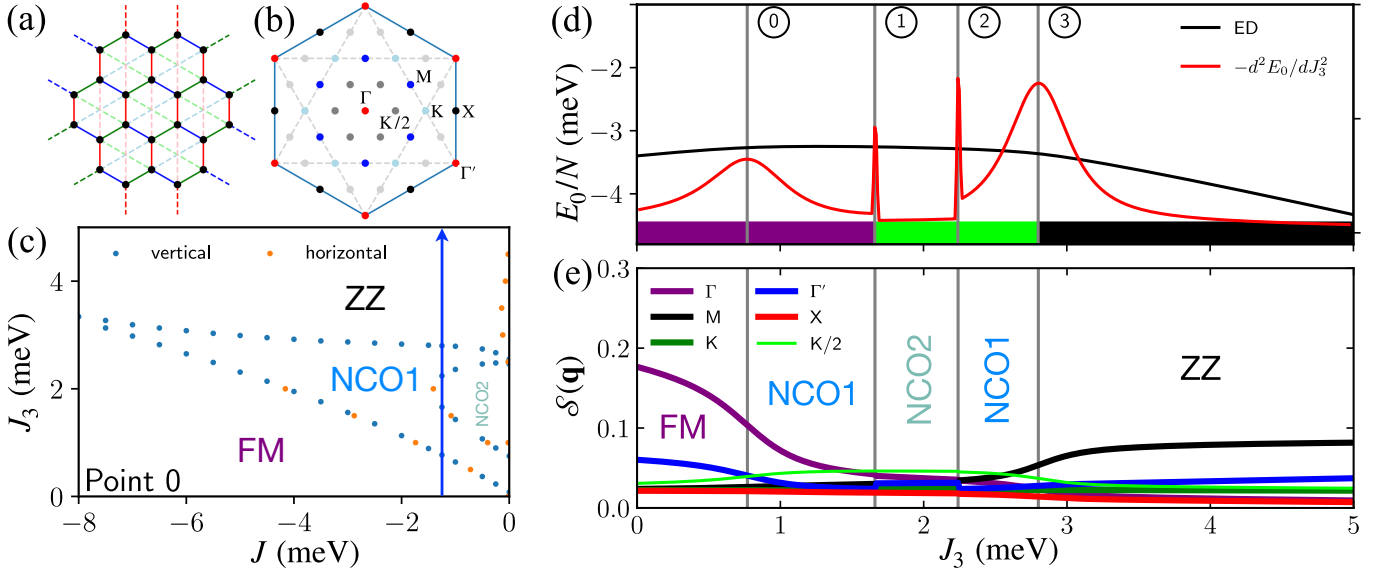


FIG. 24. (a) The 24-site cluster used in the ED calculations; the outer bonds visualize its periodicity. (b) The allowed momenta in the reciprocal space with the high-symmetry points. (c) Dots mark maxima in $-\partial^2 E_0 / \partial J_{(3)}^2$ in the vertical and horizontal sweeps for the Point 0 parameter set, see Figs. 14(b). (d) ED ground state energy per site and its second derivative vs J_3 for $J_1 = -1.25$ meV and Point 0 parameters. (e) Structure factor $\mathcal{S}(\mathbf{q})$ at the high-symmetry points for the same sweep.

broader. The sharp peaks can be taken as a signature of the singularities already in the first order derivatives of energy, implying first-order transitions, while the latter is suggestive of the more continuous phase transitions in the thermodynamic limit [150].

From the analysis of the structure factor in Fig. 24(e), the small J_3 region of the sweep spans the FM, while the large J_3 region of it belongs to the ZZ phase. The three intermediate regions have no dominant indicators of the ordering vector aside from the proximities to the FM and ZZ transitions in the two sectors marked as NCO1. They are considered as belonging to the same phase because of their continuity that is obvious from Fig. 24(c). The NCO2 phase is distinct and is carving itself a separate area of the phase diagram.

While the small size of the ED cluster should not be able to accommodate the IC1 and IC2 spiral phases discussed in Sec. IV, it is curious that it is still able to detect sharp transitions between some phases that must be reminiscent of them. It is also notable that the ED results clearly indicate a prominent intermediate region between the FM and ZZ phases, which is also in a close qualitative agreement with the LT and DMRG results.

2. Polar ED phase diagram

The polar ED phase diagram of the $J_1^{XY} - J_{z\pm} - J_3$ model discussed in Sec. III B is shown in Fig. 16(b). It is obtained using the grid of the radial, polar, and spiral sweeps, with the summary of them shown in Fig. 25(a). Each dot corresponds to a maximum in the Gaussian or Lorentzian fit of the $-\partial^2 E_0 / \partial X^2$, with $X = \{\theta, \varphi\}$ and the color labeling the sweep direction, as before.

The polar sweeps covered the entire range, $0 \leq \varphi < 2\pi$, of the polar angle, encoding the relative values of

the J_1 and J_3 terms, for the circles of different radius, which is controlled by the angle $0 \leq \theta \leq \pi/2$, encoding the $J_{z\pm}$ term. The radii were fixed at $\theta/\pi = \{1/80, 1/32, 1/16, 3/40, 7/80, 1/8, 1/5, 1/4, 3/8, 1/2\}$ with the φ step of $\pi/500$, i.e., 1000 points in a circle. In order to closely explore the region near the ZZ-FM boundary, which is of most interest, additional polar sweeps have been performed for the smaller range of φ , $3\pi/4 \leq \varphi < 5\pi/4$, for a finer mesh of radii, $\theta/\pi = \{0.34, 0.36, 0.38, 0.4, 0.42, 0.44, 0.46, 0.48, 0.5\}$, and also with the higher discretization of $\pi/2000$, corresponding to 1000 points for the sweep range.

The radial sweeps with θ were done along the radial lines of fixed $\varphi = \{0, \pi/2, \pi, 3\pi/2\}$ with a step of $\pi/1000$ for the entire range of $0 \leq \theta \leq \pi/2$. In addition, two spiral sweeps, which had both θ and φ varying along the sweep, have been performed. Both had four full rotations in φ , $0 \leq \varphi < 8\pi$, with the first varying θ from 0 to $\pi/2$, and the second from 0 to $\pi/5$, aimed at a closer investigation of the central region of the phase diagram. Both spiral sweeps had 1000 points.

Generally, because of the finite size of the ED cluster, the indicators of the transitions between different phases provided by the peaks in the energy derivative often have a finite width. This feature requires additional analysis in the cases of the two transitions coming close and peaks overlapping, such as the case shown in Fig. 25(b) and discussed below. The simple criterion for the transition as the derivative's maximum fails in these cases, while the finer step of the sweep cannot help with increasing the resolution as the width of the peak is the ED cluster property. The solution is to fit the more complicated structures in the energy derivatives by a pair of the Gaussian or Lorentzian peaks, identifying their individual maxima

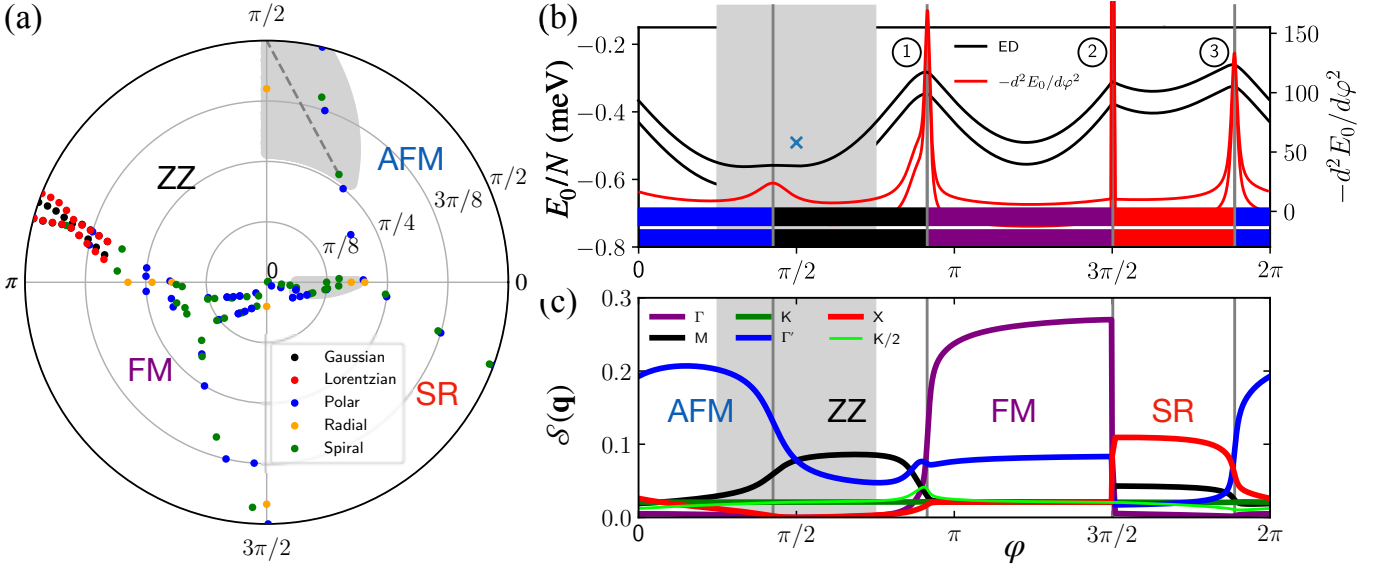


FIG. 25. (a) Same as Fig. 24(c) obtained by the polar, radial, and spiral sweeps. The Gaussian and Lorentzian fits of the close phase boundaries and the areas affected by the finite-size effects of the ED cluster, marked in gray, are discussed in text. (b) and (c) Same as Figs. 24(d) and 24(e), respectively, for $\theta = \pi/2$, see text for details.

with the phase boundaries.

The fitting procedure by the two overlapping peaks using FindFit routine in Wolfram Mathematica [151] reproduces the ED energy derivatives very well, but it leads to slightly different positions of the phase boundaries in the FM-ZZ region for the Gaussian and Lorentzian fits, see Fig. 25(a). For the phase diagram in Fig. 16, the Lorentzian border has been chosen.

In Figs. 25(b) and 25(c), we present the results for the representative polar sweep that corresponds to the circumference of the circle in Fig. 25(a), $\theta = \pi/2$, for which $J_{z\pm}$ term vanishes and the model reduces to the simpler $J_1^{XY} - J_3$ model, much studied recently [116]. Notations are the same as in Figs. 24(d) and 24(e), respectively.

We first discuss the asymmetric peak #1 in the energy derivative in Fig. 25(b), which corresponds to the proximity of the FM-ZZ boundary and is indicative of the two transitions, not one. Moreover, the structure factor in Fig. 25(c) also shows a combination of the contributions from the AFM Γ' and $K/2$ points in this region, suggesting an intermediate NCO phase. Applying the analysis of the overlapping peaks discussed above produces a clear intermediate region between the FM and ZZ phases. Its existence is also supported by a continuity argument with the $J_{z\pm} > 0$ sweeps, for which the two peaks for the transitions into the NCO phase from the neighboring FM and ZZ phases become distinct. This scenario is also in a close accord with the LT phase diagram in Fig. 16(a).

Two additional features of the sweep in Figs. 25(b) and 25(c) and of the ED phase diagram in Fig. 25(a) should be noted. Both concern the regions of the dominant J_3 , i.e., proximities of the $\varphi = \pi/2$ and $\varphi = 3\pi/2$ points with $J_1 = 0$, for which the 24-site cluster splits into three independent clusters containing only 8 sites each connected

by the sparse J_3 network.

Because of this finite-size effects, various artificial degeneracies emerge. The energy of the pure AFM J_1 model, shown in Fig. 25(b) by the cross, should be equal to that of the pure J_3 model ($\varphi = \pi/2$) in the thermodynamic limit, demonstrating strong finite-size effects for this region of φ . The affected regions are marked with gray color and the AFM-ZZ sector of the phase diagram was clarified by DMRG.

For the ferromagnetic J_3 limit ($\varphi = 3\pi/2$), the FM state is purely classical. The abrupt transition between the FM and stripe phases is also clearly reflected in the jump of the ordering vector associated with the two phases.

Altogether, the analysis provided here underscores a close quantitative unity of the results between the ED, LT, and DMRG approaches.

3. Dynamical spin-spin correlation function

The dynamical spin-spin correlation function

$$\mathcal{S}^{\mu\nu}(\mathbf{q}, \omega) = \frac{1}{2\pi} \int_{-\infty}^{\infty} e^{i\omega t} \langle S_{-\mathbf{q}}^{\mu}(t) S_{\mathbf{q}}^{\nu}(0) \rangle dt, \quad (C1)$$

can be related to various forms of dynamical structure factors, which are the subjects of ESR and INS spectroscopic experiments.

The correlation functions (C1) can be calculated numerically using ED in finite clusters, such as the one discussed in this work; see also Refs. [65, 75, 103]. ESR measures the $\mathbf{q} = 0$ sector of the dynamical structure factor, and for the results discussed in Sec. IV B, the components perpendicular to the applied field are of interest. For a field in the a -direction, the in-plane $\mathcal{S}^{bb}(0, \omega)$ component was used in Fig. 22 as a proxy for the true ESR structure factor.

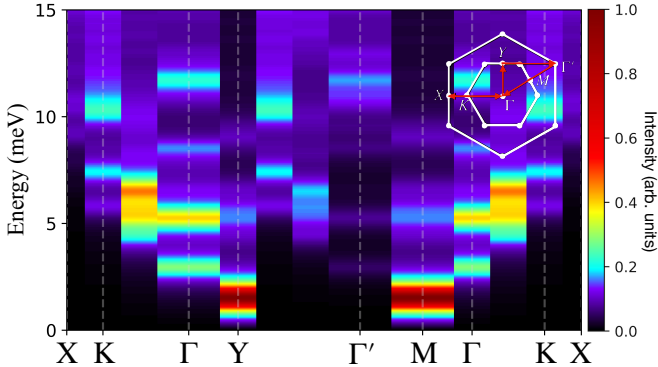


FIG. 26. The intensity map of $\mathcal{S}(\mathbf{q}, \omega)$ from Eq. (C2) for the Point \star parameter set in zero field along the \mathbf{q} -path shown in the inset.

In Figure 26 we provide an intensity plot of the sum of the diagonal components of the spin-spin correlation function from (C1)

$$\mathcal{S}(\mathbf{q}, \omega) = \sum_{\mu} \mathcal{S}^{\mu\mu}(\mathbf{q}, \omega), \quad (C2)$$

for the Point \star parameter set of model (1) in zero field. It can serve as a rough proxy for the INS dynamical structure factor [152]. Because the C_3 symmetry of the spin ground state is maintained in the ED calculations, the results in Fig. 26 also correspond to an effective averaging over the three distinct zigzag domains [75] for the Point \star set ground state.

As in the ESR comparison in Sec. IV B, the ED calculations for Fig. 26 used the Lanczos algorithm [143] and the continued fraction method [144], with a Krylov dimension of 150 and a Lorentzian broadening of 0.5 meV.

As described in Sec. V, these preliminary results require a more detailed analysis to be compared with the available INS data. However, certain improvements relative to similar comparisons using different parameter sets [75, 80] can be pointed out, such as a better quantitative matching of the lowest-energy excitations at the M- and Γ -points and a wider spectral weight distribution in the magnetic spectrum across the BZ, in accord with experimental expectations.

Appendix D: LT polar phase diagram with $J_{\pm\pm} > 0$

Our Figure 27 shows the effect of $J_{\pm\pm}$ in the full polar phase diagram obtained by the LT method, with the cutout of the FM-ZZ region from it shown in the main text in Fig. 16(c). The phase diagram is of the model (3) for the XY limit of the XXZ term, $\Delta=0$, and for a small $J_{\pm\pm}=0.05$, with J_1 and J_3 encoding the polar and $J_{z\pm}$ the radial coordinates in units of $J_1^2 + J_{z\pm}^2 + J_3^2 = 1$, as before. The choice of $J_{\pm\pm}=0.05$ is motivated by its relative value for the physical region of α -RuCl₃ parameters discussed in Sec. II B 2.

Compared to the LT phase diagram in Fig. 16(a) for $J_{\pm\pm}=0$, which shows a complete symmetry between FM and AFM and ZZ and stripe phases, respectively, such a

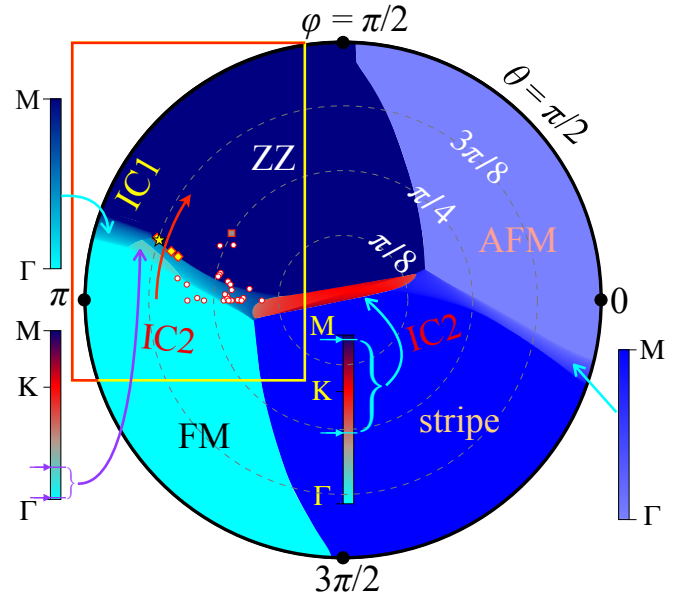


FIG. 27. Polar phase diagram of the model (3) for $\Delta=0$, $J_{\pm\pm}=0.05$, with J_1 and J_3 encoding the polar and $J_{z\pm}$ the radial coordinates in units of $J_1^2 + J_{z\pm}^2 + J_3^2 = 1$. The box shows the cutout shown in Fig. 16(c). For details, see Sec. III.

symmetry is lost in Fig. 27, suggesting a similarity between the effects of the finite $J_{\pm\pm}$ to the quantum effects observed in ED phase diagram in Fig. 16(b).

Another important effect of the finite and positive $J_{\pm\pm}$ is the protrusion of the IC2 region in the IC1 phase within the FM-ZZ quadrant, bringing a consistency of the polar phase diagram consideration with that of the Cartesian phase diagrams in the generalized KH parametrization (2) in Figs. 14 and 15, which feature both IC phases prominently. It is also relevant to the consideration of these IC phases, which are proximate to the physical parameter space of α -RuCl₃, given in Sec. IV.

In addition to the symbols representing projections of all individual α -RuCl₃ parameter sets listed in Table I onto the $\Delta=0$ plane of the phase diagram, Fig. 27 shows the group of three diamonds, which are the sets listed in Table III that were proposed in Ref. [46]. They were put forward using phenomenological constraints on the α -RuCl₃ parameters, but were deliberately not included in Table I for the sake of not skewing independent distribution of parameters from the prior literature, exposed and discussed in Sec. II B 4.

Appendix E: Classical helix ansatz

One can study incommensurate spiral phases using the general classical spin-helix ansatz, which, unlike the LT method, respects the spins' length

$$\mathbf{S}_{i,\gamma} = \mathbf{u} \cos \theta_{i,\gamma} + \mathbf{v} \sin \theta_{i,\gamma}, \quad (E1)$$

where vectors \mathbf{u} and \mathbf{v} of length $|\mathbf{u}|=|\mathbf{v}|=S$ define the plane of spins' rotation, γ is the sublattice index, and phases are $\theta_{i,\gamma} = \mathbf{Q}_{\gamma} \mathbf{r}_i + \varphi_{\gamma}$, with the propagation vector of the spiral \mathbf{Q}_{γ} and its phase shift φ_{γ} .

Reference	Method	K	Γ	Γ'	J	J_3	$J_{\pm\pm}$	$J_{z\pm}$	$J_1(1 - \Delta)$
Maksimov et al. [46]	point 1	-4.8	4.08	2.5	-2.56	2.42	0.3	-3.0	9.08
	point 2	-10.8	5.2	2.9	-4.0	3.26	1.0	-6.2	11.0
	point 3	-14.8	6.12	3.28	-4.48	3.66	1.5	-8.3	12.7

TABLE III. Same as Table II for the sets in Ref. [46], also showing J and J_3 .

For instance, the y - z and x - z helical states, such as the ones associated with, respectively, the IC1 and IC2 phases of the main text, are given by

$$\mathbf{S}_{i,\gamma} = \hat{\mathbf{y}}S \cos \theta_{i,\gamma} + \hat{\mathbf{z}}S \sin \theta_{i,\gamma}, \quad (\text{E2})$$

$$\mathbf{S}_{i,\gamma} = \hat{\mathbf{x}}S \cos \theta_{i,\gamma} + \hat{\mathbf{z}}S \sin \theta_{i,\gamma}, \quad (\text{E3})$$

see Eqs. (14) and (15) for comparison.

In addition to the spiral states, the form in Eq. (E1) can also describe *all* commensurate- \mathbf{Q} states that are discussed in this work, such as the ferromagnetic, antiferromagnetic Néel, stripe, and zigzag collinear orders.

Specifically, the choice of $\mathbf{Q} = 0$ with $\varphi_A = \varphi_B$ corresponds to a FM state, while an AFM state is associated with the same \mathbf{Q} and phases $\varphi_A = \varphi_B + \pi$. The zigzag and stripe states correspond to $\mathbf{Q} = \mathbf{G}/2 = \text{M-point}$, where \mathbf{G} is the nearest-neighbor reciprocal-lattice vector. The phases are $\varphi_A = \varphi_B$ for the stripe and $\varphi_A = \varphi_B + \pi$ for zigzag states. The values of $\varphi_{A(B)}$ phases are determined from the energy minimization and define the direction of the ordered moments in the \mathbf{u} - \mathbf{v} plane.

Using Eq. (E2) and crystallographic parametrization of the model (3), after some algebra, one can obtain the energies of the FM, AFM- z , and zigzag states, per the honeycomb-lattice unit cell and in units of S^2 , as

$$E_{\text{FM}} = 3J_1 + 3J_3 \quad (\text{E4})$$

$$E_{\text{AFM-}z} = -3\Delta J_1 - 3J_3$$

$$E_{zz} = \frac{1}{2} \left[J_1 + \Delta J_1 - 6J_3 + 4J_{\pm\pm} + (J_1 - \Delta J_1 + 4J_{\pm\pm}) \cos 2\varphi_A + 4J_{z\pm} \sin 2\varphi_A \right],$$

where $\varphi_A = \alpha$ is the out-of-plane tilt angle of the spins in Eq. (5).

Motivated by the results analyzed in Sec. IV A, we have studied the incommensurate single- \mathbf{Q} helical states with the co-rotating, $\mathbf{Q}_B = \mathbf{Q}_A$, and counter-rotating, $\mathbf{Q}_B = -\mathbf{Q}_A$ ($\varphi_B \Rightarrow -\varphi_B$), helices defined by Eq. (E1). In addition to the y - z and x - z helical states defined above, Eqs. (E2) and (E3), we have also considered the energetics of the x - y spirals that are coplanar with the \mathbf{Q} vector.

Of the considered states, the energies of the y - z and x - z counter-rotating helical states, which are close analogues of the IC1 and IC2 states discussed in Sec. IV A, are of

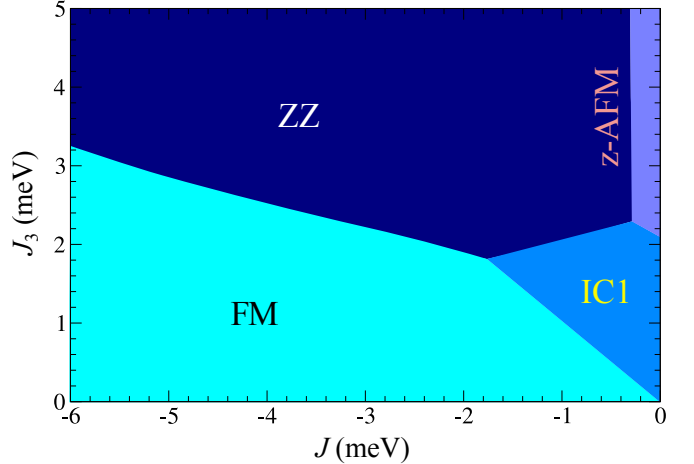


FIG. 28. Phase diagram of the model (1) using the classical helical ansatz (E1) for the Point 0 set, c.f., Fig. 14.

most interest. They are given by

$$E_{yz} = \sum_{\delta_\alpha} \left\{ \left(\frac{J_1}{2}(1 - \Delta) - J_{\pm\pm} \tilde{c}_\alpha \right) \cos(\mathbf{Q}\delta_\alpha + \Delta\varphi_{AB}) - J_{z\pm} \tilde{c}_\alpha \sin(\mathbf{Q}\delta_\alpha + \Delta\varphi_{AB}) \right\}, \quad (\text{E5})$$

$$E_{xz} = \sum_{\delta_\alpha} \left\{ \left(\frac{J_1}{2}(1 - \Delta) + J_{\pm\pm} \tilde{c}_\alpha \right) \cos(\mathbf{Q}\delta_\alpha + \Delta\varphi_{AB}) - J_{z\pm} \tilde{s}_\alpha \sin(\mathbf{Q}\delta_\alpha + \Delta\varphi_{AB}) \right\}, \quad (\text{E6})$$

in the crystallographic parametrization of the model (3), per the honeycomb-lattice unit cell, and in units of S^2 , with $\Delta\varphi_{AB} = \varphi_A - \varphi_B$ and δ_α being the nearest-neighbor vectors of the honeycomb lattice. An important feature of the results in Eqs. (E5) and (E6) is their independence of the isotropic terms of the model (1). That is, if rewritten in the generalized KH parametrization, the energies of the counter-rotating spirals depend only on the $\{K, \Gamma, \Gamma'\}$ parameter sets, the feature noticed in the discussion of such states in Sec. IV A.

Minimizing Eqs. (E5) and (E6) with respect to \mathbf{Q} and $\Delta\varphi_{AB}$, doing the same for the similar expressions for the energies of the helical states with different spin planes and co-rotating configurations, and comparing them to the energies of the commensurate states in Eq. (E4) allows one to obtain the purely classical phase diagrams of the model (1).

Our Fig. 28 shows a representative phase diagram for the Point 0 parameter set in the Cartesian J - J_3 axes of the KH parametrization, to be compared with the LT

and ED phase diagrams in Fig. 14 for the same parameters. One can see that while identical to LT regarding the commensurate FM, ZZ, and AFM phases, of the classical helical states considered here it is only IC1 (y - z) counter-rotating state that is stabilized. It is also stable in a smaller region of J and J_3 . These results underscore the importance of quantum fluctuations in stabilizing IC phases in a significantly extended parameter space.

However, we note that the classical solutions for the y - z and x - z counter-rotating helical states exhibit great

similarities to the findings presented in Sec. IV A. First of all, in both cases, the propagation vector of the helix is found to be orthogonal to the plane of spins, $\mathbf{Q} \parallel \hat{\mathbf{x}} \parallel \Gamma M$ line for the y - z (IC1) and $\mathbf{Q} \parallel \hat{\mathbf{y}} \parallel \Gamma K$ line for the x - z (IC2) helices. Then, the phase differences are found in a complete accord with the LT and DMRG results in Sec. IV A, with $\Delta\varphi_{AB}$ being zero for the IC2 state and close to 41° for the representative Point 0 parameter set in the IC1 state. Last, but not the least are close values of the IC1 and IC2 pitches of the spirals, discussed in the main text.

[1] Paramount Pictures, *Every story needs a hero*, in “Rango” (2011).

[2] U. Hilleringmann, *Silicon Semiconductor Technology* (Springer Vieweg Wiesbaden, 2023).

[3] V. Cherepanov, I. Kolokolov, and V. L’vov, The saga of YIG: Spectra, thermodynamics, interaction and relaxation of magnons in a complex magnet, *Phys. Rep.* **229**, 81 (1993).

[4] A. H. Castro Neto, F. Guinea, N. M. R. Peres, K. S. Novoselov, and A. K. Geim, The electronic properties of graphene, *Rev. Mod. Phys.* **81**, 109 (2009).

[5] L. Savary and L. Balents, Quantum spin liquids: a review, *Rep. Prog. Phys.* **80**, 016502 (2017).

[6] Y. Zhou, K. Kanoda, and T.-K. Ng, Quantum spin liquid states, *Rev. Mod. Phys.* **89**, 025003 (2017).

[7] M. R. Norman, Colloquium: Herbertsmithite and the search for the quantum spin liquid, *Rev. Mod. Phys.* **88**, 041002 (2016), and references therein.

[8] P. W. Anderson, Resonating valence bonds: A new kind of insulator?, *Mater. Res. Bull.* **8**, 153 (1973).

[9] A. Zorko, M. Herak, M. Gomilšek, J. van Tol, M. Velázquez, P. Khuntia, F. Bert, and P. Mendels, Symmetry reduction in the quantum kagome antiferromagnet herbertsmithite, *Phys. Rev. Lett.* **118**, 017202 (2017).

[10] C. Claus, Fortsetzung der Untersuchung des Platinrückstandes, nebst vorläufiger Ankündigung eines neuen Metalles, *J. Prak. Chem.* **34**, 420 (1845).

[11] A. Kitaev, Anyons in an exactly solved model and beyond, *Annals of Physics* **321**, 2 (2006).

[12] K. Hyde, E. Hooper, J. Waters, and J. Fletcher, α - and β -ruthenium trichloride, *J. Less Common Metals* **8**, 428 (1965).

[13] J. M. Fletcher, W. E. Gardner, A. C. Fox, and G. Topping, X-ray, infrared, and magnetic studies of α - and β -ruthenium trichloride, *J. Chem. Soc. A*, 1038 (1967).

[14] S. M. Winter, A. A. Tsirlin, M. Daghofer, J. van den Brink, Y. Singh, P. Gegenwart, and R. R. Valentí, Models and Materials for Generalized Kitaev Magnetism, *J. Phys.: Condens. Matter* **29**, 493002 (2017), and references therein.

[15] L. Binotto, I. Pollini, and G. Spinolo, Optical and transport properties of the magnetic semiconductor α -RuCl₃, *Phys. Status Solidi B* **44**, 245 (1971).

[16] S. Rojas and G. Spinolo, Hall effect in α -RuCl₃, *Solid State Commun.* **48**, 349 (1983).

[17] I. Pollini, Electronic properties of the narrow-band material α -RuCl₃, *Phys. Rev. B* **53**, 12769 (1996).

[18] K. W. Plumb, J. P. Clancy, L. J. Sandilands, V. V. Shankar, Y. F. Hu, K. S. Burch, H.-Y. Kee, and Y.-J. Kim, α -RuCl₃: A spin-orbit assisted Mott insulator on a honeycomb lattice, *Phys. Rev. B* **90**, 041112 (2014).

[19] M. McGuire, Crystal and magnetic structures in layered, transition metal dihalides and trihalides, *Crystals* **7**, 121 (2017).

[20] Y. Kobayashi, T. Okada, K. Asai, M. Katada, H. Sano, and F. Ambe, Mössbauer Spectroscopy and Magnetization Studies of α - and β -RuCl₃, *Inorg. Chem.* **31**, 4570 (1992).

[21] J. A. Sears, M. Songvilay, K. W. Plumb, J. P. Clancy, Y. Qiu, Y. Zhao, D. Parshall, and Y.-J. Kim, Magnetic order in α -RuCl₃: A honeycomb-lattice quantum magnet with strong spin-orbit coupling, *Phys. Rev. B* **91**, 144420 (2015).

[22] R. D. Johnson, S. C. Williams, A. A. Haghhighirad, J. Singleton, V. Zapf, P. Manuel, I. I. Mazin, Y. Li, H. O. Jeschke, R. Valentí, and R. Coldea, Monoclinic crystal structure of α -RuCl₃ and the zigzag antiferromagnetic ground state, *Phys. Rev. B* **92**, 235119 (2015).

[23] K. I. Kugel’ and D. I. Khomskii, The Jahn-Teller effect and magnetism: transition metal compounds, *Sov. Phys. Usp.* **25**, 231 (1982).

[24] G. Jackeli and G. Khaliullin, Mott Insulators in the Strong Spin-Orbit Coupling Limit: From Heisenberg to a Quantum Compass and Kitaev Models, *Phys. Rev. Lett.* **102**, 017205 (2009).

[25] J. Chaloupka, G. Jackeli, and G. Khaliullin, Kitaev-Heisenberg Model on a Honeycomb Lattice: Possible Exotic Phases in Iridium Oxides $A_2\text{IrO}_3$, *Phys. Rev. Lett.* **105**, 027204 (2010).

[26] H. B. Cao, A. Banerjee, J.-Q. Yan, C. A. Bridges, M. D. Lumsden, D. G. Mandrus, D. A. Tennant, B. C. Chakoumakos, and S. E. Nagler, Low-temperature crystal and magnetic structure of α -RuCl₃, *Phys. Rev. B* **93**, 134423 (2016).

[27] L. J. Sandilands, Y. Tian, K. W. Plumb, Y.-J. Kim, and K. S. Burch, Scattering Continuum and Possible Fractionalized Excitations in α -RuCl₃, *Phys. Rev. Lett.* **114**, 147201 (2015).

[28] A. Banerjee, C. A. Bridges, J.-Q. Yan, A. A. Aczel, L. Li, M. B. Stone, G. E. Granroth, M. D. Lumsden, Y. Yiu, J. Knolle, S. Bhattacharjee, D. L. Kovrizhin, R. Moessner, D. A. Tennant, D. G. Mandrus, and S. E. Nagler, Proximate Kitaev quantum spin liquid be-

haviour in a honeycomb magnet, *Nat. Mater.* **15**, 733 (2016).

[29] A. N. Ponomaryov, E. Schulze, J. Wosnitza, P. Lampen-Kelley, A. Banerjee, J.-Q. Yan, C. A. Bridges, D. G. Mandrus, S. E. Nagler, A. K. Kolezhuk, and S. A. Zvyagin, Unconventional spin dynamics in the honeycomb-lattice material α -RuCl₃: High-field electron spin resonance studies, *Phys. Rev. B* **96**, 241107(R) (2017).

[30] A. Banerjee, J. Yan, J. Knolle, C. A. Bridges, M. B. Stone, M. D. Lumsden, D. G. Mandrus, D. A. Tennant, R. Moessner, and S. E. Nagler, Neutron scattering in the proximate quantum spin liquid α -RuCl₃, *Science* **356**, 1055 (2017).

[31] A. Banerjee, P. Lampen-Kelley, J. Knolle, C. Balz, A. A. Aczel, B. Winn, Y. Liu, D. Pajerowski, J. Yan, C. A. Bridges, A. T. Savici, B. C. Chakoumakos, M. D. Lumsden, D. A. Tennant, R. Moessner, D. G. Mandrus, and S. E. Nagler, Excitations in the field-induced quantum spin liquid state of α -RuCl₃, *npj Quantum Mater.* **3**, 8 (2018).

[32] T. Yokoi, S. Ma, Y. Kasahara, S. Kasahara, T. Shibauchi, N. Kurita, H. Tanaka, J. Nasu, Y. Motome, C. Hickey, S. Trebst, and Y. Matsuda, Half-integer quantized anomalous thermal Hall effect in the Kitaev material candidate α -RuCl₃, *Science* **373**, 568 (2021).

[33] Y. Kasahara, T. Ohnishi, Y. Mizukami, O. Tanaka, S. Ma, K. Sugii, N. Kurita, H. Tanaka, J. Nasu, Y. Motome, T. Shibauchi, and Y. Matsuda, Majorana quantization and half-integer thermal quantum Hall effect in a Kitaev spin liquid, *Nature* **559**, 227 (2018).

[34] Y. Kasahara, K. Sugii, T. Ohnishi, M. Shimozawa, M. Yamashita, N. Kurita, H. Tanaka, J. Nasu, Y. Motome, T. Shibauchi, and Y. Matsuda, Unusual Thermal Hall Effect in a Kitaev Spin Liquid Candidate α -RuCl₃, *Phys. Rev. Lett.* **120**, 217205 (2018).

[35] P. Czajka, T. Gao, M. Hirschberger, P. Lampen-Kelley, A. Banerjee, J. Yan, D. G. Mandrus, S. E. Nagler, and N. P. Ong, Oscillations of the thermal conductivity in the spin-liquid state of α -RuCl₃, *Nat. Phys.* **17**, 915 (2021).

[36] M. Ye, G. B. Halász, L. Savary, and L. Balents, Quantization of the Thermal Hall Conductivity at Small Hall Angles, *Phys. Rev. Lett.* **121**, 147201 (2018).

[37] Y. Vinkler-Aviv and A. Rosch, Approximately Quantized Thermal Hall Effect of Chiral Liquids Coupled to Phonons, *Phys. Rev. X* **8**, 031032 (2018).

[38] J. A. N. Bruin, R. R. Claus, Y. Matsumoto, N. Kurita, H. Tanaka, and H. Takagi, Robustness of the thermal Hall effect close to half-quantization in α -RuCl₃, *Nat. Phys.* **18**, 401 (2022).

[39] H. Takagi, T. Takayama, G. Jackeli, G. Khaliullin, and S. E. Nagler, Concept and realization of Kitaev quantum spin liquids, *Nat. Rev. Phys.* **1**, 264 (2019).

[40] D. A. S. Kaib, S. M. Winter, and R. Valentí, Kitaev honeycomb models in magnetic fields: Dynamical response and dual models, *Phys. Rev. B* **100**, 144445 (2019).

[41] M. Hermanns, I. Kimchi, and J. Knolle, Physics of the Kitaev Model: Fractionalization, Dynamic Correlations, and Material Connections, *Annu. Rev. Condens. Matter Phys.* **9**, 17 (2018).

[42] Y. Motome and J. Nasu, Hunting Majorana Fermions in Kitaev Magnets, *J. Phys. Soc. Jpn.* **89**, 012002 (2020).

[43] S. Trebst and C. Hickey, Kitaev materials, *Phys. Rep.* **950**, 1 (2022).

[44] I. Rouschatzakis, N. B. Perkins, Q. Luo, and H.-Y. Kee, Beyond Kitaev physics in strong spin-orbit coupled magnets, *Rep. Prog. Phys.* **87**, 026502 (2024).

[45] Y. Matsuda, T. Shibauchi, and H.-Y. Kee, Kitaev Quantum Spin Liquids (2025), arXiv:2501.05608 [cond-mat.str-el].

[46] P. A. Maksimov and A. L. Chernyshev, Rethinking α -RuCl₃, *Phys. Rev. Res.* **2**, 033011 (2020), and references therein.

[47] C. Balz, P. Lampen-Kelley, A. Banerjee, J. Yan, Z. Lu, X. Hu, S. M. Yadav, Y. Takano, Y. Liu, D. A. Tennant, M. D. Lumsden, D. Mandrus, and S. E. Nagler, Finite field regime for a quantum spin liquid in α -RuCl₃, *Phys. Rev. B* **100**, 060405 (2019).

[48] R. L. Smit, S. Keupert, O. Tsypliyatyev, P. A. Maksimov, A. L. Chernyshev, and P. Kopietz, Magnon damping in the zigzag phase of the kitaev-heisenberg- Γ model on a honeycomb lattice, *Phys. Rev. B* **101**, 054424 (2020).

[49] E. Lefrançois, G. Grissonnanche, J. Baglo, P. Lampen-Kelley, J.-Q. Yan, C. Balz, D. Mandrus, S. E. Nagler, S. Kim, Y.-J. Kim, N. Doiron-Leyraud, and L. Taillefer, Evidence of a Phonon Hall Effect in the Kitaev Spin Liquid Candidate α -RuCl₃, *Phys. Rev. X* **12**, 021025 (2022).

[50] L. Chen, E. Lefrançois, A. Vallipuram, Q. Barthélémy, A. Ataei, W. Yao, Y. Li, and L. Taillefer, Planar thermal Hall effect from phonons in a Kitaev candidate material, *Nat. Commun.* **15**, 3513 (2024).

[51] E. Lefrançois, J. Baglo, Q. Barthélémy, S. Kim, Y.-J. Kim, and L. Taillefer, Oscillations in the magnetothermal conductivity of α -RuCl₃: Evidence of transition anomalies, *Phys. Rev. B* **107**, 064408 (2023).

[52] S. Li and S. Okamoto, Thermal Hall effect in the Kitaev-Heisenberg system with spin-phonon coupling, *Phys. Rev. B* **106**, 024413 (2022).

[53] J. A. N. Bruin, R. R. Claus, Y. Matsumoto, J. Nuss, S. Laha, B. V. Lotsch, N. Kurita, H. Tanaka, and H. Takagi, Origin of oscillatory structures in the magnetothermal conductivity of the putative Kitaev magnet α -RuCl₃, *APL Materials* **10**, 090703 (2022).

[54] L. Mangeolle, L. Balents, and L. Savary, Phonon Thermal Hall Conductivity from Scattering with Collective Fluctuations, *Phys. Rev. X* **12**, 041031 (2022).

[55] S. Li, H. Yan, and A. H. Nevidomskyy, Magnons, Phonons, and Thermal Hall Effect in Candidate Kitaev Magnet α -RuCl₃ (2023), arXiv:2301.07401 [cond-mat.str-el].

[56] R. Dhakal, D. A. S. Kaib, S. Biswas, R. Valentí, and S. M. Winter, Spin-Phonon Coupling in Transition Metal Insulators II: Spin-Orbital Moments, Chiral Phonons and Application to α -RuCl₃ (2024), arXiv:2407.00660 [cond-mat.str-el].

[57] J. G. Rau and H.-Y. Kee, Trigonal distortion in the honeycomb iridates: Proximity of zigzag and spiral phases in Na₂IrO₃ (2014), arXiv:1408.4811 [cond-mat.str-el].

[58] J. G. Rau, E. K.-H. Lee, and H.-Y. Kee, Generic Spin Model for the Honeycomb Iridates beyond the Kitaev Limit, *Phys. Rev. Lett.* **112**, 077204 (2014).

[59] J. Nasu, J. Knolle, D. L. Kovrizhin, Y. Motome, and R. Moessner, Fermionic response from fractionalization in an insulating two-dimensional magnet, *Nat. Phys.* **12**, 912 (2016).

[60] S.-H. Do, S.-Y. Park, J. Yoshitake, J. Nasu, Y. Motome, Y.-S. Kwon, D. T. Adroja, D. J. Voneshen, K. Kim, T.-H. Jang, J.-H. Park, K.-Y. Choi, and S. Ji, Majorana fermions in the Kitaev quantum spin system α -RuCl₃, *Nat. Phys.* **13**, 1079 (2017).

[61] I. Rousochatzakis, J. Reuther, R. Thomale, S. Rachel, and N. B. Perkins, Phase Diagram and Quantum Order by Disorder in the Kitaev K₁-K₂ Honeycomb Magnet, *Phys. Rev. X* **5**, 041035 (2015).

[62] R. Yadav, N. A. Bogdanov, V. M. Katukuri, S. Nishimoto, J. van den Brink, and L. Hozoi, Kitaev exchange and field-induced quantum spin-liquid states in honeycomb α -RuCl₃, *Sci. Rep.* **6**, 1 (2016).

[63] H.-S. Kim, V. V. Shankar, A. Catuneanu, and H.-Y. Kee, Kitaev magnetism in honeycomb RuCl₃ with intermediate spin-orbit coupling, *Phys. Rev. B* **91**, 241110 (2015).

[64] J. Chaloupka and G. Khaliullin, Magnetic anisotropy in the Kitaev model systems Na₂IrO₃ and RuCl₃, *Phys. Rev. B* **94**, 064435 (2016).

[65] S. M. Winter, K. Riedl, D. Kaib, R. Coldea, and R. Valentí, Probing α -RuCl₃ Beyond Magnetic Order: Effects of Temperature and Magnetic Field, *Phys. Rev. Lett.* **120**, 077203 (2018).

[66] L. Janssen, E. C. Andrade, and M. Vojta, Magnetization processes of zigzag states on the honeycomb lattice: Identifying spin models for α -RuCl₃ and Na₂IrO₃, *Phys. Rev. B* **96**, 064430 (2017).

[67] C. Balz, L. Janssen, P. Lampen-Kelley, A. Banerjee, Y. H. Liu, J.-Q. Yan, D. G. Mandrus, M. Vojta, and S. E. Nagler, Field-induced intermediate ordered phase and anisotropic interlayer interactions in α -RuCl₃, *Phys. Rev. B* **103**, 174417 (2021).

[68] P. Lampen-Kelley, S. Rachel, J. Reuther, J.-Q. Yan, A. Banerjee, C. A. Bridges, H. B. Cao, S. E. Nagler, and D. Mandrus, Anisotropic susceptibilities in the honeycomb Kitaev system α -RuCl₃, *Phys. Rev. B* **98**, 100403(R) (2018).

[69] H.-S. Kim and H.-Y. Kee, Crystal structure and magnetism in α -RuCl₃: An *ab initio* study, *Phys. Rev. B* **93**, 155143 (2016).

[70] S. M. Winter, Y. Li, H. O. Jeschke, and R. Valentí, Challenges in design of Kitaev materials: Magnetic interactions from competing energy scales, *Phys. Rev. B* **93**, 214431 (2016).

[71] Y. S. Hou, H. J. Xiang, and X. G. Gong, Unveiling magnetic interactions of ruthenium trichloride via constraining direction of orbital moments: Potential routes to realize a quantum spin liquid, *Phys. Rev. B* **96**, 054410 (2017).

[72] W. Wang, Z.-Y. Dong, S.-L. Yu, and J.-X. Li, Theoretical investigation of magnetic dynamics in α -RuCl₃, *Phys. Rev. B* **96**, 115103 (2017).

[73] C. Eichstaedt, Y. Zhang, P. Laurell, S. Okamoto, A. G. Eguiluz, and T. Berlijn, Deriving models for the Kitaev spin-liquid candidate material α -RuCl₃ from first principles, *Phys. Rev. B* **100**, 075110 (2019).

[74] K. Ran, J. Wang, W. Wang, Z.-Y. Dong, X. Ren, S. Bao, S. Li, Z. Ma, Y. Gan, Y. Zhang, J. T. Park, G. Deng, S. Danilkin, S.-L. Yu, J.-X. Li, and J. Wen, Spin-Wave Excitations Evidencing the Kitaev Interaction in Single Crystalline α -RuCl₃, *Phys. Rev. Lett.* **118**, 107203 (2017).

[75] S. M. Winter, K. Riedl, P. A. Maksimov, A. L. Cherny- shev, A. Honecker, and R. Valentí, Breakdown of magnons in a strongly spin-orbital coupled magnet, *Nat. Commun.* **8**, 1152 (2017).

[76] T. Suzuki and S. Suga, Effective model with strong Kitaev interactions for α -RuCl₃, *Phys. Rev. B* **97**, 134424 (2018).

[77] J. Cookmeyer and J. E. Moore, Spin-wave analysis of the low-temperature thermal Hall effect in the candidate Kitaev spin liquid α -RuCl₃, *Phys. Rev. B* **98**, 060412 (2018).

[78] L. Wu, A. Little, E. E. Aldape, D. Rees, E. Thewalt, P. Lampen-Kelley, A. Banerjee, C. A. Bridges, J.-Q. Yan, D. Boone, S. Patankar, D. Goldhaber-Gordon, D. Mandrus, S. E. Nagler, E. Altman, and J. Orenstein, Field evolution of magnons in α -RuCl₃ by high-resolution polarized terahertz spectroscopy, *Phys. Rev. B* **98**, 094425 (2018).

[79] I. O. Ozel, C. A. Belvin, E. Baldini, I. Kimchi, S. Do, K.-Y. Choi, and N. Gedik, Magnetic field-dependent low-energy magnon dynamics in α -RuCl₃, *Phys. Rev. B* **100**, 085108 (2019).

[80] A. Sahasrabudhe, D. A. S. Kaib, S. Reschke, R. German, T. C. Koethe, J. Buhot, D. Kamenskyi, C. Hickey, P. Becker, V. Tsurkan, A. Loidl, S. H. Do, K. Y. Choi, M. Grüninger, S. M. Winter, Z. Wang, R. Valentí, and P. H. M. van Loosdrecht, High-field quantum disordered state in α -RuCl₃: Spin flips, bound states, and a multi-particle continuum, *Phys. Rev. B* **101**, 140410 (2020).

[81] J. A. Sears, L. E. Chern, S. Kim, P. J. Bereciartua, S. Francoual, Y. B. Kim, and Y.-J. Kim, Ferromagnetic Kitaev interaction and the origin of large magnetic anisotropy in α -RuCl₃, *Nat. Phys.* **16**, 837 (2020).

[82] P. Laurell and S. Okamoto, Dynamical and thermal magnetic properties of the Kitaev spin liquid candidate α -RuCl₃, *npj Quantum Mater.* **5**, 2 (2020).

[83] H. Suzuki, H. Liu, J. Bertinshaw, K. Ueda, H. Kim, S. Laha, D. Weber, Z. Yang, L. Wang, H. Takahashi, K. Fúrsich, M. Minola, B. V. Lotsch, B. J. Kim, H. Yavas, M. Daghofer, J. Chaloupka, G. Khaliullin, H. Gretarsson, and B. Keimer, Proximate ferromagnetic state in the Kitaev model material α -RuCl₃, *Nat. Commun.* **12**, 4512 (2021).

[84] D. A. S. Kaib, S. Biswas, K. Riedl, S. M. Winter, and R. Valentí, Magnetoelastic coupling and effects of uniaxial strain in α -RuCl₃ from first principles, *Phys. Rev. B* **103**, L140402 (2021).

[85] E. C. Andrade, L. Janssen, and M. Vojta, Susceptibility anisotropy and its disorder evolution in models for Kitaev materials, *Phys. Rev. B* **102**, 115160 (2020).

[86] L. Janssen, S. Koch, and M. Vojta, Magnon dispersion and dynamic spin response in three-dimensional spin models for α -RuCl₃, *Phys. Rev. B* **101**, 174444 (2020).

[87] H. Li, H.-K. Zhang, J. Wang, H.-Q. Wu, Y. Gao, D.-W. Qu, Z.-X. Liu, S.-S. Gong, and W. Li, Identification of magnetic interactions and high-field quantum spin liquid in α -RuCl₃, *Nat. Commun.* **12**, 4007 (2021).

[88] K. Ran, J. Wang, S. Bao, Z. Cai, Y. Shangguan, Z. Ma, W. Wang, Z.-Y. Dong, P. Cermák, A. Schneidewind, S. Meng, Z. Lu, S.-L. Yu, J.-X. Li, and J. Wen, Evidence for Magnetic Fractional Excitations in a Kitaev Quantum-Spin-Liquid Candidate α -RuCl₃, *Chin. Phys. Lett.* **39**, 027501 (2022).

[89] A. M. Samarakoon, P. Laurell, C. Balz, A. Banerjee, P. Lampen-Kelley, D. Mandrus, S. E. Nagler,

S. Okamoto, and D. A. Tennant, Extraction of interaction parameters for α -RuCl₃ from neutron data using machine learning, *Phys. Rev. Res.* **4**, L022061 (2022).

[90] H. Liu, J. Chaloupka, and G. Khaliullin, Exchange interactions in $d5$ Kitaev materials: From Na₂IrO₃ to α -RuCl₃, *Phys. Rev. B* **105**, 214411 (2022).

[91] N. Rao, K. Liu, M. Machaczek, and L. Pollet, Machine-learned phase diagrams of generalized Kitaev honeycomb magnets, *Phys. Rev. Res.* **3**, 033223 (2021).

[92] D. A. S. Kaib, K. Riedl, A. Razpopov, Y. Li, S. Backes, I. I. Mazin, and R. Valentí, Electronic and magnetic properties of the RuX₃ (X=Cl, Br, I) family: two siblings—and a cousin?, *npj Quantum Mater.* **7**, 75 (2022).

[93] J. G. Rau, E. K.-H. Lee, and H.-Y. Kee, Spin-Orbit Physics Giving Rise to Novel Phases in Correlated Systems: Iridates and Related Materials, *Annu. Rev. Condens. Matter Phys.* **7**, 195 (2016).

[94] N. J. Robinson, F. H. L. Essler, I. Cabrera, and R. Coldea, Quasiparticle breakdown in the quasi-one-dimensional Ising ferromagnet CoNb₂O₆, *Phys. Rev. B* **90**, 174406 (2014).

[95] Y. Li, P. Gegenwart, and A. A. Tsirlin, Spin liquids in geometrically perfect triangular antiferromagnets, *J. Phys.: Condens. Matter* **32**, 224004 (2020).

[96] R. Coldea, D. A. Tennant, K. Habicht, P. Smeibidl, C. Wolters, and Z. Tyleczynski, Direct Measurement of the Spin Hamiltonian and Observation of Condensation of Magnons in the 2D Frustrated Quantum Magnet Cs₂CuCl₄, *Phys. Rev. Lett.* **88**, 137203 (2002).

[97] M. Mourigal, M. Enderle, A. Klöpperpieper, J.-S. Caux, A. Stunault, and H. M. Rønnow, Fractional spinon excitations in the quantum Heisenberg antiferromagnetic chain, *Nat. Phys.* **9**, 435 (2013).

[98] J. A. M. Paddison, M. Daum, Z. Dun, G. Ehlers, Y. Liu, M. B. Stone, H. Zhou, and M. Mourigal, Continuous excitations of the triangular-lattice quantum spin liquid YbMgGaO₄, *Nat. Phys.* **13**, 117 (2017).

[99] K. A. Ross, L. Savary, B. D. Gaulin, and L. Balents, Quantum Excitations in Quantum Spin Ice, *Phys. Rev. X* **1**, 021002 (2011).

[100] J. D. Thompson, P. A. McClarty, D. Prabhakaran, I. Cabrera, T. Guidi, and R. Coldea, Quasiparticle Breakdown and Spin Hamiltonian of the Frustrated Quantum Pyrochlore Yb₂Ti₂O₇ in a Magnetic Field, *Phys. Rev. Lett.* **119**, 057203 (2017).

[101] J. G. Rau, R. Moessner, and P. A. McClarty, Magnon interactions in the frustrated pyrochlore ferromagnet Yb₂Ti₂O₇, *Phys. Rev. B* **100**, 104423 (2019).

[102] L. Woodland, D. Macdougal, I. M. Cabrera, J. D. Thompson, D. Prabhakaran, R. I. Bewley, and R. Coldea, Tuning the confinement potential between spinons in the Ising chain compound CoNb₂O₆ using longitudinal fields and quantitative determination of the microscopic Hamiltonian, *Phys. Rev. B* **108**, 184416 (2023).

[103] T. Xie, S. Gozel, J. Xing, N. Zhao, S. M. Avdoshenko, L. Wu, A. S. Sefat, A. L. Chernyshev, A. M. Läuchli, A. Podlesnyak, and S. E. Nikitin, Quantum Spin Dynamics Due to Strong Kitaev Interactions in the Triangular-Lattice Antiferromagnet CsCeSe₂, *Phys. Rev. Lett.* **133**, 096703 (2024).

[104] S. Kim, E. Horsley, C. Nelson, J. Ruff, and Y.-J. Kim, Re-investigation of Moment Direction in a Kitaev Material α -RuCl₃ (2024), arXiv:2403.04176 [cond-mat.str-el].

[105] A. N. Ponomaryov, L. Zviagina, J. Wosnitza, P. Lampen-Kelley, A. Banerjee, J.-Q. Yan, C. A. Bridges, D. G. Mandrus, S. E. Nagler, and S. A. Zvyagin, Nature of Magnetic Excitations in the High-Field Phase of α -RuCl₃, *Phys. Rev. Lett.* **125**, 037202 (2020).

[106] J. M. Luttinger and L. Tisza, Theory of Dipole Interaction in Crystals, *Phys. Rev.* **70**, 954 (1946).

[107] D. H. Lyons and T. A. Kaplan, Method for Determining Ground-State Spin Configurations, *Phys. Rev.* **120**, 1580 (1960).

[108] Z. Friedman and J. Felsteiner, On the solution of the Luttinger-Tisza problem for magnetic systems, *Philos. Mag.* **29**, 957 (1974).

[109] D. B. Litvin, The Luttinger-Tisza method, *Physica* **77**, 205 (1974).

[110] N. Niggemann, M. Hering, and J. Reuther, Classical spiral spin liquids as a possible route to quantum spin liquids, *J. Phys.: Condens. Matter* **32**, 024001 (2019).

[111] J. Chaloupka and G. Khaliullin, Hidden symmetries of the extended Kitaev-Heisenberg model: Implications for the honeycomb-lattice iridates A₂IrO₃, *Phys. Rev. B* **92**, 024413 (2015).

[112] P. A. Maksimov and A. L. Chernyshev, Easy-plane anisotropic-exchange magnets on a honeycomb lattice: Quantum effects and dealing with them, *Phys. Rev. B* **106**, 214411 (2022).

[113] P. A. Maksimov, Z. Zhu, S. R. White, and A. L. Chernyshev, Anisotropic-Exchange Magnets on a Triangular Lattice: Spin Waves, Accidental Degeneracies, and Dual Spin Liquids, *Phys. Rev. X* **9**, 021017 (2019).

[114] J. G. Rau and M. J. P. Gingras, Frustration and anisotropic exchange in ytterbium magnets with edge-shared octahedra, *Phys. Rev. B* **98**, 054408 (2018).

[115] E. Rastelli, A. Tassi, and L. Reatto, Non-simple magnetic order for simple Hamiltonians, *Physica B+C* **97**, 1 (1979).

[116] S. Jiang, S. R. White, and A. L. Chernyshev, Quantum phases in the honeycomb-lattice J_1 - J_3 ferro-antiferromagnetic model, *Phys. Rev. B* **108**, L180406 (2023).

[117] A. Bose, M. Routh, S. Voleti, S. K. Saha, M. Kumar, T. Saha-Dasgupta, and A. Paramekanti, Proximate Dirac spin liquid in the honeycomb lattice J_1 - J_3 XXZ model: Numerical study and application to cobaltates, *Phys. Rev. B* **108**, 174422 (2023).

[118] Y. Watanabe, S. Trebst, and C. Hickey, Frustrated Ferromagnetism of Honeycomb Cobaltates: Incommensurate Spirals, Quantum Disordered Phases, and Out-of-Plane Ising Order (2022), arXiv:2212.14053 [cond-mat.str-el].

[119] T. Halloran, F. Desrochers, E. Z. Zhang, T. Chen, L. E. Chern, Z. Xu, B. Winn, M. Graves-Brook, M. B. Stone, A. I. Kolesnikov, Y. Qiu, R. Zhong, R. Cava, Y. B. Kim, and C. Broholm, Geometrical frustration versus Kitaev interactions in BaCo₂(AsO₄)₂, *Proc. Natl. Acad. Sci. U.S.A.* **120**, e2215509119 (2023).

[120] C. A. Gallegos and A. L. Chernyshev, Magnon interactions in the quantum paramagnetic phase of CoNb₂O₆, *Phys. Rev. B* **109**, 014424 (2024).

[121] Y. Kubota, H. Tanaka, T. Ono, Y. Narumi, and K. Kindo, Successive magnetic phase transitions in α -RuCl₃: XY-like frustrated magnet on the honeycomb lattice, *Phys. Rev. B* **91**, 094422 (2015).

[122] P. M. Cônsoli, L. Janssen, M. Vojta, and E. C. Andrade, Heisenberg-Kitaev model in a magnetic field: $1/S$ expansion, *Phys. Rev. B* **102**, 155134 (2020).

[123] J. A. Sears, Y. Zhao, Z. Xu, J. W. Lynn, and Y.-J. Kim, Phase diagram of α -RuCl₃ in an in-plane magnetic field, *Phys. Rev. B* **95**, 180411 (2017).

[124] C. Liu, R. Yu, and X. Wang, Semiclassical ground-state phase diagram and multi- Q phase of a spin-orbit-coupled model on triangular lattice, *Phys. Rev. B* **94**, 174424 (2016).

[125] Q. Luo, S. Hu, B. Xi, J. Zhao, and X. Wang, Ground-state phase diagram of an anisotropic spin- $\frac{1}{2}$ model on the triangular lattice, *Phys. Rev. B* **95**, 165110 (2017).

[126] M. Becker, M. Hermanns, B. Bauer, M. Garst, and S. Trebst, Spin-orbit physics of $j = \frac{1}{2}$ Mott insulators on the triangular lattice, *Phys. Rev. B* **91**, 155135 (2015).

[127] I. A. Zaliznyak and M. E. Zhitomirsky, Modification of the classical Heisenberg helimagnet by weak uniaxial anisotropy and magnetic field, *JETP* **81**, 568 (1995).

[128] I. Kimchi and A. Vishwanath, Kitaev-Heisenberg models for iridates on the triangular, hyperkagome, kagome, fcc, and pyrochlore lattices, *Phys. Rev. B* **89**, 014414 (2014).

[129] M. Fishman, S. R. White, and E. M. Stoudenmire, The itensor software library for tensor network calculations, *SciPost Phys. Codebases*, 4 (2022).

[130] S. R. White and A. L. Chernyshev, Neél Order in Square and Triangular Lattice Heisenberg Models, *Phys. Rev. Lett.* **99**, 127004 (2007).

[131] Z. Zhu, D. A. Huse, and S. R. White, Weak Plaquette Valence Bond Order in the $S = 1/2$ Honeycomb J_1 - J_2 Heisenberg Model, *Phys. Rev. Lett.* **110**, 127205 (2013).

[132] Z. Zhu and S. R. White, Spin liquid phase of the $S = \frac{1}{2}$ J_1 - J_2 Heisenberg model on the triangular lattice, *Phys. Rev. B* **92**, 041105(R) (2015).

[133] Z. Zhu, D. A. Huse, and S. R. White, Unexpected z -Direction Ising Antiferromagnetic Order in a Frustrated Spin-1/2 J_1 - J_2 XY Model on the Honeycomb Lattice, *Phys. Rev. Lett.* **111**, 257201 (2013).

[134] Z. Zhu, P. A. Maksimov, S. R. White, and A. L. Chernyshev, Disorder-Induced Mimicry of a Spin Liquid in YbMgGaO₄, *Phys. Rev. Lett.* **119**, 157201 (2017).

[135] Z. Zhu, P. A. Maksimov, S. R. White, and A. L. Chernyshev, Topography of Spin Liquids on a Triangular Lattice, *Phys. Rev. Lett.* **120**, 207203 (2018).

[136] S. Jiang, J. Romhányi, S. R. White, M. E. Zhitomirsky, and A. L. Chernyshev, Where is the Quantum Spin Nematic?, *Phys. Rev. Lett.* **130**, 116701 (2023).

[137] S. Jiang, D. J. Scalapino, and S. R. White, Ground-state phase diagram of the t - t' - J model, *Proc. Natl. Acad. Sci. U.S.A.* **118** (2021).

[138] A. Biffin, R. D. Johnson, I. Kimchi, R. Morris, A. Bombardi, J. G. Analytis, A. Vishwanath, and R. Coldea, Noncoplanar and Counterrotating Incommensurate Magnetic Order Stabilized by Kitaev Interactions in γ -Li₂IrO₃, *Phys. Rev. Lett.* **113**, 197201 (2014).

[139] A. Biffin, R. D. Johnson, S. Choi, F. Freund, S. Manni, A. Bombardi, P. Manuel, P. Gegenwart, and R. Coldea, Unconventional magnetic order on the hyperhoneycomb Kitaev lattice in β -Li₂IrO₃: Full solution via magnetic resonant x-ray diffraction, *Phys. Rev. B* **90**, 205116 (2014).

[140] I. Kimchi, R. Coldea, and A. Vishwanath, Unified theory of spiral magnetism in the harmonic-honeycomb iridates α , β , and γ -Li₂IrO₃, *Phys. Rev. B* **91**, 245134 (2015).

[141] S. C. Williams, R. D. Johnson, F. Freund, S. Choi, A. Jesche, I. Kimchi, S. Manni, A. Bombardi, P. Manuel, P. Gegenwart, and R. Coldea, Incommensurate counterrotating magnetic order stabilized by Kitaev interactions in the layered honeycomb α -Li₂IrO₃, *Phys. Rev. B* **93**, 195158 (2016).

[142] I. Kimchi and R. Coldea, Spin dynamics of counterrotating Kitaev spirals via duality, *Phys. Rev. B* **94**, 201110 (2016).

[143] C. Lanczos, An iteration method for the solution of the eigenvalue problem of linear differential and integral operators, *J. Res. Natl. Bur. Stand. B* **45**, 255 (1950).

[144] E. Dagotto, Correlated electrons in high-temperature superconductors, *Rev. Mod. Phys.* **66**, 763 (1994).

[145] Q. Wang, A. de la Torre, J. A. Rodriguez-Rivera, A. A. Podlesnyak, W. Tian, A. A. Aczel, M. Matsuda, P. J. Ryan, J.-W. Kim, J. G. Rau, and K. W. Plumb, Pulling order back from the brink of disorder: Observation of a nodal line spin liquid and fluctuation stabilized order in K₂IrCl₆ (2024), arXiv:2407.17559 [cond-mat.str-el].

[146] M. J. Freiser, Thermal Variation of the Pitch of Helical Spin Configurations, *Phys. Rev.* **123**, 2003 (1961).

[147] K. Yosida, The Status of the Theories of Magnetic Anisotropy, *J. Appl. Phys.* **39**, 511 (1968).

[148] Y.-D. Li, X. Wang, and G. Chen, Anisotropic spin model of strong spin-orbit-coupled triangular antiferromagnets, *Phys. Rev. B* **94**, 035107 (2016).

[149] T. A. Kaplan and N. Menyuk, Spin ordering in three-dimensional crystals with strong competing exchange interactions, *Philos. Mag.* **87**, 3711 (2007).

[150] E. Sela, H.-C. Jiang, M. H. Gerlach, and S. Trebst, Order-by-disorder and spin-orbital liquids in a distorted Heisenberg-Kitaev model, *Phys. Rev. B* **90**, 035113 (2014).

[151] M. L. Abell, J. P. Braselton, J. A. Rafter, and J. A. Rafter, *Statistics with Mathematica*, Vol. 1 (Academic Press, 1999).

[152] M. Mourigal, W. T. Fuhrman, A. L. Chernyshev, and M. E. Zhitomirsky, Dynamical structure factor of the triangular-lattice antiferromagnet, *Phys. Rev. B* **88**, 094407 (2013).